# *PRINCIPAL MODES AND THEIR APPLICATION FOR FIBER BASED MODE DIVISION MULTIPLEXING TRANSMISSION SCHEMES*

Vorgelegt von
Dipl. Ing. Adrián A. Juárez M.
geboren in Guatemala

Von der Fakultät IV - Elektrotechnik und Informatik
der Technischen Universität Berlin
zur Erlangung des akademischen Grades

Doktor der Ingenieurwissenschaften
-Dr. Ing.-

genehmigte Dissertation

Promotionsausschuss:

| | |
|---|---|
| Vorsitzender: | Herr Prof. Caire, Ph. D. |
| Gutachter: | Herr Prof. Dr. –Ing. Klaus Petermann |
| Gutachter: | Herr Prof. Dr. –Ing. Peter Krummrich |
| Gutachter: | Herr. Dr. –Ing. Henning Bülow |

Tag der Wissenschaftlichen Aussprache: 23.02.2015

Berlin 2015

# Abstract

The yearly internet traffic growth of 45% requires new optical transmission technologies to meet the increasing capacity demand. The use of multimode fibers in mode division multiplexing operation could be a possible candidate to increase the transmission capacity for long haul transmission, as well as for short range transmission links such as communication within data centers, where multimode fibers are already in use. Here the operation of the multimode fiber is currently restricted to a single input, single output scheme. One of the issues of using multimode fibers is mode coupling and mode dispersion. This issue can be managed by using principal modes as transmission carriers modes as will be discussed in this thesis. To numerically verify this, a coherent multimode fiber model was developed. Here only linear affects like mode dispersion and mode coupling were taken into account. Principal mode transmission in mode division multiplexing scheme is analyzed and its limits examined. The maximal multiplexed transmission rate is imposed by the multimode fiber bandwidth, as long as principal mode dependent losses are compensated. In this case multiple input multiple output digital signal processing at the receiver is not required. Using digital signal processing at the receiver, combined with principal mode transmission has some advantages compared to the conventional LP-mode launch, if the memory of the system is limited to one symbol. In this case the equalizer is capable of equalizing twice the transmission rate that would be possible using the conventional LP-mode transmission.

# Zusammenfassung

Der Bedarf an immer schnelleren Datenübertragung ist in den letzten Jahren drastisch gewachsen. Dies erfordert die Entwicklung neuer Optischer Übertragungstechniken um diesem Bedarf entgegenzukommen. Eine Möglichkeit besteht darin, die Eigenwellen einer mehrwelligen Faser zu nutzen, um parallel Datenströme zu übertragen. Auf Grund von Modenkopplung und Modendispersion ist dies durch aufwendige Signalverarbeitung am Empfänger beschränkt, so dass nach anderen Lösungen gesucht werden muss. Eine Möglichkeit besteht darin, so genannte „Principal modes“ als Trägermoden zu verwenden. Diese Möglichkeit würde in dieser Dissertation numerisch untersucht und deren Grenzen bestimmt. Um dies zu untersuchen, wurde ein kohärentes Mehrwelliges Fasermodell entwickelt, um die Übertragung von Signalen mit höherwertigen modulationsformaten in einer mehrwelligen Faser darzustellen. Darauf basierend wurde die „Principal mode“ Übertragung in mehrwelligen Fasern im „mode division multiplexing“ Betrieb untersucht. Aus der Analyse geht hervor, dass diese Art von Übertragung durch die Bandbreite der mehrwelligen Faser begrenzt ist, solange die „Principal Mode“ abhängigen Verluste kompensiert werden. Die Anwendung digitaler Signalverarbeitung ermöglicht es, die Symbolrate weiterhin zu erhöhen, wobei dann der Unterschied zum herkömmlichen Ansatz, die LP-moden als Trägerwellen zu verwenden, nur dann von Bedeutung ist, wenn die Gedächtnislänge nur einen Symbollänge beträgt.

# Index of content

# 1. Introduction

Glass fiber is becoming more and more important these days, specially due to the high bandwidth demand induced by many new internet applications such as high definition video communication, cloud computing and social networking amongst others. All these new applications have led to a yearly internet traffic growth of 45 % [1], which requires new optical technologies to meet the growing bandwidth demand. Fiber based communications is mainly divided into two categories: technologies based on single mode fibers (SMF), which are commonly used for long and mid – range transmission and technologies based on multimode fibers (MMF), which are mainly used in short range transmissions due to their larger numerical aperture (NA) and core radius $\rho_0$, which directly translates into lower assembly costs due to larger coupling tolerances [2].

Short-range transmission, commonly limited to a transmission range of less than one kilometer, is typically needed in data centers, which contain thousands of servers that form parallel supercomputing infrastructure [3]. The communication traffic in data centers is currently limited between servers that are located within one building, but it is foreseen to extent to several buildings to form cluster fabrics for warehouse scale computing [4] in order to keep up with increasing traffic demand. This places some new challenges for data center operators, since operating at larger transmission rates reduces the maximal transmission distance. To understand this limitation, it is necessary to understand the standard MMF operation. Fig. 1 shows a simplified MMF transmission scenario. Here a pulse is modulated on the optical carrier, which

can be emitted for instance from a light emitting diode (LED), by modulating the driving current. Light is then coupled into the MMF, where the optical pulse is distorted during propagation if no modal coupling is present, by modal dispersion[1]. At the output of the MMF, the optical power is converted by means of a photodiode (PD) into electrical current, where the pulse appears distorted as depicted in Fig. 1. This distortion causes inter symbol interference, in the case of data transmission, where a very long bit stream is transmitted through the MMF, which would then result in bit errors at the receiver. The effect of modal dispersion is the main limiting factor in MMF transmission [5,6] and can be understood in a very simplified manner as shown in Fig. 1. Here two different modes propagate with different group velocity in the MMF, arriving at the receiver at different time instances. If the light source was modulated, the maximal achievable transmission distance would roughly be given by the maximal allowable time delay between the slowest and fastest modes, so that the pulses are not distorted.

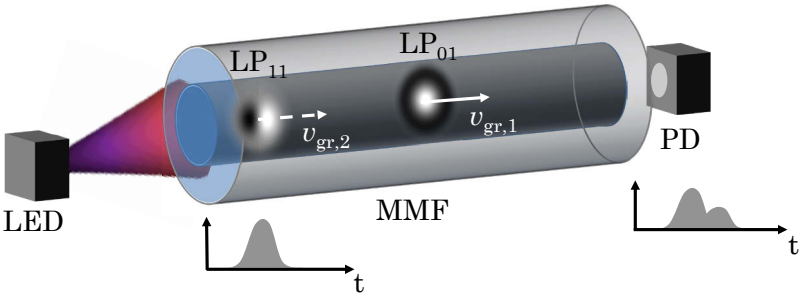


Fig. 1. Traditional MMF operation. A pulse is modulated on the optical carrier (here a LED) which is then coupled into the MMF. The pulse appears distorted on the output side of the MMF after being detected by the photodiode (PD) due to mode dispersion. Modal dispersion is induced by mode propagating at different group velocities, here shown exemplary for the $LP_{01}$ and $LP_{11}$ mode, with group velocities $v_{gr,1}$ and $v_{gr,2}$ respectively.

A key factor that describes the maximal transmission rate over a given length is known as the bandwidth length product and much effort has been applied over the last decades to improve this factor. Several MMF standards are commercially available, capable of achieving higher transmission rate over a given distance (some examples include the OM1 – OM4 MMF specified by the

[1] Here only linear effects are being considered.

IEEE standards). All these MMF are specified at a wavelength of $\lambda = 850\,\text{nm}$ since transmitters and receivers are available at low cost. To increase the transmission capacity further, it is essential to explore new transmission schemes which will be reviewed in the next subsection.

## 1.1 State of the art

To increase the transmission rate even more, new approaches have been proposed. These are not necessarily low cost, but are capable of increasing the transmission capacity further. These include

**Electronic dispersion compensation:** This technique distorts the input or output signal, using for example a feed-forward equalizer, in such a way as to compensate for the distortion effects of the MMF and/or vertical cavity surface emitting lasers (VCSEL). Several reports have shown [7,8] the feasibility of this approach, improving the maximal transmission rate at the given transmission distance.

**Frequency/Wavelength division multiplexing.** These approaches rely on using multiple sub – carriers to increase the overall transmission rate and to mitigate inter symbol interference. These subcarriers can either be optical, as in coarse wavelength division multiplexing (CWDM), where several optical emitters are multiplexed within the 150 nm transmission window in the 850 nm region; or electric subcarriers, as in subcarrier multiplexing, where regions beyond the baseband showing flat frequency response are used for transmission. These electrical and optical multiplexing techniques can be combined to obtain extremely high data rates [2].

**Space division multiplexing.** One straight forward approach to increase the transmission rates of MMF for data center application was introduced in the IEEE 802.3ba standard, by defining the 40GBASE – SR4 and 100GBASE – SR10 technologies [2]. This approach relies on the use of space division multiplexing (SDM), which bundles four or ten OM3 type MMF, to achieve transmission rates up to 100 Gbit/s for a maximal distance of 100 meters. This approach has a major drawbacks which is scalability, since the amount of MMF required would become most likely unmanageable [9].

The concept of SDM is not limited to simple MMF parallelization and several different approaches have been proposed to increase the transmission capacity of a MMF. One approach is the so called mode group division multiplexing

(MGDM) [10,11,12]. This approach relies on exciting and detecting a group of modes that have the same propagation constant and to encode information on each of these mode groups. This allows data transmission parallelization using one single MMF. Considering as an example an OM4 MMF, which guides ten mode groups at a wavelength of $\lambda_0 = 1.55$ µm. A multiplexing gain factor of ten can thus be achieved. Due to slightly different propagation constants within one mode group, the maximal transmission distance is limited by the maximal differential time delay between guided modes within one mode group. The multiplexing and de-multiplexing can be realized by using an offset launch [13] and offset mode filtering as shown for instance in [14] or by using spatial diversity detection using ring photo – diodes [15,16]. This approach does not require multiple input multiple output (MIMO) digital signal processing if coupling between mode groups is low and maximal transmission reach is limited to 1 – 2 km. In the case where mode coupling originated from micro-bending for example can no longer be neglected (for example if the transmission length exceeds 2 km), signal degradation increases dramatically, reducing the transmission performance of such multiplexing transmission systems. Since direct detection is normally applied to make this approach a simple, low cost approach, MIMO signal processing does not improve the performance significantly [17] since the phase information is not available at the receiver.

Spatial beam forming has also been proposed as a candidate for spatial division multiplexing in a MMF for short reach application using direct detection [18,19]. Here the channel needs to be known a priori to equalize the input mode field pattern as to maximize the output photodiode current of the $i^{th}$ photodiode of the $i^{th}$ optical output. This approach requires the use of one coherent laser source, which is then split into multiple outputs. Each output is then modulated with different data streams. Since all outputs are originated from one source, they all have a well-defined phase relation to each other which can be changed to a desired value by a phase shifter for example. A related approach was introduced by Fan and Khan in 2005 by the so called principal modes (PMs) [20]. They are computed and launched using the channel state information and therefore take into consideration the dispersive effects of the MMF and the mode coupling characteristics of the MMF. It was found that

these modes are frequency independent to the first order and therefore robust against modal dispersion. An intuitive example of their benefit is shown in Fig. 2.

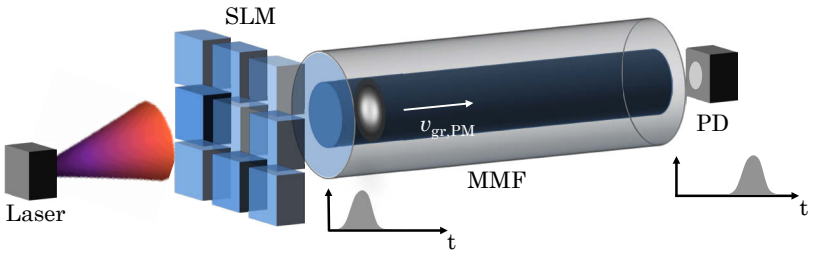


Fig. 2. The main concept of principal mode transmission in MMF. Here the spatial field distribution is modified by the spatial light modulator (SLM) to a match a principal mode. The field distribution representing the principal mode inside the MMF is a weighted superposition of the guided eigenmodes of the unperturbed MMF. The principal mode travels inside the MMF with a well-defined group velocity $v_{gr,\,PM}$. For this reason no signal distortion is observed at the output of the MMF.

Here the field distribution of a laser light source is mapped into a principal mode which in turn excites the MMF. The mapping is shown here exemplary using a spatial light modulator (SLM), but can be done also by silicon photonics grating couplers [21] or special lenses [22]. The pulse modulated on the laser propagates though the MMF and appears undistorted at the output of the MMF, in contrast to resulting output pulse shown in Fig. 1. This approach was firstly demonstrated by [23,24] using a standard graded index MMF. By using adaptive optics, in form of a spatial light modulator, it was possible to excite a PM, achieving transmission rates of 100 Gbit/s over a transmission distance of 2.2 km [25]. This shows the potential of the approach, since the MMF used was an OMF 4 type fiber, optimized for the wavelength of $\lambda_0 = 850\,\mathrm{nm}$ and hence, with a MMF bandwidth length product of less than $2\,\mathrm{GHz}\times\mathrm{km}$ at the wavelength of $\lambda_0 = 1.55$ µm. Using the same MMF in the conventional transmission scheme would allow a maximal transmission rate of roughly less than 2 Gbit/s for one kilometer. This concept will be extended in this work by using the PMs as carriers for mode division multiplexing (MDM) as discussed in the section 4.

## 1.2 Goal and outline of this thesis

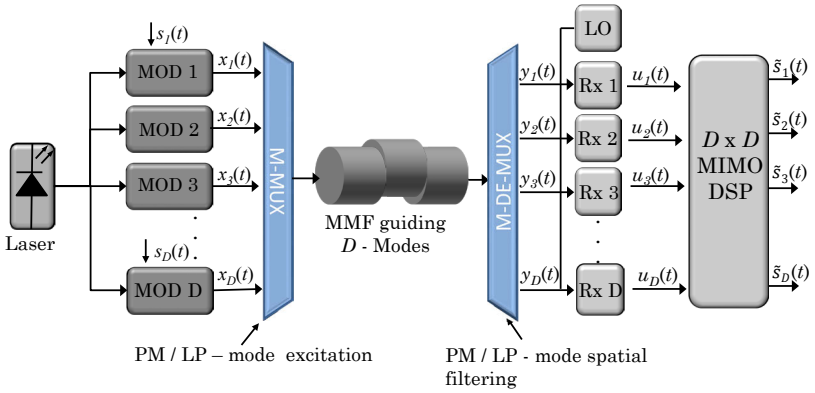


Fig. 3. The concept of mode division multiplexing in a multimode fiber.

The natural extension of the principal mode approach is its use in a MDM scheme, as mentioned earlier. This approach makes sense if one takes into consideration that multiple data streams transmitted through the MMF in parallel are likely to couple amongst each other, limiting the transmission performance of such a system. This performance limitation can be compensated using digital signal processing at the receiver, but mode dispersion (MD) will enhance the complexity of such a receiver since it complexity increases roughly proportional to the square of maximal differential time delay between the guided modes. A principal mode transmission in MDM scheme would be transparent towards these effects as explained in section 4 and might perform well without the use of MIMO digital signal processing at the receiver or even reduce its complexity if present. A possible transmission scenario is depicted in Fig. 3. Here each PM, containing a different data stream, is multiplexed (MUX) into the MMF, transmitted and then de-multiplexed (DEMUX) by a spatial filter and detected at the receiver. At the receiver, it is possible to use MIMO digital signal processing to recover the input information. This MDM approach can be combined with wavelength division multiplexing (WDM) approaches, but will be studied here at only one wavelength, namely $\lambda_0 = 1.55$ µm. This wavelength, which is commonly used for long range transmission, is used here since it is believed that silicon photonics will play an important role in future transceiver and receivers structures for MMF transmission systems as the joint work of Corning and Intel suggest [26]. Since silicon is not transparent for wavelengths below $\lambda \leq 1\mu m$, the usage of larger

wavelengths are necessary and since most of the research is being realized at $\lambda_0 = 1.55\mu m$, it suggest this to be the wavelength of choice. In addition, silica fibers exhibit their absorption minimum at $\lambda_0 = 1.55\,\mu m$, achieving at this wavelength low loss transmission.

To understand the main limitations of the MMF in MDM scheme using PMs as carriers, a model needs to be established. As higher order modulation formats are likely to be used in future MMF transmission links and PMs require the complete amplitude and phase information of the transmission channel, a coherent MMF transmission model is necessary. To implement this, complete knowledge of the eigenmodes of the unperturbed MMF are essential, which will be dealt with in chapter 2. Here the Laguerre-Gaussian modes will be introduced, which are the eigenmodes of the infinitely extended parabolic index profile fiber and used in this work unless stated otherwise. These eigenmodes will be compared against the modes of the truncated parabolic index profile MMF in terms of field distribution, propagation constant and differential group delay. Chapter 3 will deal with the modeling of the MMF which includes mode coupling induced by splices and micro-bends. Here a simple model will be presented which is capable of evaluating the propagation inside the MMF with low computational effort. Chapter 4 will then use this transmission model to emulate a MDM transmission scenario using the PMs as carrier modes. This scenario will be compared towards the more common LP-mode launch in terms of transmission performance. To extend the applicability of this approach, the performance of the PM transmission will be analyzed using a multiple input multiple output (MIMO) digital signal processing receiver, which will be introduced in chapter 5. The performance of PM transmission in a MDM scheme will be compared towards the LP-mode transmission scheme. The conclusion of this thesis will then be presented in chapter 6.

# 2. Multimode fiber modes

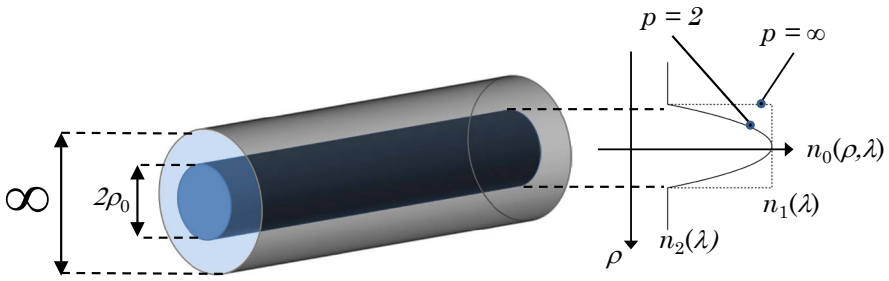


Fig. 4. Schematic of MMF. Refractive index is shown here exemplary for $p=2$ and $p=\infty$. The cladding is shown here to extend to infinity and the core diameter is denoted here by $2\rho_0$.

Fibers can be categorized mainly into two types of fibers: single mode fibers (SMF) and multimode fibers (MMF), while the latter is of interest here. The main structure is shown in Fig. 4 and can be divided into two areas: the core (dark blue) and cladding (light blue). The core area has a refractive index, which may have a radial dependence, denoted here as $n_0(\rho,\lambda)$. Its maximal value $n_1(\lambda)$ is found typically at the fiber core axis $(\rho=0)$. Light is guided in the core area by means of total internal reflection. For this reason, the material surrounding the core area, exhibits a smaller refractive index value $n_2(\lambda)$, which is called cladding. A common examined refractive index profile is the family of so called power law profiles, which is given by [27,5]:

$$n_0^2(\rho,\lambda)=n_1^2(\lambda)\left(1-2\Delta(\lambda)\left(\frac{\rho}{\rho_0}\right)^p\right) \tag{2.1}$$

Here $\rho_0$ denotes the core radius and $\Delta(\lambda)$ the normalized refractive index difference, which is defined as [27]:

$$\Delta(\lambda)=\frac{1}{2}\left(1-\frac{n_2^2(\lambda)}{n_1^2(\lambda)}\right)\approx\frac{n_1(\lambda)-n_2(\lambda)}{n_1(\lambda)} \tag{2.2}$$

The approximation given in Eq.(2.2) holds if $\Delta(\lambda)\ll 1$. The description given in Eq. (2.1) yields the step index MMF if $p=\infty$, as shown in Fig. 4 (dotted line) and the graded index profile (Fig. 4 shows exemplary the parabolic index profile with $p=2$). MMFs with refractive index profiles with $p$ around $p\approx 2$ are known to minimize the differential group delay (DGD) [5] between the propagating modes[2]. Since the goal of this work is to apply a MMF to use for MDM, it is necessary to reduce the differential time delay between the propagating modes in order to minimize the memory of the digital signal processing at the receiver. For this reason the analysis here is limited to power law profiles with $p\approx 2$. The refractive index $n_1(\lambda)$ can be calculated using the Sellmeier – equation, which is given as [28]:

$$n_1^2(\lambda)=1+\frac{1}{\lambda_L\lambda_e\left(\frac{1}{\lambda_e^2}-\frac{1}{\lambda^2}\right)}-\frac{\lambda^2}{\lambda_L^2}. \tag{2.3}$$

The resonance wavelengths $\lambda_e$ and $\lambda_L$ depend on the silica concentration [28].

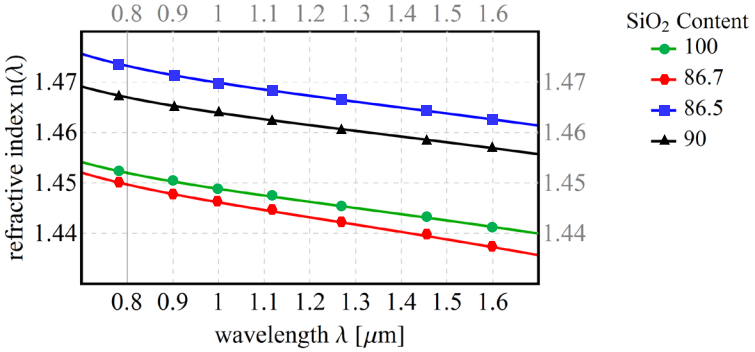


Fig. 5. Refractive index for different concentrations of $SiO_2$. This figure was plotted using the values in [28]. The green curve contains 100 % $SiO_2$ content, while the red curve contains 86.7% $SiO_2$ and 13.3% $B_2O_3$, the blue curve contains 86.5% $SiO_2$ and 13.5% $GeO_2$ and the black curve 90% $SiO_2$ and 10% $P_2O_5$

[2] This applies only if profile dispersion is neglected [34]. Different wavelengths require a different power law parameter $p$ to obtain an optimal MMF bandwidth. Here it will be assumed that this is the case.

Fig. 5 shows the refractive index for different concentrations of $SiO_2$. Here a 90 % silica concentration and 10 % $P_2O_5$ concentration is assumed (Black curve) for $n_1(\lambda)$. To understand the fundamentals of MMFs, it is necessary to analyze the MMF in terms of its eigenmodes. This is presented in the next subsection.

## 2.1 Vector wave equation

In order to describe the propagation of light inside a multimode fiber (MMF), it is necessary to assume that the region of interest is far away from any source of excitation, so that it is possible to describe the MMF with its bound modes. Their sum represents the complete electric and magnetic field vector $\vec{\mathbf{E}}(x,y,z)$ and $\vec{\mathbf{H}}(x,y,z)$ respectively [27]. These are given as:

$$\begin{aligned}\vec{\mathbf{E}}(x,y,z,t) &= \sum_r \tilde{a}_r \vec{\mathbf{E}}_r(x,y,z,t) + \sum_r \tilde{a}_{-r} \vec{\mathbf{E}}_{-r}(x,y,z,t) \\ \vec{\mathbf{H}}(x,y,z,t) &= \underbrace{\sum_r \tilde{a}_r \vec{\mathbf{H}}_r(x,y,z,t)}_{\text{Forward prop. wave}} + \underbrace{\sum_r \tilde{a}_{-r} \vec{\mathbf{H}}_{-r}(x,y,z,t)}_{\text{Backward prop. wave}}\end{aligned} \tag{2.4}$$

The index $r$ is an integer and extends over all guided modes, with total number $D$. The parameter $\tilde{a}_{\pm r}$ denotes the modal amplitudes. The summation extends over the forward and backward propagating waves as shown in Eq. (2.4). Only forward propagating waves will be considered here and therefore the second summation in Eq. (2.4) is set to zero. The electric and magnetic field satisfy Maxwell's equations, which can be expressed in differential form as[3]:

$$\begin{aligned}\nabla \times \vec{\mathbf{E}}_r &= -j\sqrt{\frac{\mu_0}{\epsilon_0}} k_0 \vec{\mathbf{H}}_r; \qquad \nabla \times \vec{\mathbf{H}}_r = j\sqrt{\frac{\mu_0}{\epsilon_0}} k_0 n_0^2(\rho,\lambda)\vec{\mathbf{E}}_r; \\ \nabla \cdot \left(n_0^2(\rho,\lambda)\vec{\mathbf{E}}_r\right) &= 0; \qquad\qquad \nabla \cdot \vec{\mathbf{H}}_r = 0.\end{aligned} \tag{2.5}$$

Here $k_0 = \omega\sqrt{\mu_0 \epsilon_0}$ is the wave number in free space, $\epsilon_0$ and $\mu_0$ the dielectric constant and magnetic permeability in free space, respectively. Equation (2.5) implies the use of the time dependence $\exp(j\omega t)$ [4]. For this reason, the derivative with respect to time $\partial/\partial t$ is replaced by $j\omega$, already applied in Eq.(2.5). Under the assumption that the refractive index does not change in propagation direction, which is assumed here to be the positive z-direction, the modal fields can be expressed in Cartesian coordinates, while omitting the time dependence $\exp(j\omega t)$ as:

$$\begin{aligned}\vec{\mathbf{E}}_r(x,y,z) &= \vec{\mathbf{e}}_r(x,y)\exp\left(-j\tilde{\beta}_r z\right), \\ \vec{\mathbf{H}}_r(x,y,z) &= \vec{\mathbf{h}}_r(x,y)\exp\left(-j\tilde{\beta}_r z\right)\end{aligned} \tag{2.6}$$

[3] Here the convention $\exp(j\omega t)$ is used; [27] uses the convention $\exp(-j\omega t)$.
[4] $j$ is the imaginary number defined as $j^2 = -1$.

or in cylindrical coordinates as:

$$\begin{aligned}\vec{\mathbf{E}}_r(r,\phi,z) &= \vec{\mathbf{e}}_r(r,\phi)\exp(-j\tilde{\beta}_r z),\\ \vec{\mathbf{H}}_r(r,\phi,z) &= \vec{\mathbf{h}}_r(r,\phi)\exp(-j\tilde{\beta}_r z).\end{aligned} \tag{2.7}$$

Here $\tilde{\beta}_r$ [5] is the propagation constant of the $r^{\text{th}}$ mode, $\vec{\mathbf{e}}_r(x,y)$ and $\vec{\mathbf{h}}_r(x,y)$ are electric and magnetic field vectors without any z-dependence. The propagation constant $\tilde{\beta}_r$ is frequency dependent in general, but the current analysis is limited to a single frequency so that this dependence is omitted for now. The vector wave equation for the electric field can be obtained by eliminating the magnetic field by performing the rotation of the first equation in Eq.(2.5). The following expression is obtained:

$$\vec{\nabla}\times\vec{\nabla}\times\vec{\mathbf{E}}_r = \vec{\nabla}\left(\vec{\nabla}\cdot\vec{\mathbf{E}}_r\right) - \vec{\nabla}^2\vec{\mathbf{E}}_r = j\omega\mu_0\vec{\nabla}\times\vec{\mathbf{H}}_r = k_0^2 n_0^2(\rho,\lambda)\vec{\mathbf{E}}_r. \tag{2.8}$$

This equation can be simplified using the fact that:

$$\begin{aligned}\vec{\nabla}\left(n_0^2(\rho,\lambda)\vec{\mathbf{E}}_r\right) &= \vec{\mathbf{E}}_r\vec{\nabla}n_0^2(\rho,\lambda) + n_0^2(\rho,\lambda)\vec{\nabla}\cdot\vec{\mathbf{E}}_r\\ \vec{\mathbf{E}}_r\vec{\nabla}n_0^2(\rho,\lambda) + n_0^2(\rho,\lambda)\vec{\nabla}\cdot\vec{\mathbf{E}}_r &= 0,\\ \vec{\nabla}\cdot\vec{\mathbf{E}}_r &= -\vec{\mathbf{E}}_r\left(\vec{\nabla}n_0^2(\rho,\lambda)\right)/n_0^2,\\ &= -\vec{\mathbf{E}}_r\vec{\nabla}\left\{\log\left(n_0^2(\rho,\lambda)\right)\right\}.\end{aligned} \tag{2.9}$$

Applying (2.9) to (2.8) yields:

$$\left\{\vec{\nabla}^2 + n_0^2(\rho,\lambda)k_0^2\right\}\vec{\mathbf{E}}_r = -\vec{\nabla}\left\{\vec{\mathbf{E}}_r\vec{\nabla}_t\ln\left(n_0^2(\rho,\lambda)\right)\right\}. \tag{2.10}$$

If a similar procedure is applied to the magnetic field $\vec{\mathbf{H}}_r$ the following equation is obtained [27]:

$$\left\{\vec{\nabla}^2 + n_0^2(\rho,\lambda)k_0^2\right\}\vec{\mathbf{H}}_r = \left(\vec{\nabla}\times\vec{\mathbf{H}}_r\right)\times\vec{\nabla}_t\ln\left(n_0^2(\rho,\lambda)\right). \tag{2.11}$$

Equations (2.10) and (2.11) have been stated here independently of any coordinate system. A great simplification is achieved, if the field vectors have components referred to fixed Cartesian directions [27]. In that case the vector operator $\vec{\nabla}^2$ can be replaced by the scalar Laplacian operator $\Delta$. Since the fields are independent to the choice of coordinate system, the fields are expressed as:

[5] Here the tilde is used to differentiate to $\beta$, which is the propagation constant using the weak guidance approximation.

$$\begin{aligned}\vec{\mathbf{E}}_r &= e_{r,x}(\rho,\phi)\vec{\mathbf{x}} + e_{r,y}(\rho,\phi)\vec{\mathbf{y}} + e_{r,z}(\rho,\phi)\vec{\mathbf{z}},\\ \vec{\mathbf{H}}_r &= h_{r,x}(\rho,\phi)\vec{\mathbf{x}} + h_{r,y}(\rho,\phi)\vec{\mathbf{y}} + h_{r,z}(\rho,\phi)\vec{\mathbf{z}}.\end{aligned} \tag{2.12}$$

Here $\vec{\mathbf{x}},\vec{\mathbf{y}}$ and $\vec{\mathbf{z}}$ are unit vectors in x-, y- and z-direction respectively. Equation (2.10) and (2.11) can now be formulated as:

$$\begin{aligned}\left\{\Delta + n_0^2(\rho,\lambda)k_0^2\right\}\vec{\mathbf{E}}_r &= -\nabla\left\{\vec{\mathbf{E}}_r\nabla_t \ln\left(n_0^2(\rho,\lambda)\right)\right\},\\ \left\{\Delta + n_0^2(\rho,\lambda)k_0^2\right\}\vec{\mathbf{H}}_r &= \left(\nabla\times\vec{\mathbf{H}}_r\right)\times\nabla_t \ln\left(n_0^2(\rho,\lambda)\right).\end{aligned} \tag{2.13}$$

The subscript $t$ denotes that the operator operates only on the transversal components. The right side of (2.13) still couples the field components to each other and it is therefore reasonable to introduce some simplification. This is mainly the weak guidance approximation, which is discussed in the next subsection.

## 2.2 Scalar wave equation

If it is possible to assume, that the normalized refractive index difference $\Delta(\lambda)$ between core and cladding is much smaller than unity, the vector wave equation can be reduced to a scalar eave equation [5] since the right hand side Eq. (2.13) becomes zero. This enables the use of so called linear polarized modes (LP-Modes) which was first proposed by [29] for step index fibers. As a consequence, the solution to the eigenvalue equation is virtually insensitive to the polarization properties of the MMF [27] and the waves propagating along the waveguide experience almost a homogeneous medium, which leads to almost a free space propagation character. For this reason polarization effects will not be accounted during this work and the number of modes stated here and further on refer always to the case of single polarization. The transversal magnetic field components is then given by [5]:

$$\vec{\mathbf{H}}_{r,t} = \left(\frac{\epsilon_0}{\mu_0}\right)^{1/2} n_1(\lambda)\,\vec{\mathbf{z}} \times \vec{\mathbf{E}}_{r,t}. \tag{2.14}$$

The z- component of the electric and magnetic field vector is given as:

$$\begin{aligned} E_{r,z} &= \frac{j\nabla_t \vec{\mathbf{E}}_{r,t}}{k_0 n_1(\lambda)\rho_0}, \\ H_{r,z} &= \frac{j\nabla_t \vec{\mathbf{H}}_{r,t}}{k_0 n_1(\lambda)\rho_0}, \end{aligned} \tag{2.15}$$

where $\nabla_t = \nabla - \partial/\partial_z$ is the Nabla operator operating only the on the transversal coordinate components. Both vector wave equations result in:

$$\begin{aligned} \left\{\Delta_t + n_0^2(\rho,\lambda)k_0^2 - \beta_r^2\right\}\vec{\mathbf{e}}_{r,t} &= 0, \\ \left\{\Delta_t + n_0^2(\rho,\lambda)k_0^2 - \beta_r^2\right\}\vec{\mathbf{h}}_{r,t} &= 0. \end{aligned} \tag{2.16}$$

Here the use of Eq. (2.7) and $\partial/\partial z = -j\beta$ has been applied. These fields satisfy the orthogonality condition, stated here for the electric field in one polarization directions as [28]:

$$\iint_A e_{r,t}(r,\phi)\, e^*_{r',t}(r,\phi)\, dA = 0, \tag{2.17}$$

where $A$ extends over the entire fiber cross-section and this condition holds if $r \neq r'$. If $r = r'$ this integral is proportional to the guided power [5], but will be normalized to unity as:

$$\iint_A e_{r,t}(r,\phi)\, e_{r,t}^{*}(r,\phi)\, dA = 1 \tag{2.18}$$

Since the MMF is circularly symmetric, it makes sense to use a cylindrical coordinate system to describe the eigenmodes of the MMF. Equation (2.16) can therefore by written as:

$$\left(\frac{1}{\rho}\frac{\partial}{\partial r}\left\{\rho\frac{\partial}{\partial \rho}\right\} + \frac{1}{\rho^2}\frac{\partial^2}{\partial \phi^2} + n_0^2(\rho,\lambda)k_0^2 - \beta_r^2\right)\begin{Bmatrix}\vec{\mathbf{e}}_{r,t}(\rho,\phi)\\ \vec{\mathbf{h}}_{r,t}(\rho,\phi)\end{Bmatrix} = 0. \tag{2.19}$$

The following equations are limited to the transverse electric field vector $\vec{\mathbf{e}}_{r,t}(r,\phi)$ only, since the equation for the transverse magnetic field vector $\vec{\mathbf{h}}_{r,t}(r,\phi)$ is the same. If the separable form:

$$\vec{\mathbf{e}}_{r,x}(\rho,\phi) = \vec{\mathbf{x}}\,\psi_l(\rho)\begin{Bmatrix}\sin(l\phi)\\ \cos(l\phi)\end{Bmatrix}, \tag{2.20}$$

is applied to Eq. (2.19), where $\psi_l(\rho)$ is a function that has only a radial dependency and $l$ is an integer denoting the circumferential order, it is possible to reformulate (2.19) for one polarization direction as:

$$\left(\frac{1}{\rho}\frac{\partial}{\partial \rho}\left\{\rho\frac{\partial}{\partial \rho}\right\} + n_0^2(\rho,\lambda)k_0^2 - \beta_r^2 - \frac{l^2}{\rho^2}\right)\psi_l(\rho) = 0. \tag{2.21}$$

This equation can be normalized by introducing the following dimensionless variable $R = \rho/\rho_0$ which is also used in the argument of $\psi_i(\rho)$ further on. In In order to solve Eq.(2.21), it is necessary to specify the refractive index profile. As explained earlier, it is necessary to minimize the DGD spread between propagating modes in order to minimize the complexity of digital signal processing at the receiver if the MMF is to be used for MDM operation. For this reason, the power law refractive index profile given in (2.1) with $p = 2$ is used to analyze the MMF further. Small deviations from this profile are discussed later in section 2.6. This leads to the following differential equation [27]:

$$\left\{\frac{\partial^2}{\partial R^2} + \frac{1}{R}\frac{\partial}{\partial R} - \frac{l^2}{R^2} + u_r^2 - V^2R^2\right\}\psi_l(R) = 0, \tag{2.22}$$

where Eq. (2.1) has been used. The parameters $u_r$ and $V$ are given as:

$$u_r = \rho_0 \sqrt{k_0^2 n_1^2(\lambda) - \beta_r^2},$$
$$V = k_0 n_1(\lambda) \rho_0 \sqrt{2\Delta(\lambda)}. \tag{2.23}$$

A good approximation to the problem stated in Eq.(2.22) can be found if it is assumed that the parabolic profile extends to infinity as shown in Fig. 6 with the black dashed curve. The solution to the modal field distribution can be found in terms of the Laguerre-Gauss modes, which are discussed in the next subsection.

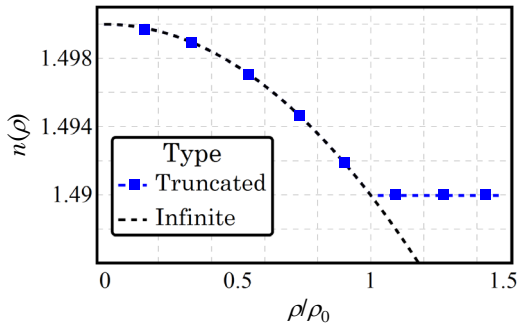


Fig. 6 Exemplary refractive index profile. Blue curve shows the truncated profile, which has a constant value for $\rho/\rho_0 > 1$, black curve shows the infinite parabolic profile

## 2.3 Solution to the infinite square law profile

The following trial solution

$$\psi_l(R) = g_l(VR^2)R^l \exp(-VR^2/2) \tag{2.24}$$

is applied as discussed in [27] to Eq. (2.22) in order to transform the differential equation to (see Annex A.1):

$$\left\{ w\frac{d}{dw^2} + (l+1-w)\frac{d}{dw} + \frac{u_r^2}{4V} + \frac{l+1}{2} \right\} g_l(w) = 0. \tag{2.25}$$

The parameter $w$ is given as $w = VR^2$. The solution which ensures that $\psi_l(R)$ is bounded is the generalized Laguerre polynomial $L_q^l(VR^2)$ [27,30][6]. The constant $q$ is bounded to be an integer and given by:

$$q = \frac{u_r^2}{4V} - \frac{l-1}{2}. \tag{2.26}$$

Together with Eq. (2.23) it is possible to determine the propagation constant $\beta_{l,q+1}$[7] as [31]:

$$\beta_{l,q+1} = n_1(\lambda)k_0\sqrt{1 - \frac{2\sqrt{2\Delta(\lambda)}(2q+l+1)}{\rho_0 k_0 n_1(\lambda)}}. \tag{2.27}$$

The field distribution in $x$ or $y$ polarization is therefore given as [27]:

$$e_{l,q+1}(\rho,\phi) = \tilde{C}_{l,q+1}R^l L_q^l(VR^2)\exp\left(-\frac{VR^2}{2}\right)\begin{cases}\cos(l\phi)\\ \sin(l\phi)\end{cases}. \tag{2.28}$$

where $\tilde{C}_{l,q+1}$ is a normalization constant which normalizes the field to unity to satify Eq. (2.18). Before proceeding to normalize $e_{l,q+1}(\rho,\phi)$, it is necessary to reformulate Eq.(2.28) and introduce some parameters. The parameter $\xi$ is introduced and is defined as:

$$\xi = \sqrt{\frac{\rho_0}{n_1(\lambda)k_0\sqrt{2\Delta(\lambda)}}}. \tag{2.29}$$

---

[6] The Laguerre polynomial can be described by using the Rodrigues' Formula given in [30] as: $L_q^l(x) = (e^x x^{-l}/q!)d^n(e^{-x}x^l x^q)/dx^n$.

[7] The modal subscript $r$ is now given with $l$ and $q$ describing circumferential and radial order respectively. Adding the value of one to $q$ is necessary to match the LP – mode notation, where the notation $LP_{l,q+1}$ notation is followed.

Using the fact that $VR^2 = \rho^2 / \xi^2$, the electric field of mode $(l,q)$ can be formulated as [32]:

$$e_{l,q+1}(\rho,\phi) = C_{l,q+1}\left(\frac{\rho}{\xi}\right)^l L_q^l\left(\frac{\rho^2}{\xi^2}\right)\exp\left(-\frac{\rho^2}{2\xi^2}\right)\begin{cases}\cos(l\phi)\\ \sin(l\phi)\end{cases}. \tag{2.30}$$

The normalization constant $C_{l,q}$ is given as [32]:

$$C_{l,q+1} = \frac{1}{\xi}\sqrt{\frac{b_l}{\pi}\frac{q!}{(l+q)!}}, \qquad b_l = \begin{cases}1 \text{ for } l = 0\\ 2 \text{ for } l \neq 0\end{cases}. \tag{2.31}$$

The solution given in Eq. (2.30) is known as the Laguerre-Gauss modes and Fig. 7 shows as an example the intensity distribution of the fundamental $LP_{01}$ mode, while (b) shows as an example the intensity distribution of the $LP_{22}$ mode.

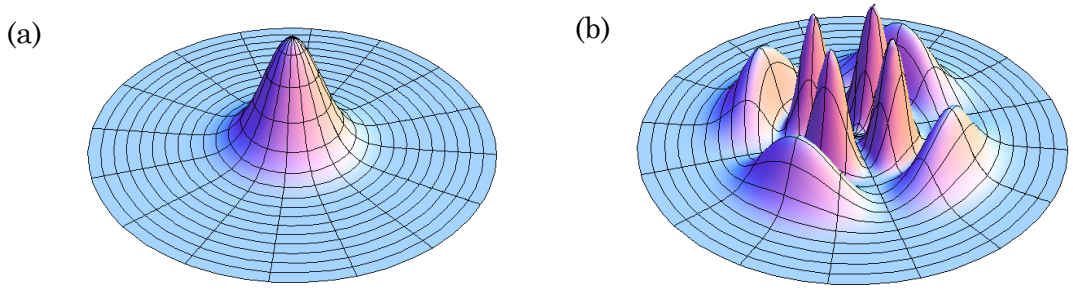


Fig. 7. Spatial intensity distribution of (a) $LP_{01}$ Mode, (b) $LP_{22}$ Mode

It is possible to give $\xi$ a physical interpretation if the fundamental mode is analyzed. The magnitude of the pointing vector in propagation direction is given as:

$$S_{l,q+1} = \frac{1}{2}\left[\vec{\mathbf{e}}_{l,q+1}(\rho,\phi)\times\vec{\mathbf{h}}^*_{l,q+1}(\rho,\phi)\right]\vec{\mathbf{z}} \propto \left|e_{l,q+1}(\rho,\phi)\right|^2, \tag{2.32}$$

For the fundamental mode $(l = 0 \text{ and } q = 0)$ the pointing vector is proportional to:

$$S_{0,0} \propto \exp\left(-\frac{\rho^2}{\xi^2}\right). \tag{2.33}$$

The pointing vector drops to 1/e of its maximal value at $\rho = \xi$ [8]. Since the optical power is proportional to $S$ it is possible to state $2\xi$ as the diameter, where the power has dropped to 1/e of its maximal value. The Laguerre-Gauss modes are going to be used throughout the entire work unless stated otherwise.

### 2.3.1 Estimation of propagation constants

The propagation constant $\beta_{l,q+1}$ , formulated in Eq.(2.27), describes the propagation of mode ($l$,$q$) in $z$-direction and is in general frequency dependent since it includes, among others, the frequency dependence of the refractive index, described in Eq.(2.3). It is useful to expand the propagation constant $\beta_{l,q+1}$ in terms of a Taylor series, which can be found in textbooks such as [33], around the optical angular carrier frequency $\omega_0$ as:

$$\beta_{l,q+1}(\omega) \approx \beta_{l,q+1}^{(0)}\Big|_{\omega=\omega_0} + \beta_{l,q+1}^{(1)}\Big|_{\omega=\omega_0}(\omega-\omega_0) + \frac{1}{2}\beta_{l,q+1}^{(2)}\Big|_{\omega=\omega_0}(\omega-\omega_0)^2 . \tag{2.34}$$

Here $\beta_{l,q+1}^{(i)}$ is the i$^{\text{th}}$ derivative of $\beta_{l,q+1}$ with respect to $\omega$ at the center angular frequency $\omega_0$. The first derivative of $\beta_{l,q+1}(\omega)$ is performed by using the approximation $\sqrt{1-x} \approx 1 - x/2 - x^2/8$ which yields [31]:

$$\begin{aligned}
\frac{\partial\beta_{l,q+1}(\omega)}{\partial\omega}\Big|_{\omega=\omega_0} &\approx \frac{\partial}{\partial\omega}\left(1-\frac{\sqrt{2\Delta(\omega_0)}M}{\rho_0 n_1(\omega_0)k_0}-\frac{1}{8}\left(\frac{2\sqrt{2\Delta(\omega_0)}M}{\rho_0 n_1(\omega_0)k_0}\right)^2\right)\Bigg|_{\omega=\omega_0} \\
&= \frac{N_1(\omega_0)}{c_0}\left(1+\Delta(\omega_0)\left(\frac{M}{n_1(\omega_0)k_0\rho_0}\right)^2\right) \\
&\quad -\frac{M}{\rho_0}\left(\frac{1}{\sqrt{\Delta(\omega_0)}}+\frac{2\Delta(\omega_0)}{\rho_0 n_1(\omega_0)k_0}\right)\frac{\partial\Delta(\omega)}{\partial\omega}\Big|_{\omega=\omega_0} \\
\frac{\partial\beta_{l,q+1}(\omega)}{\partial\omega}\Big|_{\omega=\omega_0} &= \beta_{l,q+1}^{(1)} \approx \frac{N_1(\omega_0)}{c_0}\left(1+2\Delta^2(\omega_0)\left(\frac{M}{V}\right)^2\right)-\frac{M}{\rho_0\sqrt{\Delta(\omega_0)}}\frac{\partial\Delta(\omega)}{\partial\omega}\Big|_{\omega=\omega_0} .
\end{aligned} \tag{2.35}$$

[8] This is not be mistaken with the field mode radius given in [31]. The parameter $\xi$ is related to the mode field radius $w$ as $\sqrt{2}\xi = w$ .

Here Eq. (2.23) was applied. The simplification was achieved by assuming $1 \gg 2\Delta^2(\lambda)/V$ which is always the case for weakly guiding fibers. The degenerate mode group (DMG) number $M$ is given as:

$$M = 2q + l + 1 \tag{2.36}$$

and $N_1(\lambda)$ is the group index defined as $N_1(\lambda) = n_1(\lambda) - \lambda \partial n_1(\lambda)/\partial\lambda$ . The parameter $\beta_{l,q+1}^{(1)}$ has the unit of time per unit length and will be denoted by $\tau_{l,q+1}$ further on. It is important to mention here, that modes with the same DMG number $M$, have the same group velocity and can be gathered into groups, the so called degenerate mode groups. $M$ specifies the number of modes contained within the DMG with DMG number $M$. To evaluate the maximal DMG number $M_{\max}$, it is necessary to know the maximal number of guided modes, which is denoted by $D$. These can be obtained by evaluating Eq. (2.27) using the following condition [27]:

$$k_0 n_2(\lambda) < \beta_{l,q+1} \leq k_0 n_1(\lambda). \tag{2.37}$$

As soon as all the guided modes are known, it is possible to calculate $M_{\max}$ by using Eq. (2.36). The derivative of $\Delta(\lambda)$ with respect to $\omega$ can be related to profile dispersion, which is defined as [5]:

$$P = \frac{n_1(\lambda)}{N_1(\lambda)} \frac{\lambda}{\Delta(\lambda)} \frac{\partial \Delta(\lambda)}{\partial \lambda} \tag{2.38}$$

and causes a frequency dependent deviation of the time delay $\tau_{l,q+1}$, which influences the bandwidth length product of the MMF as shown in [34]. This can be countered by optimizing the exponent coefficient $p$ in Eq. (2.1) as shown in [34] for the wavelength of interest[9]. For this reason, it will be assumed that the few mode fiber (FMF) under consideration has an optimal exponent $p$ to counter for this effect. As will be shown later in section 2.6, the field distribution of such power law profiles are very similar to the field distribution in a MMF with parabolic index profile so that the use of Laguerre-Gauss modes is justified.

[9] Assuming a MMF with $\rho_0 = 25\,\mu\text{m}$, $NA = 0.2$, $n_1 = 1.457$ a profile dispersion value of $P = 0.13$ is calculated. Using the formulas given in [34] to estimate the optimal $p_{opt}$ parameter, a value of $p_{opt} = 1.72$ is obtained.

The second derivative $\beta_{l,q+1}^{(2)}$ is given as:

$$\begin{aligned}\left.\frac{\partial^2\beta_{l,q+1}(\omega)}{\partial\omega^2}\right|_{\omega=\omega_0} &= \frac{1}{c}\left.\frac{\partial N_1(\omega)}{\partial\omega}\right|_{\omega=\omega_0}\left(1+\Delta(\omega_0)\left(\frac{M}{n_1k_0\rho_0}\right)^2\right)\\ &\quad -\frac{2N_1^2\rho_0}{c^2}\frac{\Delta(\omega_0)M^2}{\left(n_1(\omega_0)k_0\rho_0\right)^3}\\ &= \frac{\lambda^3}{2\pi c^2}\left.\frac{\partial^2 n_1(\lambda)}{\partial\lambda^2}\right|_{\lambda=\lambda_0}\left(1+\Delta(\lambda_0)\left(\frac{M}{n_1(\lambda_0)k_0\rho_0}\right)^2\right)\\ &\quad -\frac{2N_1^2(\lambda_0)\rho_0}{c^2}\frac{\Delta(\lambda_0)M^2}{\left(n_1(\lambda_0)k_0\rho_0\right)^3}\\ \left.\frac{\partial^2\beta_{l,q+1}(\omega)}{\partial\omega^2}\right|_{\omega=\omega_0} &\approx \frac{\lambda^2}{2\pi c}D_M,\end{aligned} \tag{2.39}$$

where $D_M = \lambda c^{-1}\partial^2 n_1(\lambda)/\partial\lambda^2$ is known as material dispersion. The last expression in (2.39) was obtained by assuming $n_1(\lambda)k_0\rho_0 \gg 1$ [10]. Using the expressions obtained in (2.35) and (2.39) it is possible to formulate (2.34) as:

$$\beta_{l,q+1}(\omega) \approx \beta_{l,q+1}^{(0)} + \tau_{l,q+1}(\omega-\omega_0) + \frac{\lambda^2}{2\pi c}D_M(\omega-\omega_0)^2. \tag{2.40}$$

If the optical wave is modulated, the optical envelope, modulated on mode ($l$,$q$), travels with the group velocity $\mathrm{v}_{gr}^{(l,q+1)}$ given as:

$$\mathrm{v}_{gr}^{(l,q+1)} = \left(\left.\frac{\partial\beta_{l,q+1}(\omega)}{\partial\omega}\right|_{\omega=\omega_0}\right)^{-1} = \frac{1}{\tau_{l,q+1}}, \tag{2.41}$$

From Eq. (2.41) it becomes clear, that signals carried on several modes with different DMG number $M$, will at some point suffer from distortion. This is called modal dispersion (MD) and is the main cause of distortion in MMF [6]. The Laguerre-Gauss modes, given in Eq.(2.30), together with their propagation constants, given in Eq.(2.40), will be used throughout this work.

To justify the use of the Laguerre-Gauss modes, which is the solution of the infinite extended parabolic profile and does not take into account the effect of

[10] The expression $\lambda^2 D_M/(2\pi c)$ is one order of magnitude larger than the rest of the expression.

the cladding, a numerical analysis will be carried out in which the spatial mode distribution, propagation constant and group delay is evaluated and compared. This analysis takes into account the effect of the cladding, which, as shown later, has a great impact on the maximal DGD. The next subsection will therefore deal with the description of the numerical procedure used to estimate the mode distribution as well as propagation constants which is based on the work of [35,34].

## 2.4 Numerical estimation algorithm

In order to formulate Eq. (2.21) free from all fiber parameters other than $V$, the normalized propagation constant $B_r^2$ [11] is introduced, which is defined as [35]:

$$B_r^2 = \frac{k_0^2 n_1^2(\lambda) - \beta_r^2}{k_0^2\left(n_1^2(\lambda) - n_2^2(\lambda)\right)}. \tag{2.42}$$

$B_r$ is the normalized propagation constant bounded between zero and one[12]. Using the definition of $V$ in Eq. (2.23) and $R = \rho/\rho_0$, Eq. (2.21) is formulated as [35]:

$$\left\{R\frac{\partial}{\partial R}\left(R\frac{\partial}{\partial R}\right) + V^2R^2\left(B_r^2 - N(R)\right) - l^2\right\}\psi_l(R) = 0. \tag{2.43}$$

$N(R)$ is the normalized profile shape which has a minimum value of zero and a value of one at the core – cladding boundary. The solution to this problem in the cladding region $\left(N(R) = 1 \text{ for } R > 1\right)$, where it is assumed that the cladding extends to infinity as shown in Fig. 4, is given by the modified Bessel function $K_l$ of the second type as:

$$\psi_l(R) = AK_l\left(V\sqrt{1 - B_r^2}R\right). \tag{2.44}$$

The constant $A$ is determined by the boundary condition between core and cladding which dictates that $\psi_l(R)$ and $\partial\psi_l(R)/\partial R$ have to be continuous [35]. In addition, there are six boundary conditions at center of the axis $R = 0$. These are given as [35]:

$$\begin{aligned}
&\psi_l(0) = 1, \quad && \frac{\partial\psi_l(0)}{\partial R} = 0, \quad && l = 0\\
&\psi_l(0) = 0, \quad && \frac{\partial\psi_l(0)}{\partial R} = 1, \quad && l = 1\\
&\psi_l(0) = 0, \quad && \frac{\partial\psi_l(0)}{\partial R} = 0, \quad && l \geq 2
\end{aligned} \tag{2.45}$$

To reduce the number of boundary conditions the following transformation rule is applied to Eq.(2.43) as suggested by [35]:

---

[11] The index $r$ is used here to clarify that the normalized propagation constant varies with mode.

[12] $B_r$ is defined here as given in [35]. A more common definition is given for example in [5], which is related to the values given here by its square root value.

$$\psi_l(R) = R^l f_l(R). \tag{2.46}$$

Equation (2.43) is then transformed to:

$$R\frac{\partial^2 f(R)}{\partial R^2} + (2l+1)\frac{\partial f(R)}{\partial R} + RV^2\left[B_r^2 - N(R)\right] f_l(R) = 0, \tag{2.47}$$

with the following boundary conditions :

$$f_l(R)\big|_{R=0} = 1, \quad \left.\frac{\partial f_l(R)}{\partial R}\right|_{R=0} = 0, \quad \left.\frac{\partial^2 f_l(R)}{\partial R^2}\right|_{R=0} = \frac{V^2\left[N(0) - B_r^2\right]}{2(l+1)}. \tag{2.48}$$

The boundary condition for the second derivative has been deduced by applying the boundary conditions for the zero and first derivative to Eq. (2.47) and by using the rule of L'Hôpital [33]. The continuity condition at the core-cladding boundary delivers the boundary condition, which can be formulated as:

$$\frac{1}{f_l(R)\big|_R}\left.\frac{\partial f_l(R)}{\partial R}\right|_{R=0} + l + V\sqrt{1-B_r^2}\,\frac{K_{l-1}\left(V\sqrt{1-B_r^2}\right) + K_{l+1}\left(V\sqrt{1-B_r^2}\right)}{2K_l\left(V\sqrt{1-B_r^2}\right)} = 0. \tag{2.49}$$

Eq. (2.47) is now integrated for a fixed value $l$ and a random value of $B_r$ in the range of $0 < B_r < 1$. If $B_r$ satisfies Eq.(2.49), the correct radial field distribution $f_l(R)$ is found, together with its propagation constant now denoted as $\bar{B}_{l,q+1}$ [13]. Given $f_l(R)$, the electric field of the mode ($l$,$q$+1) can be described as:

$$\bar{e}_{l,q+1}(\rho,\phi) = \bar{C}_{l,q+1}\bar{\psi}_{l,q+1}(R)\begin{cases}\cos(l\phi)\\ \sin(l\phi)\end{cases} \tag{2.50}$$

with $\bar{\psi}_{l,\mathrm{q}+1}(R)$ given as:

$$\begin{aligned}\bar{\psi}_{l,q+1}(R) &= R^l f_{l,q+1}(R) && \text{for } R<1,\\ \bar{\psi}_{l,q+1}(R) &= AK_l\left(V\sqrt{1-\bar{B}_{l,q+1}^2}R\right) && \text{for } R>1.\end{aligned} \tag{2.51}$$

Here the line above $\bar{e}_{l,q+1}(\rho,\phi)$ is used to distinguish the electric field of the Laguerre-Gauss mode given in Eq. (2.30) and the numerical estimation in

[13] $B_r$ is now $\bar{B}_{l,q+1}$ since the field has a circumferential order $l$ and radial order $q$. The roots of Eq.(2.49) are used to define the radial order. In addition the propagation constant $\bar{B}_{l,q+1}$ and the normalized field distribution $\bar{e}_{l,q+1}$ have been marked with a line on top, to differentiate with respect to the Laguerre - Gauss modes, described in section 2.3.

Eq. (2.50). The normalization constant $\bar{C}_{l,q+1}$ normalizes the field in the sense of Eq. (2.18). The propagation constant $\bar{\beta}_{l,q+1}$ can be obtained by using $\bar{B}_{l,q+1}$ from Eq. (2.49).

It is now of interest to compare the Laguerre-Gauss field approximation with the more accurate numerical calculation. This is the topic of the next subsection.

## 2.5 Comparison between LG modes and numerical mode evaluation

There are several parameters that need to be compared in order to estimate the accuracy of the Laguerre-Gauss approximation. These values can be stated as follows:

- Field distribution
- Propagation constant
- Group delay

Each of them is dealt with in the next subsections:

### 2.5.1 Comparison of field distribution

The field distribution can be compared by estimating the overlap between two field distributions, where $\bar{e}_{l,q+1}(\rho,\phi)$ denotes the exact field distribution using the numerical mode solver and $e_{l,q+1}(\rho,\phi)$ denotes the Lagurre – Gauss approximation as given in section 2.3. If the fields are both normalized to unity as described in Eq. (2.18), the overlap can be formulated as:

$$C_{l,q+1} = \iint_A \bar{e}_{l,q+1}(\rho,\phi)\, e^*_{l,q+1}(\rho,\phi)\, dA, \tag{2.52}$$

where $A$ is the MMF cross-section. Since both field distributions have the same circumferential dependence, Eq. (2.52) can be simplified to:

$$C_{l,q+1} = \int_0^{\rho_e} \bar{\psi}_{l,q+1}(R)\, \psi^*_{l,q+1}(R)\, \rho d\rho. \tag{2.53}$$

The upper boundary $\rho_e$ should ideally go to infinity. This is of course numerically not possible and for this reason the integration is performed up to $\rho_e = 3 \times \rho_0$ [14]. To reasonably compare the field distributions, the parameter $\xi$ given in Eq. (2.29) is set for each MMF under consideration to have the same

[14] This value proved enough to ensure an error of less than 0.1%.

value of $\xi = 5.5\mu m$ [15]. From Eq. (2.29) this means the ratio of $\rho_0/NA$ needs to be set constant since:

$$\xi = \sqrt{\frac{\rho_0}{k_0 n_1(\lambda)\sqrt{2\Delta(\lambda)}}} = \sqrt{\frac{\rho_0}{k_0 NA}} \tag{2.54}$$

The parameter *NA* is the numerical aperture of the MMF and is defined as:

$$NA = \sqrt{n_1^2(\lambda) - n_2^2(\lambda)}. \tag{2.55}$$

Using these considerations for the simulation environment, the guided modes of the infinite parabolic profile and the truncated parabolic profile are compared. The simulation parameters are given in Table I. Each of the simulations is done, using a carrier wavelength of $\lambda_0 = 1.55\,\mu m$ .

TABLE I SIMULATION PARAMETERS FOR MMF OF INTEREST

| Parameter | Unit | Values | | | | |
|---|---|---|---|---|---|---|
| Number of modes per polarization | - | 6 | 10 | 15 | 21 | 55 |
| *NA* | - | 0.12 | 0.13 | 0.144 | 0.156 | 0.2 |
| $\rho_0$ | μm | 15 | 16.25 | 18 | 19.5 | 25 |
| *V* | - | 7.3 | 8.56 | 10.5 | 12.3 | 20.3 |
| $\Delta\tau_{max}$ | ps/km | 17 | 32 | 51 | 75 | 211 |

Fig. 8 shows exemplary the radial dependence of two modes, the $LP_{11}$- and $LP_{31}$ mode for the 15 mode fiber. The dashed curves represents the radial field using the LG – approximation given in Eq.(2.28), while the solid lines represent the radial field using the numerical calculation given section 2.4.

The LG – modes represent an excellent approximation for the lower order modes, while the higher order modes deviate a little, especially for values $R > 1$. This is now analyzed further using the relative mode mismatch, which is defined as:

$$\Delta C_{l,q+1} = 1 - C_{l,q+1}. \tag{2.56}$$

[15] This value is chosen due to the fact that a standard OM4 Fiber has this value.

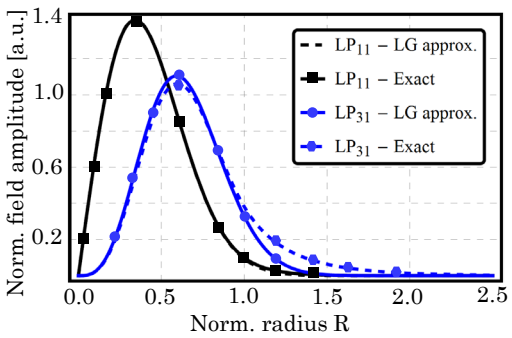


Fig. 8. Radial field distribution of the $LP_{11}$ mode and $LP_{31}$ mode for the 6 mode fiber using the values given in Table I. The dashed lines represent the distribution using the LG – approximation, while the solid lines represent the radial field distribution using the exact numerical approach. The field distribution is normalized to unity.

Fig. 9 shows the results. These show that the modes belonging to the mode group with highest DMG number *M* have the highest mismatch.

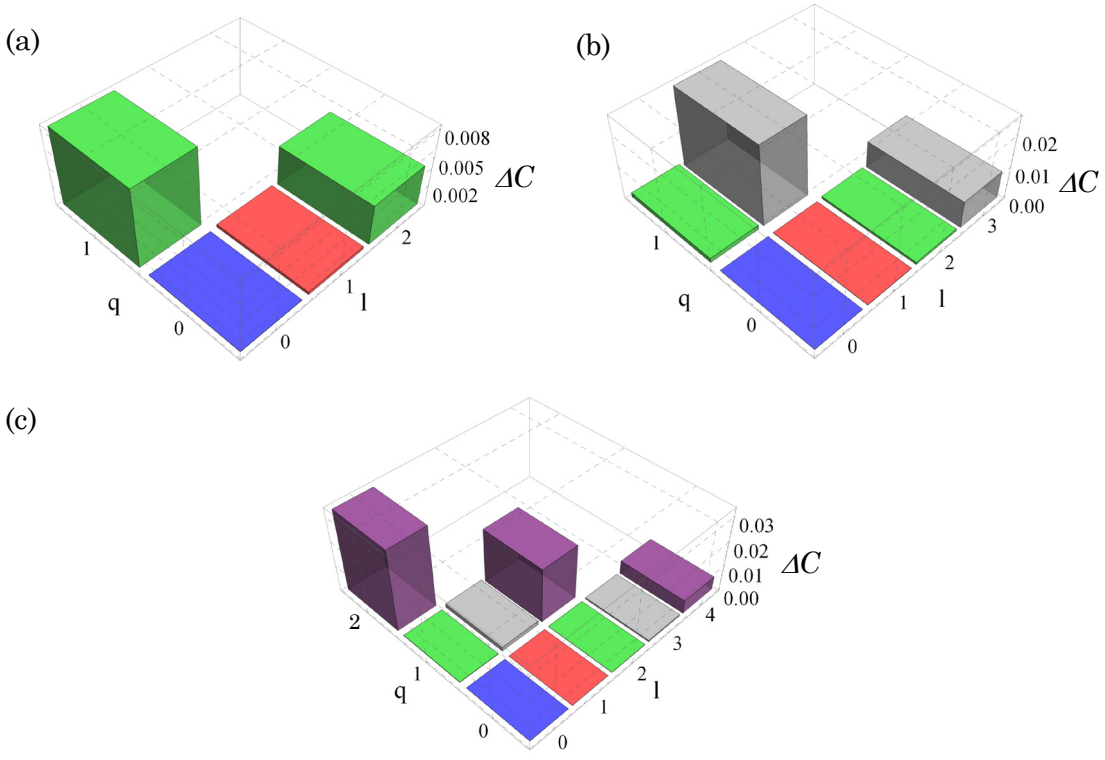


Fig. 9. Relative mode deviation for (a) 6 mode FMF; (b) 10 mode FMF; (c) 15 mode FMF

This can be attributed to the cladding, since modes with lower DMG number value $M$ are concentrated more around the axis region. As the number of modes increase, the relative mode mismatch increases for the highest mode group as shown in Fig. 9 (a) – (c). Nevertheless, the relative mode mismatch affects mostly the highest mode group, particularly those modes with higher radial order $q$. Since the calculation of the modal field distribution described in subsection 2.4 yields also the propagation constant, the comparison of the propagations constants will be evaluated in the next subsection.

### 2.5.2 Comparison of phase constants

The evaluation of the radial field distribution described in section 2.4 delivers additionally the normalized propagation constant $\overline{B}_{l,q+1}$. This is now compared to the normalized propagation constant $B_{l,q+1}$ of the Laguerre-Gauss modes at the carrier wavelength of $\lambda_0 = 1.55\,\mu\text{m}$. Fig. 10 shows the square of normalized propagation constant $B$ as function of DMG number $M$[16] for a 15 mode few mode fiber (FMF) and a 55 mode MMF. First it is possible to see that $B^2$ is equal for all modes within one DMG as expected in the Laguerre-Gauss approximation. This is also the case for the exact solution, except for the highest DMG, since the individual modes within this mode group experience the cladding differently, as discussed in the previous subsection. In these two particular examples the standard deviation of $B^2$ within the mode belonging to the highest DMG number $M$ is less than 0.007. The highest DMG number has the value of $M_{max} = 5$ for the 15 mode FMF and $M_{max} = 10$ for the 55 mode MMF.

[16] The numerical estimation does not yield degenerate values for $\overline{B}_{l,q+1}$ within the same mode group since the parabolic profile does not extend into infinity. Nevertheless their deviation is small so that an arrangement within so called quasi-principal mode groups is possible.

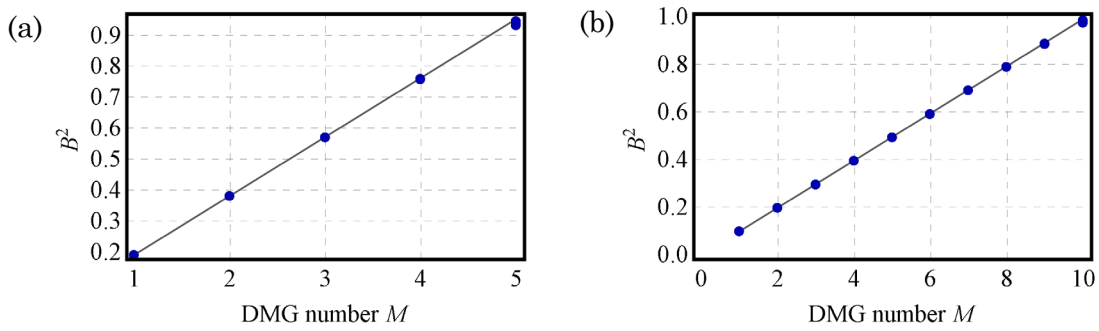


Fig. 10. Comparison between normalized propagation constant $B^2$ for a FMF guiding (a) 15 modes and (b) 55 modes using the Laguerre-Gauss appoximation in Eq. (2.35) represented by the solid gray line and the exact numerical calculation using blue dots. Solid line is only depicted for better overview since the DMG number $M$ is an integer number.

### 2.5.3 Comparison of differential group delay

The evaluation of the differential group delay per unit length $\tau_{l,q+1}$ requires the computation of the derivative with respect to angular frequency of the propagation constant $\overline{\beta}_{l,q+1}$. Instead of evaluating the derivative numerically, an alternative formulation is presented which uses the Hellmann-Feynman theorem. The group delay per unit length can be computed according to [36] as:

$$\tau_{l,q+1} = \frac{1}{2\beta_{l,q+1}} \frac{\partial \beta_{l,q+1}^2}{\partial \omega} = \frac{1}{2\beta_{l,q+1}} \iint_A \overline{e}_{l,q+1}^2(\rho,\phi) \frac{\partial n^2(\rho) k_0^2}{\partial \omega} dA. \qquad (2.57)$$

Here $A$ is the MMF cross-section which extends to infinity and the field distribution $\overline{e}_{l,q+1}$ is normalized as given in Eq. (2.18). Applying Eq. (2.1) and Eq. (2.42) to Eq. (2.57) yields:

$$\tau_{l,q+1} = \frac{N_1}{c} \frac{1}{n_1^2(\lambda)\left(1 - 2\Delta(\lambda) B_{l,q+1}^2\right)} \iint_A \overline{e}_{l,q+1}^2(\rho,\phi) n^2(\rho) dA. \qquad (2.58)$$

Fig. 11 shows the differential group delay $\Delta\tau_{l,q+1}$ as function of DMG number $M$. The differential group delay has been evaluated with respect to the fundamental mode as:

$$\Delta\tau_{l,q+1} = \tau_{l,q+1} - \tau_{0,1}. \qquad (2.59)$$

The dashed black line shows the results using the Laguerre-Gauss approximation given in Eq. (2.35) while the blue and green dots show the results using the exact numerical estimation for a 15 mode FMF and a 55 mode

MMF respectively. These results are in agreement with the calculations realized in [37] were the WKB approximation was used to calculate the DGDs of the different DMGs. The results in Fig. 11 show that mainly the two highest DMG have different DGD values induced by the presence of the cladding.

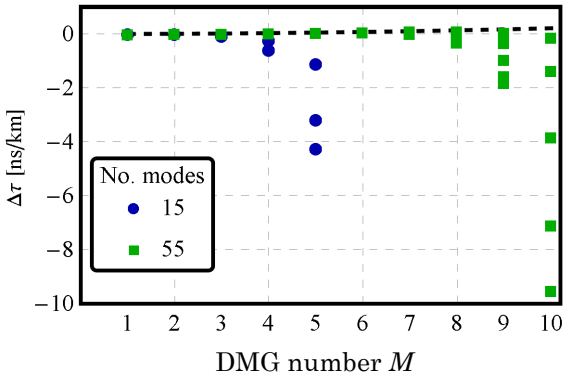


Fig. 11. Influence of the cladding upon the differential group delay. Black dashed line shows the results using the Laguerre-Gauss approximation, blue and green dots shows DGD for a 15 and 55 mode fiber respectively.

This is consistent with the results shown in section 2.5.1, where modes with larger DMG number experiences more of the cladding, which as a consequence, reduces the effective refractive index perception by the field (since the cladding has a lower refractive index).

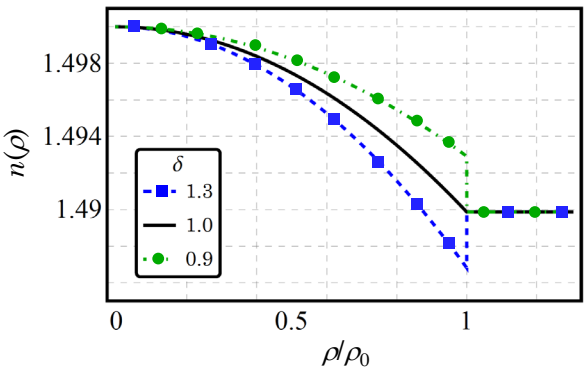


Fig. 12. Modification of the refractive index distribution as proposed by [38] by introducing the factor $\delta$, which describes the strength of the refractive index step between core and cladding boundary. To reduce the DGD spread only values of $\delta > 1$ have to be considered.

In the limit where the field propagates only in the cladding, its group velocity is given by $c/N_2$ . This value is higher than the fundamental mode group velocity for instance, which is located around the core axis region and therefore travels nearly at $c/N_1$ . This explains the negative values in Fig. 11 for modes located within the highest DMGs. The results in Fig. 11 show that the differential group delay can be as large as 10 ns/km, which is almost two orders of magnitude larger than calculated through the help of Eq. (2.35). To counteract the DGD spread induced by the cladding, a method was proposed by [38] in which a step is introduced between the core-cladding interfaces as shown in Fig. 12. This modified refractive index can be described as [38]:

$$n^2(\rho,\lambda) = \begin{cases} n_1^2(\lambda)\left(1 - 2\delta\Delta(\lambda)\left(\frac{\rho}{\rho_0}\right)^p\right) & 0 \le \rho < 1, \\ n_1^2(\lambda)\left(1 - 2\Delta(\lambda)\right) & \rho \ge 1, \end{cases} \tag{2.60}$$

where $\delta$ is the parameter that controls the step size at the core-cladding interface. Here only values above 1, i.e $\delta > 1,$ will be examined, since those have been reported to reduce the differential group delay which is essential in MDM applications to reduce the DGD spread. Fig. 13 shows the DGDs for all LP-modes in a 15 mode FMF as a function of the step values $\delta$. Using a value of $\delta = 2$ effectively reduces the maximal DGD spread from 4.2 ns/km to 140 ps/km[17] as shown in more detail in the inset of Fig. 13. These results might lead to the conclusion that increasing $\delta$ further might decreases the differential group delay. This is not the case as shown in [38], where a numerical routine is used to find the optimal $\delta$ value to minimize the overall DGD value.

[17] Here it is important to notice that the number of guided modes can be smaller for the same normalized frequency parameter $V$, if $\delta > 1$. This is because the cut off condition is shifted to higher $V$ values as shown in [38]. This has been compensated in Fig. 13 by increasing $V$ while maintaining $\xi$ constant to maintain the total number of guided modes 15.

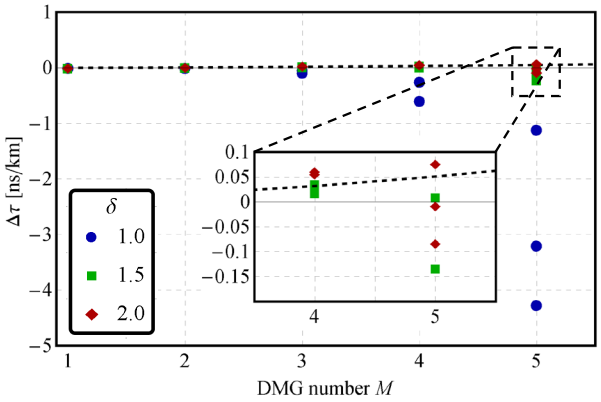


Fig. 13. DGDs for FMFs guiding 15 modes for different step values $\delta$. The maximal differential group delay of the the highest mode group is reduced to 140 ps/km using a value of $\delta = 2$. The dashed line shows the values for the infinite extended parabolic profile. The discrete values are joined only for better overview.

The field distribution of the $LP_{01}$ and $LP_{03}$ mode using the Laguerre-Gauss modes and the fields estimated using the step parameter $\delta = 2$ are shown in Fig. 14. As expected, the field mismatch is reduced and the field distribution is almost identical, even for the mode belonging to the higher order mode group. Here it needs to be pointed out, that the step, described by the parameter $\delta$, also affects the number of guided modes.

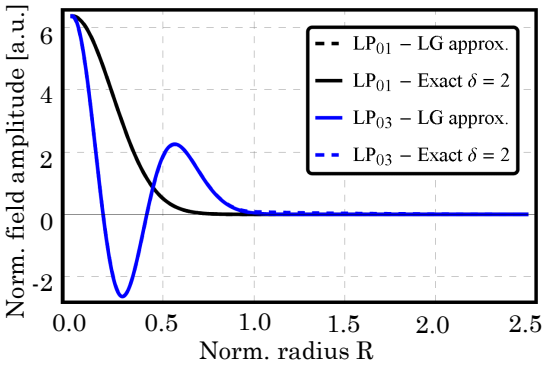


Fig. 14. Field distribution of the $LP_{01}$ and $LP_{03}$ modes using the Laguerre Guassian and exact numerical calculation with $\delta = 2$. Field distribution are almost identical. Field mismatch is for the $LP_{03}$ modes equal to $C = 0.002$ (Compared to a value of $C = 0.03$ in Fig. 9 (c))

To compare the field overlap of the higher order modes, the normalized frequency parameter $V = 10.5$ had to be increased to value of $V = 14.3$ so that

the modes to be compared are guided. The $V$ parameter was increased by increasing $\rho_0$ and $NA$ in such a manner, to keep the ratio $\rho_0 / NA$ constant. From these results it is possible to conclude, that the Laguerre-Gauss approximation is an excellent approximation to describe the field distribution inside a FMF, as well as DGDs of the individual modes. Now that the parabolic index profile has been analyzed and the Laguerre-Gauss approximation has been verified, it is worthwhile analyzing if the same field distribution can be used to describe profiles with near parabolic index profile. For this reason, the analysis is extended to power law profiles which is discussed in the next subsection.

## 2.6 MMF with power law profiles

As mentioned already in section 2.3.1, the field distribution of a FMF with a truncated power law profile can be very similar to the field distribution of a FMF with an infinitely extended parabolic index profile. This is now verified by evaluating the field mismatch $\Delta C$ from Eq. (2.56) for different truncated power law profiles. The variation is realized here for a 15 mode FMF in the range of $p = \{1.8, 1.9, \ldots, 2.4\}$ and the results are shown in Fig. 15. The mismatch is evaluated between the Laguerre-Gauss modes and the numerical calculation.

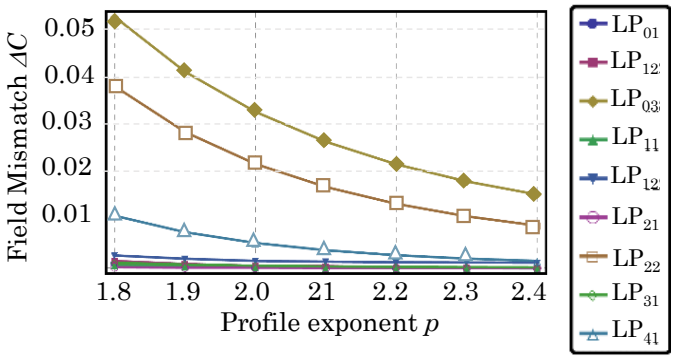


Fig. 15. Field mismatch $\Delta C$ between Laguerre-Gauss modes and numerical calculation of field distribution for different profile exponents' $p$.

As expected, the relative mismatch $\Delta C$ is relatively small for all guided modes. The highest mismatch value is given for the $LP_{03}$ mode which is in agreement with the results presented in section 2.5.1. With this analysis this section is finalized and the results will be summarized in the next subsection.

## 2.7 Summary

With these results this chapter is concluded and the main results can be summarized as follows:

- The scalar wave equation can be used if the normalized refractive index difference $\Delta(\lambda)$ is much smaller than unity, i.e. if $\Delta(\lambda) << 1$ holds. In this case the FMF is said to be weakly guiding.
- The field distribution is described using the Laguerre-Gauss approximation. The relative field mismatch $\Delta C$ between the Laguerre-Gauss modes and numerical calculations does not increase above 5% for the considered FMFs, even if the profile deviates slightly from parabolic profile.
- Modes belonging to the two highest order DMG are mostly affected by the cladding. This can be seen in the DGDs spread, which can increase as much as 100 times the value given by the LG-Modes. This can be efficiently compensated using the refractive index distribution shown in Fig. 12 such as to have a much smaller deviation from the LG-approximation. In this case, the field distribution is even more accurately described by the Laguerre-Gauss modes. Nevertheless, it is necessary to increase the $V$ value to maintain the number of guided modes equal.

Under the assumption that the FMF under consideration has a refractive index profile as in Fig. 12 with a value of $\delta \approx 2$ , the LG-modes and its propagation values are a very good approximation and will be used in the following chapters to simulate the FMF of interest unless stated otherwise.

# 3. Propagation and mode coupling in MMF

The modal field distributions that were given in the last chapter are modes that can actually be excited but exist only if the MMF is free from any imperfection. Imperfections are always present in MMF and cause modes to couple. Some of these imperfections are for example micro-bendings, splices, MMF core deformations like ellipticity, refractive index variations, amongst others. Micro-bendings and splices will be dealt with here. To understand some of the limitations induced by modal coupling one imagines the excitation of a single mode at the beginning of the MMF. After some distance the power will be transferred to other guided modes while some of the power is transferred to non-guided modes [39]. Power transferred to non-guided modes results in so called coupling losses while power transferred to other guided modes can result for example in signal distortion. While MMF were studied extensively in the 70s using power coupling models [40,41,42] which effectively describes power redistribution as function of time and MMF length and MMF bandwidth increase due to modal coupling, these models fail to consider phase effects which are important when using coherent light sources or higher order modulation formats.

This chapter deals with the modeling of the coherent transmission link, limiting the analysis to linear effects in the MMF. Linear propagation inside the MMF will be described first, taking into account phase effects and modal dispersion, while introducing the matrix notation. The orthogonality condition described in section 2.2 will be reformulated for this purpose, simplifying its evaluation while using the matrix formalism, as well as deriving the formula for the weighting coefficients.

The analysis is then extended to include modal coupling induced by micro-bendings and splices. Two different mode coupling procedures are

compared and analyzed: the ideal mode approach and the local mode approach as shown in Fig. 16 (a) and (b) respectively. The ideal mode approach relies on approximating the perturbed MMF by using one set of modes, which are the eigenmodes of the ideal MMF shown in Fig. 16 (a) by the dashed lines.

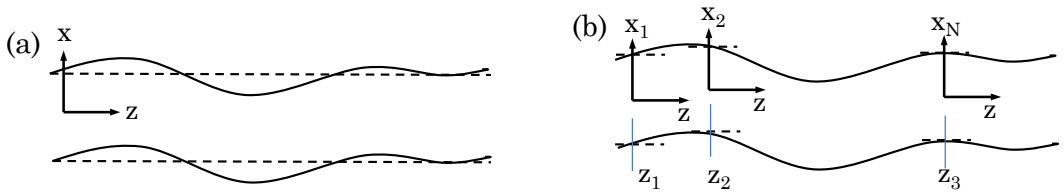


Fig. 16. MMF with distorted core – cladding interface described in terms of (a) ideal modes; (b) normal local modes

The actual MMF depicted in Fig. 16 (a) by the solid line is then viewed as a perturbation of the ideal MMF. The local normal mode approach relies on partitioning the MMF in many segments. Each segment is then described by a local coordinate system as depicted in Fig. 16 (b) and the eigenmodes are computed for a fictitious MMF depicted in Fig. 16 (b) by the dashed lines. Coupling can then be estimated by evaluating the overlap integral between the eigenmodes from MMF section $i$ to MMF section $j$. While both models rely on partitioning the MMF in small sections, it will be evident that the use of the local mode approach brings some benefits since coupling losses are automatically included in the description. In addition, it will be shown that it is possible to drastically reduce the computational effort of the model by reducing the total amount of MMF fiber sections if the overall induced coupling loss is maintained constant. This will be verified thoroughly by analyzing the evolution of the DGDs of the MMF, the MMF bandwidth and mode dependent loss. The chapter ends by comparing the results to the results presented in [40,41] which use the coupled power models.

## 3.1 Ideal propagation and matrix notation of the MMF transmission system

An arbitrary electric field at the input $(z=0)$ of the MMF can be expanded in terms of the MMF eigenmodes as [28]:

$$e(\rho,\phi)=\sum_{l,q} a_{l,q+1} e_{l,q+1}(\rho,\varphi), \tag{3.1}$$

where $a_{l,q}$ is the weighting coefficients and the summation extends over all guided modes. If Eq. (3.1) is now multiplied with $e^{*}_{l',q'}(r,\phi)$ and integrated over the complete MMF cross-section, the following equation is obtained:

$$\iint_A e(\rho,\phi) e^{*}_{l',q'+1}(r,\phi)\,dA=\sum_{l,q} a_{l,q+1}\iint_A e_{l,q+1}(\rho,\phi) e^{*}_{l',q'+1}(r,\phi)dA. \tag{3.2}$$

Using the orthogonality condition given in Eq. (2.17) and the fact that in Eq. (3.2) only terms with $l=l'$ and $q=q'$ remain, the following relation can be formulated for the excitation coefficients [28]:

$$a_{l,q}=\frac{\iint_A e(\rho,\phi) e^{*}_{l',q+1'}(r,\phi)\,dA}{\iint_A e_{l,q+1}(\rho,\phi) e^{*}_{l',q'+1}(r,\phi)\,dA}. \tag{3.3}$$

Identically, the field at the output of the MMF can be expressed as an expansion of the MMF eigenmodes with different weighting coefficients $b_{q,l}(z,\omega)$ as:

$$e_{out}(\rho,\phi,z,\omega)=\sum_{l,q} b_{l,q+1}(z,\omega) e_{l,q+1}(\rho,\phi). \tag{3.4}$$

The weighting coefficients $b_{l,q+1}(z,\omega)$ are now frequency and z – dependent since they contain the propagation information. In the case of ideal propagation, that is, the case of a perfect straight MMF, the input and output field can be described using vector notation as:

$$\vec{\mathbf{b}}(z,\omega)=\exp\left(-j\mathbf{B}(\omega)L\right)\vec{\mathbf{a}}(z=0). \tag{3.5}$$

Here $L$ describes the MMF length and the matrix $\mathbf{B}(\omega)$ is square matrix given by:

$$\mathbf{B}(\omega)=\begin{pmatrix}\beta_{01}(\omega) & 0 & \cdots & 0\\ 0 & \beta_{11}(\omega) & 0 & \vdots\\ \vdots & 0 & \ddots & 0\\ 0 & \cdots & 0 & \beta_{l_{max},q_{max}+1}(\omega)\end{pmatrix} \tag{3.6}$$

with diagonal entries given by the uncoupled propagation coefficients $\beta_{l,q+1}(\omega)$ described in Eq. (2.34). The first matrix entry is the propagation constant of the $LP_{01}$ fundamental mode. The second and third diagonal entry correspond to the odd and even $LP_{11}$ mode, which form the second DMG. The next entries correspond to the propagation constants $\beta_{l,q+1}(\omega)$ of all modes belonging to the third degenerate mode group, where all possible combinations of $q$ and $l$ are taken into account that yield $M = 2q + l + 1 = 3$, starting with lowest $l$ value and ending with the highest. This is done for all guided modes, so that the matrix $\mathbf{B}(\omega)$ can be viewed as a block diagonal matrix, where each block matrix is diagonal as well and contains the propagation constants of one DMG. The matrix exponential is defined in terms of a Taylor series as [30]:

$$\exp\left[-j\mathbf{B}(\omega)L\right]=\sum_{k=0}^{\infty}\left(-j\mathbf{B}(\omega)L\right)^{k}/k!. \tag{3.7}$$

The vector $\vec{\mathbf{a}}(z=0)=\left[a_{0,1}(z=0),a_{1,1}(z=0),\ldots,a_{l_{\max},q_{\max}+1}(z=0)\right]^{T}$ contains the excitation coefficients of all guided eigenmodes at the input of the MMF, denoted here with $z=0$. Since each weighting coefficient within the vector $\vec{\mathbf{a}}(z=0)$ describes indirectly the presence of a field distribution, the orthogonality condition given in Eq. (2.17) reduces in this vector space to a scalar product between two vectors as:

$$\vec{\mathbf{a}}_{l,q+1}^{T}\vec{\mathbf{a}}_{l',q'+1}^{*}=0, \tag{3.8}$$

if $l\neq l'$ or $q\neq q'$. This can be understood easily if one takes a closer look to the following example: the vector $\vec{\mathbf{a}}_{0,1}=\left[a_{0,1},0,\ldots,0\right]^{T}$ contains the weighting coefficient of the $LP_{01}$ mode and the vector $\vec{\mathbf{a}}_{0,2}=\left[0,\ldots,0,a_{0,2},0,\ldots,0\right]^{T}$ contains the weighting coefficient of the $LP_{02}$ mode. If the scalar product between the vector $\vec{\mathbf{a}}_{0,1}$ and the vector $\vec{\mathbf{a}}_{0,2}^{*}$ is computed, it's clear that the result is zero:

$$\vec{\mathbf{a}}_{0,1}{}^{T}\vec{\mathbf{a}}_{0,2}^{*}=0 \tag{3.9}$$

This vector scalar product describes therefore the orthogonality condition given in Eq. (2.18). In addition, a second variation of the orthogonality condition can be formulated, by leaving out the conjugation of the second vector as:

$$\vec{\mathbf{a}}^{T}_{l,q+1}\vec{\mathbf{a}}_{l',q'+1} = 0 \tag{3.10}$$

A rigorous treatment of this mathematical formulation would require the introduction of the Heisenberg notation as done for example in [20,43]. This will not be done here to maintain simplicity.

Having introduced the matrix notation for the propagation within the MMF, the analysis is now extended to include modal coupling. These two coupling mechanism behave identical in MMF with parabolic index profile as will be shown in the next subsection by transforming the refractive index.

## 3.2 Refractive index transformation

If a MMF contains micro-bendings, it is possible to assign a bending radius to each bend. Each bending is therefore described by a bending radius in *x*- and *y*- direction, denoted as $R_x$ and $R_y$[18] respectively. Fig. 17 (a) shows exemplary a MMF segment with a bending radius in *y*-direction.

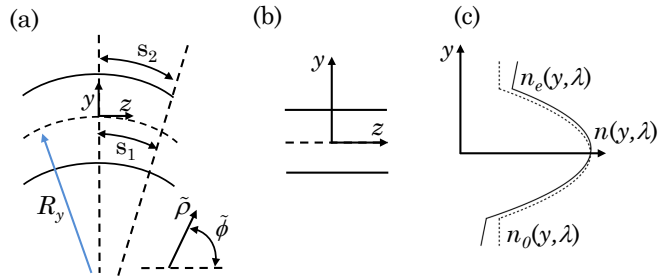


Fig. 17. Transformation of a MMF segment with (a) micro-bending with refractive index $n_0(y,\lambda)$ in y- direction into a (b) straight MMF segment with refractive index $n_e(y,\lambda)$.The effective refractive index $n_e(y,\lambda)$ induced by the bending is shown in (c) in the case of a truncated parabolic profile.

The goal is to transform the geometrical change in the MMF as shown in Fig. 17 (a) into a refractive index change so that the MMF segment might be considered as a straight section as shown in Fig. 17 (b). The resulting refractive index profile is shown in Fig. 17 (c) with the solid line. This transformation is described in the next paragraph.

As the wave travels along a bent MMF segment, it is necessary for the wave to have a higher phase velocity at the outer core-cladding boundary, than in the core axis for example, in order to preserve the phase front. This requires a smaller phase constant at the core-cladding boundary. Using the polar coordinate system, which lies here in the y-z plane[19], the outer and center arc lengths in Fig. 17 (a), denoted as $s_1$ and $s_2$, are given as:

$$s_{1,2} = \int_0^{\tilde{\phi}_0} \tilde{\rho} d\tilde{\phi} = \tilde{\rho}_{1,2}\tilde{\phi}_0, \tag{3.11}$$

[18] The bending radii considered here are in the order of magnitude of meters. In this sense it only makes sense to talk about coupling losses, since they exceed radiation losses as mentioned in [45].

[19] The same procedure can be realized for the x-z plane. For simplicity only the y-dependency is discussed.

where $\tilde{\rho}$ and $\tilde{\phi}$ describe the axial and angular dependence[20] and $\tilde{\phi}_0$ is the integration limit for the angular dependency. From Fig. 17 (a), it is possible to identify $\tilde{\rho}_1$ with $R_y$. The phase front is preserved if:

$$\begin{aligned} \beta(R_y) R_y \tilde{\phi}_0 &= \beta(\tilde{\rho}_2)\tilde{\rho}_2\tilde{\phi}_0, \\ \beta(\tilde{\rho}_2) &= \beta(R_y)\left(\frac{R_y}{R_y + y}\right), \\ \text{with } \tilde{\rho}_2 &= R_y + y. \end{aligned} \tag{3.12}$$

The transverse wave number for the bended MMF $k_{t,b}$ is given as:

$$k_{t,b}^2 = k_0^2 n_0^2(x,y,\lambda) - \beta^2(x,y). \tag{3.13}$$

The transverse wave number for the equivalent straight MMF segment $k_{t,s}$ is given as:

$$k_{t,s}^2 = k_0^2\left(n_0^2(x,y,\lambda) + n_p^2(x,y,\lambda)\right) - \beta_s^2. \tag{3.14}$$

Both equations describe the same problem, which is why Eq. (3.13) and Eq. (3.14) are equated as:

$$k_{t,b} \doteq k_{t,s}. \tag{3.15}$$

This yields the following relation:

$$\begin{aligned} \beta^2(\rho_2) &= \beta_s^2 - k_0^2 n_p^2(x,y,\lambda), \\ \left(1 - 2\frac{y}{R_y}\right)\beta^2(R_y) &= \beta_s^2 - n_p^2(x,y,\lambda), \end{aligned} \tag{3.16}$$

where the series expansion of $(1/1 + yR_y^{-1})^2 \approx 1 - 2yR_y^{-1}$ has been used[21]. Under the assumption that $\beta^2(R_y) = \beta_s^2$ the refractive index perturbation is obtained as [27]:

$$n_p^2(x,y,\lambda) = \left(\frac{2y}{R_y} + \frac{2x}{R_x}\right) n_1^2(\lambda). \tag{3.17}$$

Therefore, the refractive index change induced by a bending is a linear tilt as shown in Fig. 17 (c). It is possible to reformulate this further by noting that:

[20] Not to be mistaken with the MMF coordinate system used in Eq. (2.50) for example.
[21] This expansion is justified if $\{R_x, R_y\} \gg \{x, y\}$.

$$\begin{aligned} n_e^2(x,y,\lambda) &= n_0^2(x,y,\lambda) + n_p^2(x,y,\lambda) \\ &= n_1^2(\lambda)\left(1-2\Delta(\lambda)\frac{x^2+y^2}{\rho_0^2}\right) + n_1^2(\lambda)\left(\frac{2x}{R_x}+\frac{2y}{R_y}\right) \\ &= n_1^2(\lambda)\left[1-2\Delta(\lambda)\left(\frac{x^2}{\rho_0^2}-\frac{x}{\Delta(\lambda)R_x}+\frac{y^2}{\rho_0^2}-\frac{y}{\Delta(\lambda)R_y}\right)\right] \\ &\approx n_1^2(\lambda)\left[1-2\Delta(\lambda)\left(\frac{x-\Delta x}{\rho_0}\right)^2-2\Delta(\lambda)\left(\frac{y-\Delta y}{\rho_0}\right)^2\right]. \end{aligned} \tag{3.18}$$

The offset in $x$- and $y$-direction is given as:

$$\Delta x = \frac{\rho_0^2}{2\Delta(\lambda)R_x};\ \Delta y = \frac{\rho_0^2}{2\Delta(\lambda)R_y}. \tag{3.19}$$

With Eq. (3.18) it is shown that a micro-bend can be viewed as an offset, where the offset is inversely proportional to the micro-bending radius. A more rigorous proof of this concept can be formulated by analyzing the power coupling spectrum, which is shown in detail in annex A.2.

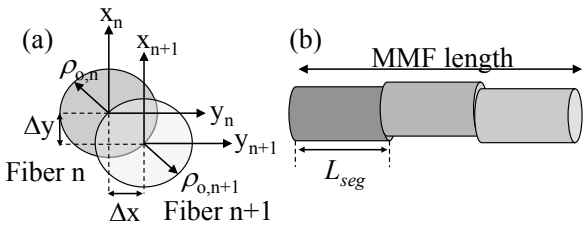


Fig. 18. Fiber mismatch in x- and y-direction. The distribution in each direction is Gaussian; (b) Complete MMF made out of concatenation of ideal MMF segments.

This transformation shows an important relation. Micro-bendings can be modeled as a series of mismatched MMF segments with offset $\Delta x$ and $\Delta y$ and can be interpreted as splices as in Fig. 18, if the refractive index profile has a parabolic shape. If actual splices are included in the transmission link, they can be modeled by an additional mismatch. The description of the coupled mode theory in terms of ideal modes will be discussed in the following subsection.

## 3.3 Description in terms of ideal modes

The main idea behind this approach is to model the MMF in terms of one set of orthogonal modes which describe the MMF in the absence of any perturbation. Fig. 16 (a) shows the case of a MMF in which the core-cladding interface is deformed. The dashed line shows the undistorted MMF and its eigenmodes obey the homogeneous scalar wave equation given in Eq. (2.16). As already shown in chapter 2, the Laguerre-Gauss modes describe the eigenmodes of the MMF in good approximation with parabolic index profile. In presence of a perturbation, as shown in Fig. 16 (a) by the solid line, the modes couple and their propagation can be formulated in matrix notation as [39]:

$$\frac{\mathrm{d}\vec{\mathbf{a}}(z)}{\mathrm{d}z} + j\mathbf{B}(\omega)\vec{\mathbf{a}}(z) = \boldsymbol{\kappa}(z)\vec{\mathbf{a}}(z). \tag{3.20}$$

Here no coupling between back- and forward propagating waves is assumed and the matrix $\boldsymbol{\kappa}(z)$ describes mode coupling between the guided modes and is length dependent. Equation (3.20) describes coupling within guided modes only since coupling into non guided modes is not included. As a consequence, the coupling matrix $\boldsymbol{\kappa}(z)$ is unitary. To simplify Eq.(3.20), the MMF is partitioned into small sections. Within one section, the coupling matrix $\boldsymbol{\kappa}(z)$ can be considered constant and is therefore z-independent. The evolution of the vector $\vec{\mathbf{a}}$ within one segment is therefore given as:

$$\frac{\mathrm{d}\vec{\mathbf{a}}(z)}{\mathrm{d}z} + j\mathbf{B}(\omega)\cdot\vec{\mathbf{a}}(z) = \boldsymbol{\kappa}_n\cdot\vec{\mathbf{a}}(z). \tag{3.21}$$

The index $n$ denotes here the $n$th MMF segment. The coupling coefficients of the matrix $\boldsymbol{\kappa}_n$ can be estimated as [27,39]:

$$\kappa^{(n)}_{l,q+1,l',q'+1} = \frac{-jk_0}{2n_1(\lambda)}\int_{-\infty}^{\infty}\int_{-\infty}^{\infty} n_p^2(x,y,\lambda)e^*_{l,q+1}(x,y)e_{l',q'+1}(x,y)\,dxdy. \tag{3.22}$$

The perturbed refractive index $n_p$ describes the perturbation in terms of the refractive index change and is given as described in Eq. (3.17) for a micro-bending. Eq. (3.22) is therefore given as:

$$\kappa^{(n)}_{l,q+1,l',q'+1} = \frac{-jk_0}{R_x}n_1(\lambda)\int_{-\infty}^{\infty}\int_{-\infty}^{\infty} xe^*_{l,q+1}(x,y)e_{l',q'+1}(x,y)\,dxdy. \tag{3.23}$$

The evolution of the input vector $\vec{\mathbf{a}}(z=0)$ can be formulated now by integrating Eq. (3.21) over a small segment of length $L_{seg}$ since $\mathbf{B}(\omega)$ and $\boldsymbol{\kappa}_n$ are z – independent. This yields as suggest by [44]:

$$\vec{\mathbf{b}}\left(z=L_{seg},\omega\right)=\mathbf{T}_{seg,n}\left(z=L_{seg},\omega\right)\vec{\mathbf{a}}\left(z=0\right). \tag{3.24}$$

The vector $\vec{\mathbf{b}}\left(z=L_{seg},\omega\right)$ denotes the evolution of the vector $\vec{\mathbf{a}}$ after a single MMF segment and $\mathbf{T}_{seg,n}(z,\omega)$ is the transfer matrix describing propagation and coupling given as:

$$\mathbf{T}_{seg,n}\left(z=L_{seg},\omega\right)=\exp\left(-j\mathbf{B}\left(\omega\right)L_{seg}+\boldsymbol{\kappa}_n L_{seg}\right). \tag{3.25}$$

The complete transfer matrix is therefore given as a product of $N$ segment matrices

$$\mathbf{T}_I\left(z,\omega\right)=\prod_{n=1}^{N}\mathbf{T}_{seg,n}\left(z=L_{seg},\omega\right). \tag{3.26}$$

The index $I$ stands for ideal modes. The rank of the transfer matrix $\mathbf{T}_I\left(z,\omega\right)$ equals the number of guided modes $D$ and contains $M_{\max}$ different mode groups. To incorporate coupling losses in $\mathbf{T}_I\left(z,\omega\right)$ it is assumed that the highest order mode group with DMG number $M_{\max}$ couples into the first non-guided mode group $M_{\max}$+1. This idea is motivated on the work presented in [45], where micro-bending losses were estimated for single mode fibers. There it was shown that coupling losses can be calculated by coupling the fundamental $LP_{01}$ mode with the first non - guided mode, the $LP_{11}$ mode. On this basis, the idea is extended and applied to a MMF. To obtain the modes of the first non-guided mode group, a virtual MMF is evaluated, which guides $M'_{\max}=M_{max}+1$ mode groups. This MMF is created by increasing the $V$ parameter, while maintain the ratio of $\rho_0 / NA$ constant. This ensures that all modes contained within the mode groups $M' \le M'_{\max}-1$ have exactly the same spatial distribution as the actual MMF. Coupling into these modes is then evaluated within each segment by using Eq. (3.23). The correctness of this assumption will be shown later as the two models are compared. The rank of the matrix $\mathbf{T}_{seg,n}\left(z,\omega\right)$ is now increased by an additional mode group. The number of modes contained now

in $\mathbf{T}^{+}_{seg,n}(z,\omega)$ [22] is increased from $D$ to $D^{+}$ which can be evaluated by using the following relation:

$$D^{+} = \sum_{i=1}^{M_{max}+1} i. \tag{3.27}$$

Further on it is assumed that the power coupled into the modes with DMG number $M'_{\max}$ does not couple back into the guided modes. This is therefore considered as coupling loss and is modeled by setting the matrix entries to zero after each segment. This can be achieved by multiplying the matrix $\mathbf{T}^{+}_{seg,n}(z,\omega)$ on both sides with the matrix $\mathbf{L}$ defined as:

$$\mathbf{L} = \begin{pmatrix} \mathbf{I} & \mathbf{0}_D \\ \mathbf{0}_D^T & \mathbf{0}_s \end{pmatrix}. \tag{3.28}$$

The matrix $\mathbf{I}$ is a square identity matrix of rank $D$, the matrix $\mathbf{0}_D$ is rectangular zero matrix of size $D \times (D^{+} - D)$ and $\mathbf{0}_s$ is a square zero matrix of Rank $D^{+} - D$. The matrix $\mathbf{0}_s^T$ is the transpose of $\mathbf{0}_D$. The complete transmission matrix is therefore given as:

$$\mathbf{T}^{+}_{I}(z,\omega) = \prod_{n=1}^{N} \mathbf{L} \cdot \mathbf{T}^{+}_{seg,n}(z = L_{seg},\omega) \cdot \mathbf{L}. \tag{3.29}$$

The evolution of the input field, given by the vector $\vec{\mathbf{a}}$, can now be described by:

$$\vec{\mathbf{b}}(z,\omega) = \mathbf{T}^{+}_{I}(z,\omega) \cdot \vec{\mathbf{a}}(z = 0). \tag{3.30}$$

Eq. (3.30) can now be used to describe the propagation of an arbitrary input field, given by the vector $\vec{\mathbf{a}}(z = 0)$.

[22] The + indicates here that the matrix has an increased rank. As an example consider a MMF guiding 55 modes, divided into 10 mode groups. The virtual MMF contains 11 mode groups and 66 modes. The last ten mode contained in the real MMF couple to the 11 new modes contained in the new virtual mode group. This calculation assumed modes in only one polarization direction.

## 3.4 Description in terms of normal local modes

The description in terms of normal local modes is based on the idea of using a local coordinate system as shown Fig. 16 (b). At each position $z = z_i$ the perturbed MMF is approximated by the unperturbed MMF shown with the dashed lines. As mentioned in section 3.1, the effective refractive index $n_e(x,y,\lambda)$ of a micro-bend can be viewed as a splice mismatch as shown in Fig. 18. At each position $z_i$, the eigenmodes are therefore computed and expanded in terms of the eigenmodes of the next section $z_{i+1}$ to calculate the overlap and with it the coupling coefficients. In each ideal segment $n$, the scalar wave equation (for one polarization direction, here the $x$-direction)

$$\left\{\Delta_t + n_{e,n}^2 k_0^2 - \beta_{r,n}^2\right\} e_x = 0 \tag{3.31}$$

is satisfied. One possibility to solve this problem is by using the fact that each micro-bend is equivalent to MMF offset as given in Eq.(3.18). By using a separate coordinate system for each MMF section as shown in Fig. 18 (a), the scalar wave equation is satisfied by the Laguerre-Gauss-modes. The propagation constants within each ideal MMF segment are given as described in section 2.3.1. The Laguerre-Gauss-modes are described in the $n$-th segment with a coordinate system denoted by $\rho_n$ and $\phi_n$. The coupling coefficients can be formulated using overlap integrals as [32,46]:

$$K_{l,q+1,l',q'+1}^{(n)} = \int_{-\infty}^{\infty}\int_{-\infty}^{\infty} e_{l,q+1}^{(n)}(\rho_n,\phi_n)\, e_{l',q'+1}^{*(n+1)}(\rho_{n+1},\phi_{n+1})\, dA. \tag{3.32}$$

Here it is assumed that fields are normalized to unity. These coefficients[23] form the coupling matrix denoted by $\mathbf{K}_n$ which describes coupling between section $n$ and $n+1$. The coupling matrix $\mathbf{K}_n$ is not unitary. (unlike $\boldsymbol{\kappa}_n$ in the previous section), Therefore coupling losses between two adjacent MMF sections are implicitly included in matrix $\mathbf{K}_n$ and as shown later, describes effectively

[23] The coupling coefficients can be evaluated for offset values numerically. If very small offsets are used, an analytical approach should be used since numerical inaccuracy will cause matrices to have norm larger than one. As a consequence, cascading them will lead to gain in the transmission system. One approach to solve these integrals analytically is by expanding the Laguerre-Gauss mode into Hermite-Gauss modes as explained in [32]. The coupling integral between these modes can be evaluated analytically and then retransformed into Laguerre-Gauss modes.

coupling induced losses. Propagation within one segment is described by the diagonal matrix $\mathbf{M}(\omega)$ given as:

$$\mathbf{M}(z,\omega) = \exp(-j\mathbf{B}(\omega)z). \tag{3.33}$$

Here $\mathbf{B}(\omega)$ is exactly the same matrix as described in Eq. (3.6). Propagation and coupling is then described by:

$$\mathbf{T}_{LN}(z,\omega) = \prod_{n=1}^{N} \mathbf{M}(z,\omega)\cdot\mathbf{K}_n. \tag{3.34}$$

Here the index *LN* stands for local normal modes and basically describes a concatenation of segments with piecewise contants curvature. Equation (3.29) and Eq. (3.34) describe the evolution of the modes in the presence of modal coupling induced by micro-bends and splices in terms of ideal modes or local normal modes. To take into account mode coupling effects within one mode group and or fiber variations due to temperature, the following random matrices are introduced which are described in the next subsection.

## 3.5 Random matrices

The optical phase of light propagating though the MMF changes if the temperature changes inside the MMF. This has mainly two causes [47]: the change in fiber length through thermal expansion or contraction and the refractive index change due to temperature variation. This phase change $\Delta\varphi$ per unit temperature $\Delta T$ and unit length $\Delta l$ is given as [47]:

$$\frac{\Delta\varphi}{\Delta T\,\Delta l} = \frac{2\pi}{\lambda}\left(\frac{n}{\Delta l}\frac{\partial \Delta l}{\partial T} + \frac{\partial n}{\partial T}\right). \tag{3.35}$$

Using the values presented [48] for the wavelength of $\lambda = 1.55\mu\text{m}$, it is possible to estimate a value of [24]:

$$\frac{\Delta\varphi}{\Delta T\,\Delta l} = 48 \text{ radians} / {}^{\circ}C / m. \tag{3.36}$$

This values is only valid for the fundamental mode in a SMF. In the case of a MMF, it is probable that this value varies slightly for each mode. A slight temperature variation causes a significant phase change so that a random matrix approach is chosen to model the phase change induced by temperature. This diagonal matrix is therefore given as:

$$\mathbf{R}_D = \exp\left(-j\,\mathrm{diag}\left(\zeta_1, \zeta_2, \ldots, \zeta_Y\right)\right), \tag{3.37}$$

where each elements $\zeta_i$ is uniformly distributed with the boundaries $0 - 2\pi$. Due to the results presented in [48], it is reasonable to assume that this matrix is constant over frequency and is therefore equal for all frequency components.

An additional effect which is modeled here using random matrices is coupling between modes within one degenerate mode group. Since all modes within one mode group have the same propagation constant it is likely for these modes to couple uniformly as reported by [22,49]. To model this process, it is necessary to generate unitary matrices. This can be modeled by using the procedure described in [50]. The basic idea behind this procedure is to generate a random unitary matrix. Using the QR-decomposition, any matrix $\mathbf{Z}$ [25] can be decomposed as:

---

[24] Here the value of $\Delta l^{-1}\partial\Delta l / \partial T$ has been neglected since it is one order of magnitude smaller than $\partial n/\partial T$ according to [47]

[25] The arbitrary matrix $\mathbf{Z}$ is generated using Mathematica random number generation.

$$\mathbf{Z} = \mathbf{QR}. \tag{3.38}$$

Here the matrix $\mathbf{R}$ is an upper triangular matrix and invertible. The $\mathbf{Q}$ matrix belongs to the unitary group, $\mathbf{Q} \in U(n)$ and is therefore unitary. The matrix generated through this procedure will be used to couple within one mode group. The resulting mode group coupling matrix is a block matrix given as:

$$\mathbf{R}_U = \begin{pmatrix} 1 & 0 & \cdots & 0 \\ 0 & \mathbf{Q}_{2\times 2} & 0 & \vdots \\ \vdots & 0 & \ddots & 0 \\ 0 & \cdots & 0 & \mathbf{Q}_{M_{\max}\times M_{\max}} \end{pmatrix}. \tag{3.39}$$

These two matrices are multiplied after each ideal segment, which modifies the complete transmission matrix to:

$$\mathbf{T}_{LN}(z,\omega) = \prod_{n=1}^{N} \mathbf{M}\left(z = L_{seg},\omega\right)\cdot\mathbf{K}_n\cdot\mathbf{R}_{U,n}\cdot\mathbf{R}_{D,n}. \tag{3.40}$$

It is important to mention here, that the segment length $L_{seg}$ is modified slightly from segment to segment to avoid the exact phase state for each mode. This subsection finalizes the description of the MMF modeling and it is possible to proceed to the numerical evaluation of the two models.

To compare these two transmission models with each other, it is important to evaluate the impact of mode coupling on the transmission characteristics of the system. Some of the system characteristics include the evolution of the DGD spread, the mode dependent loss (MDL) and overall induced coupling loss. To evaluate the evolution of the DGD in the presence of mode coupling, the eigenvalues of the group delay operator are used as proposed in [43,51]. By doing so a DGD value can be attributed to one particular principal mode and the overall DGD spread can be tracked. To do so, the group delay operator (GDO) needs to be introduced. Here the operator will be derived and used without using the PMs for MDM operation. An intuitive explanation to the principal modes and a motivation of why to use them in mode division multiplex applications was already given in the introduction and will be dealt with in more detail in section 4.

## 3.6 The group delay operator

The analysis is started by normalizing Eq. (3.30) with respect to the fundamental mode as:

$$\vec{\mathbf{b}}(z=L,\omega)=e^{-j\phi_{0,1}(\omega)}\mathbf{T}(z=L,\omega)\cdot\vec{\mathbf{a}}(z=0). \tag{3.41}$$

Here $\phi_{0,1}$ is the phase of the fundamental mode given as $\phi_{0,1}(\omega)=\beta_{0,1}(\omega)L \approx(\beta_{0,1}+\tau_{0,1}\omega)L$, where $L$ is the length of the complete MMF. Since only the frequency dependence will be of interest in this derivation, the z – dependence is omitted for now. $\mathbf{T}(\omega)$ is the transmission matrix given either by the model in Eq. (3.29) or Eq. (3.40). The derivative with respect to angular frequency $\omega$ yields:

$$\frac{\partial\vec{\mathbf{b}}(\omega)}{\partial\omega}=\left[-j\mathbf{T}(\omega)\frac{\partial\phi_{0,1}(\omega)}{\partial\omega}+\frac{\partial\mathbf{T}(\omega)}{\partial\omega}\right]e^{-j\phi_{0,1}(\omega)}\vec{\mathbf{a}}, \tag{3.42}$$

Since the input field $\vec{\mathbf{a}}$ is fixed, the derivative of $\vec{\mathbf{a}}$ with respect to $\omega$ has been set to zero $\partial\vec{\mathbf{a}}/\partial\omega=0$ in Eq. (3.42). By rearranging Eq. (3.42) and using Eq. (3.41) the following expression is obtained:

$$\frac{\partial\vec{\mathbf{b}}(\omega)}{\partial\omega}=\left[-j\mathbf{T}(\omega)\frac{\partial\phi_{0,1}(\omega)}{\partial\omega}+\frac{\partial\mathbf{T}(\omega)}{\partial\omega}\right]\mathbf{T}^{-1}(\omega)\vec{\mathbf{b}}, \tag{3.43}$$

This equation can be reformulated as:

$$\frac{\partial\vec{\mathbf{b}}(\omega)}{\partial\omega}=\left[-j\tau_{0,1}L\cdot\mathbf{I}+\mathbf{G}(\omega)\right]\vec{\mathbf{b}}(\omega), \tag{3.44}$$

where $\mathbf{I}$ is identity matrix and $\mathbf{G}(\omega)$ is the group delay operator defined as [52]:

$$\mathbf{G}(\omega)=\frac{\partial\mathbf{T}(\omega)}{\partial\omega}\mathbf{T}(\omega)^{-1}. \tag{3.45}$$

The frequency derivative of $\phi_{0,1}$ can be identified as $\tau_{0,1}L$, the group delay of the fundamental mode over the complete transmission length $L$. Equation (3.44) represents the change of the output field pattern $\vec{\mathbf{b}}(\omega)$ as the frequency changes to the first order due to the matrix $\mathbf{G}(\omega)$. Nevertheless, it is possible to find a vector $\vec{\mathbf{b}}_p$ that is frequency independent to the first order if the

frequency dependent matrix $\mathbf{G}(\omega)$ acting on $\vec{\mathbf{b}}(\omega)$ complies with the following equation:

$$\mathbf{G}(\omega)\cdot\vec{\mathbf{b}}_p = \gamma_p\vec{\mathbf{b}}_p. \tag{3.46}$$

This can be rewritten as an eigenvalue equation as follows:

$$\mathbf{G}(\omega) - \gamma_p\mathbf{I} = 0, \tag{3.47}$$

Where $\gamma_p$ are the complex eigenvalues of the matrix $\mathbf{G}(\omega)$. The eigenvectors computed through Eq. (3.47) are the PMs at the output of the MMF and are designated as $\vec{\mathbf{b}}_p$. Using Eq. (3.44) and Eq. (3.46) the following expression is obtained:

$$\frac{\partial\vec{\mathbf{b}}_p}{\partial\omega} = \left(-j\left(\tau_{0,1}+\tau_p\right)L - \alpha_p L\right)\vec{\mathbf{b}}_p, \tag{3.48}$$

where the eigenvalues have been separated into a real and imaginary part as $\gamma_p = -\left(\alpha_p + j\tau_p\right)L$. Equation (3.48) shows that $\vec{\mathbf{b}}_p$ is frequency independent since $\tau_p$ and $\alpha_p$ are scalar values. In addition, it is important to notice that the PMs do not satisfy the orthogonality condition given in Eq.(3.8) and Eq.(3.10), since losses are included in the transmission matrix $\mathbf{T}(\omega)$. This agrees with the analysis made in [53] for the PSP, where polarization dependent loss causes the PSP not to be orthogonal. The imaginary part of $\gamma_p$ can be interpreted as the differential group delay of the PM times the transmission length $L$. The real part of $\gamma_p$ can be related to the differential loss over the transmission length $L$ for each PM. The PMs at the input can be computed either by using Eq. (3.41) or by following a similar approach as described from Eq. (3.42) to Eq. (3.48). This results in the following equation:

$$\frac{\partial\vec{\mathbf{a}}}{\partial\omega} = \left[j\frac{\partial\phi_0(\omega)}{\partial\omega}\cdot\mathbf{I} - \mathbf{F}(\omega)\right]\vec{\mathbf{a}} = 0, \tag{3.49}$$

where the matrix $\mathbf{F}(\omega)$ is given as: $\mathbf{F}(\omega) = \mathbf{T}(\omega)^{-1}\,\partial\mathbf{T}(\omega)/\partial\omega$. The eigenvalue equation is then given as:

$$\mathbf{F}(\omega) - \gamma_p\mathbf{I} = 0, \tag{3.50}$$

which yields identical eigenvalues as in Eq. (3.47). The eigenvectors obtained through the eigenvalue equation (3.50) are the PMs at the input of the MMF

and are designated here as $\vec{\mathbf{a}}_p$. The matrix $\mathbf{F}(\omega)$ and $\mathbf{G}(\omega)$ are not identical which is a direct consequence of $\mathbf{T}(\omega)$ not being unitary [52], although they have the same eigenvalues. For this reason the PMs at the input are not the same as the PMs at the output and this analysis differs at this point from the analysis presented in [20]. Having now derived the GDO it is possible to proceed to study the evolution of the group delay in presence of modal coupling and to compare the two proposed models, which is the topic of the next subsection.

## 3.7 Model validation

One of the main influences of mode coupling is the reduction of the overall DGD, which in turn increases the MMF bandwidth [40,41,42]. This process can be viewed in power coupling models as a redistribution of power, where power couples from mode to mode. If a signal pulse is travelling on different modes at different times, portions of its energy will be transferred from mode to mode randomly along the transmission. By evaluating the MMF as a complete system an overall change in the group delay of the individual PMs can be observed. This was firstly shown by [43]. While the analysis in [43] is somewhat similar to the one proposed here, it fails to describe coupling losses. For this reason, all results will be plotted as a function of coupling loss.

The analysis to be presented in the next paragraph is realized for to a ten mode FMF and has therefore 4 mode groups, i.e. $M_{\max} = 4$. Polarization effects and profile dispersion are not considered here. The simulation parameters are given in Table II.

TABLE II. SIMULATION PARAMETER FOR TEN MODE FIBER (PER POLARIZATION)

| Parameter | Value | Quantity |
|---|---|---|
| $\xi$ | 5.5 μm | Radius at which the optical power of the fundamental mode has decreased to 1/e of its maximum value |
| $\Delta\tau_{\max}$ | 32 ps/km | Maximal DGD difference of the uncoupled LP-modes |
| $2\rho_0$ | 32.5 μm | MMF core diameter |
| $N_1$ | 1.475 | Group refractive index in the core axis |
| $n_1$ | 1.457 | Refractive index in the core axis |
| $L$ | 1 km | Fiber length |
| $\lambda_0$ | 1.55 μm | Center wavelength |
| $M_{\max}$ | 4 | Maximal DMG number |

First the evolution of the DGD of the PMs is analyzed and plotted as a function of the overall coupling losses. Overall coupling losses are calculated by using an overfilled launch at the input of the FMF and by evaluating the logarithmic ratio of output to input power as:

$$\alpha\left[\mathrm{dB}\right] = \left\langle 10\log\left(\frac{\vec{\mathbf{b}}^{\dagger}\vec{\mathbf{b}}}{\vec{\mathbf{a}}^{\dagger}\vec{\mathbf{a}}}\right)\right\rangle \tag{3.51}$$

Here the input vector $\vec{\mathbf{a}} = [1,1,\ldots,1]^T$, excites all guided modes in order to meet the overfilled launch condition and † represents the conjugate transpose of the given vector. The symbol $\langle\ \rangle$ indicates the ensemble average and is applied over 100 realizations. For the ideal mode approach this means that 100 realizations were computed for a fixed standard deviation $\sigma_{1/R}$ of the inverse bending radius, which follows a truncated normal distribution $\mathbb{N}\left(0,\sigma_{1/R}^2\right)$. For the ideal mode case this means that 100 realizations were computed for a fixed standard deviation $\sigma_{spl}$ of the lateral mismatch, which follows a truncated normal distribution $\mathbb{N}\left(0,\sigma_{1/R}^2\right)$. Fig. 19 (a) shows the DGD over 1 km, using the ideal mode approach as previously published in [54,55].

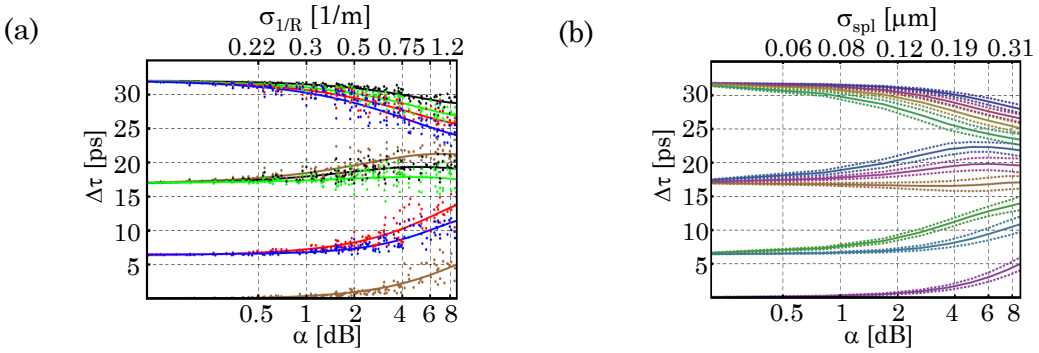


Fig. 19. (a) Evolution of the DGD of the PMs. Here the micro-bending model using ideal mode approach was used. Micro-bending radius follows a truncated normal distribution $\mathbb{N}\left(0,\sigma_{1/R}^2\right)$ with the given standard deviation of the inverse bending radius (upper frame axis). (b) DGD of the PMs using local modes. Here $10^4$ segments were used. The splice offset follows a truncated Gaussian distribution $\mathbb{N}\left(0,\sigma_{spl}^2\right)$ (upper frame axis) have been used. Each curve shows the average DGD (solid line) and the standard deviation (dotted) over 100 realizations. The truncated Gaussian distribution has a maximal value of $4\times\sigma_{1/R}$ and $4\times\sigma_{spl}$ for both approaches.

The amount of segments used for this simulation is 4 x $10^4$. The segment length $L_{\text{seg}}$ was set to a maximum value of 10 cm and varied uniformly to values below that. Each point represents a FMF realization for different statistics of the inverse bending radii distribution. The solid line was obtained with a polynomial least square fit. The results match the tendency of the results presented in [43] in which the DGD spread narrows as the inverse bending radii increases. Fig. 19 (b) shows the same result using the local mode approach using 1 x $10^4$ ideal MMF segments. These results show that both models behave

very similarly as long as the coupling losses are the same. This results confirms the assumption made in section 3.1, that coupling losses can be modeled by assuming coupling into the first non-guided mode group with DMG number $M_{\max} + 1$. Additionally it shows that losses can be computed by simply using MMF segment mismatch which speeds up the numerical procedure. It is also important to notice that both models exhibit the same behavior even though the number of MMF segments is not the same. For this reason, the number of segments are reduced in the next subsection while maintaining the coupling losses constant. This is achieved by increasing splice mismatch, i.e. by increasing $\sigma_{\text{spl}}$.

### 3.7.1 Reducing the number of MMF segments

The group delay operator is now evaluated for a 1 km FMF while varying the number of MMF segments [56]. Since the two proposed mode coupling models behave identically, the analysis here is restricted to the local mode approach (lateral offset), since its evaluation is faster. This is mainly due to the reduced number of matrix multiplications. In order to compare the results, the DGD spread, defined as the standard deviation of the group delay of the PMS as:

$$\sigma_\tau = \sqrt{\frac{1}{D-1}\sum_{i=1}^{D}\left[\Delta\tau_i - \Delta\bar{\tau}\right]^2} \tag{3.52}$$

is evaluated. Here $\Delta\bar{\tau} = 1/D\sum_{i=1}^{D}\Delta\tau_i$ is the average DGD of the PMs and $\Delta\tau_i$ are the individual DGDs of the PMs. The results are presented in Fig. 20 (a). The calculated DGD spread computed for the different number of MMF segments matches perfectly for a number of segments above 100.

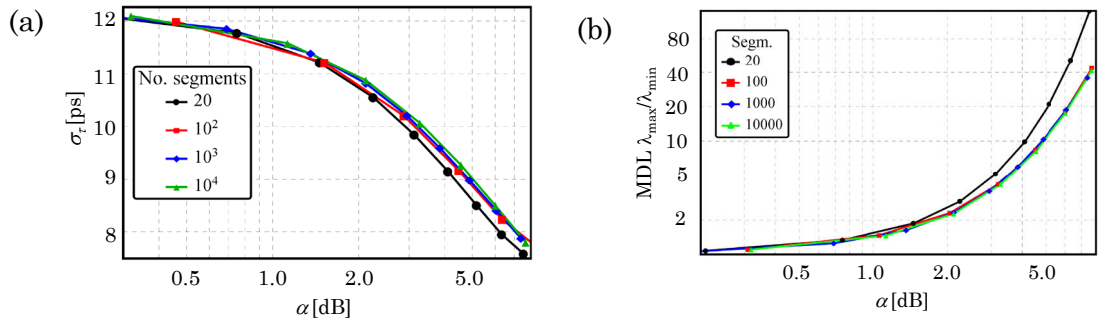


Fig. 20. (a) 10 mode FMF DGD spread $\sigma_\tau$ as function of overall coupling loss for different number of FMF segments (b) MDL values for a one km 10 mode fiber (one polarization) for different number of FMF segments.

As the number of segments is reduced below this value, a deviation can be observed at values above 1.5 dB coupling loss. This is analyzed in detail by evaluating the relative DGD spread error $\Delta\delta$, defined as:

$$\Delta\delta_i = \left(\sigma_{\tau,i} - \sigma_{\tau,ref}\right) / \sigma_{\tau,ref}. \tag{3.53}$$

Here the index $i$ represents the realization of interest, for example a MMF with 20 ideal FMF segments and *ref* stands for the reference realization which is taken here to be the FMF with $10^4$ segments. The relative DGD spread error is shown in Fig. 21.

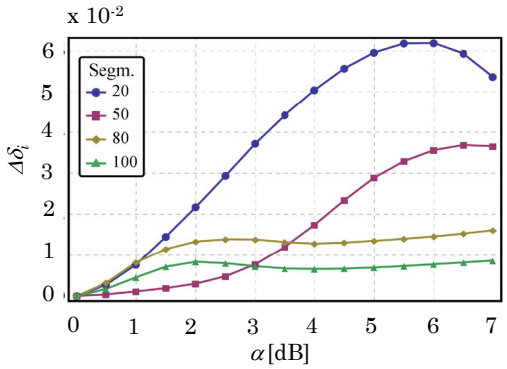


Fig. 21. Relative bandwidth error $\Delta\delta$ for 1km FMF with different number of ideal FMF segments using the local mode approach. The relative error is computed using as reference the FMF containing $10^4$ segments.

The relative error for the MMF containing 100 segments is below 1% for the complete simulated range. As the number of FMF segments is reduced, the

relative error increases, especially for higher $\alpha$ values. From these results it is possible to deduce the following results: if the FMF link contains up to 7 dB coupling loss, the number of ideal FMF segments should not be reduced below 100 within 1 km if the error is to be kept below 1%. Since high coupling losses are unlikely in FMF transmission links, the number of FMF segments can be reduced much more without making considerable errors, as shown in Fig. 21.

The power redistribution in presence of modal coupling can be studied by analyzing the behavior of mode dependent loss (MDL). MDL has a direct impact on the performance of the transmission system [57] since it can be viewed as a direct reduction of number of propagation modes [58]. For this reason it is important to analyze if the MDL behavior is preserved while reducing the number of ideal FMF segments. MDL can be calculated by decomposing the transmission matrix $\mathbf{T}_{LN}(\omega)$ using the singular value decomposition[26]. This procedure decomposes an arbitrary matrix into three matrices as [59]:

$$\mathbf{T}_{LN}(\omega) = \mathbf{U}\boldsymbol{\Sigma}\mathbf{V}^{\dagger}. \tag{3.54}$$

The matrix **U** and **V** are both unitary matrices, while **Σ** is a diagonal matrix with nonnegative entries. The diagonal entries $\lambda_i$ in **Σ** are known as the singular values. The ratio of largest to smallest singular value is known as mode dependent loss, which is defined as [60]:

$$\mathrm{MDL} = \frac{\lambda_{\max}}{\lambda_{\min}}. \tag{3.55}$$

The MDL behavior is shown in Fig. 20 (b). As in Fig. 20 (a), MDL behaves identically in the sense that all MDL values coincide if the number of segments is above 100.

Now that the limit of the model has been calculated using a ten mode fiber and its correctness verified, the DGD spread behavior is analyzed as a function of number of modes. This is the topic of the next subsection.

[26] This is an entirely numerical procedure to evaluate the power fluctuation of the MMF. It is not related to the losses of the LP-modes or PMs. A relation to this is not known so far.

## 3.8 Scaling behavior of a MMF with respect to bandwidth and MDL

Table III shows the parameters used for scaling the number of guided modes within the simulation environment. Values which are not mentioned in Table III are the same as the ones used in Table II. The parameters have been scaled such as to have a value of $\xi = 5.5\mu m$.

TABLE III. SIMULATION PARAMETERS FOR VARIOUS MMF

| Parameter | Unit | Values | | | | |
|---|---|---|---|---|---|---|
| Number of modes per polarization | | 6 | 10 | 15 | 21 | 36 |
| $\Delta\tau_{max}$ | ps/km | 17 | 32 | 51 | 75 | 123 |
| NA | - | 0.12 | 0.13 | 0.144 | 0.156 | 0.176 |
| $2\rho_0$ | μm | 30 | 32.5 | 36 | 39 | 46 |

Since the DGD spread increases due to the increasing number of modes, it is only reasonable to express the results in terms of a normalized DGD spread $\sigma_N$, which is defined as:

$$\sigma_N = \sigma_\tau / \sigma_{\tau,u}. \tag{3.56}$$

Here $\sigma_{\tau,u}$ defines the uncoupled DGD spread which is given at $\alpha = 0$, where no mode coupling is present and its value is maximal. Since the relative bandwidth gain $B_G$ is related to one over the normalized DGD spread, i.e. $B_G \propto 1/\sigma_N$, the results are presented in terms of the inverse DGD spread as function of overall coupling loss $\alpha$ for different number of guided modes. The results presented in Fig. 22(a) show that $1/\sigma_N$ depends solely on the overall coupling losses. It is important to point out that the red and blue curves (square and diamond marks respectively) show a turning point at about five and seven dB coupling losses respectively. This is a numerical artifact caused by the estimation of Eq. (3.45) since the smallest singular value of $\mathbf{T}_{LN}(z,\omega)$ is very small (due to coupling losses) and therefore the inverse $\mathbf{T}_{LN}^{-1}(z,\omega)$ cannot be computed correctly.

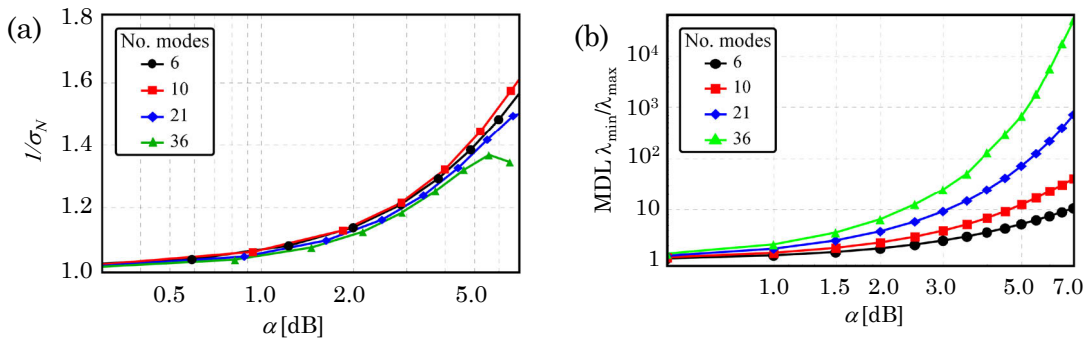


Fig. 22. (a) Inverse DGD spread for different number of guided modes per polarization (b) MDL for various MMF guiding different number of modes per polarization. The number of MMF segments used in each simulation is 100. Each curve has been estimated by averaging over 100 realizations.

The results in Fig. 22(a) show that coupling loss governs the behavior of the inverse DGD spread, which is additionally independent of the number of guided modes. This means for example that reducing the DGD spread by half comes at a cost of 9dB coupling loss (extrapolating the results in Fig. 22 (a)). This has to be considered if coupling techniques are applied to increase the bandwidth of graded index MMF. Additionally, the MDL behavior is analyzed. MDL has the tendency to increase faster with higher number of modes for the same coupling loss values as shown in Fig. 22 (b).

The main results are now summarized as follows:

- The DGD spread improvement for a MMF with parabolic index profile depends solely on the coupling loss induced by the mode coupling.
- MDL has a higher impact on MMF guiding a larger number of modes if mode coupling is used to reduce the DGD spread by the same amount. This means that a MMF with larger number of modes loses more degrees of freedom. This will directly impact the number of channels within the MMF that can be used for MDM.

This means that mode coupling can have a negative impact on MDM transmission systems, since some modes lose much power during the coupling process which directly affects the capacity of the MDM system. If mode

coupling is used intentionally in a MDM system to reduce the DGD spread as proposed by [61], some channels might be lost during transmission due to their large attenuation.

The results presented so far follow more or less the coherent analysis proposed by Poole for the case of the PSP and by Shemirani for the PMs using the GDO. Nevertheless, the coherent model proposed here should yield the same bandwidth behavior induced by modal coupling as the non-coherent approach realized in [40,41] to describe the impulse response reduction due to modal coupling. For this reason, some new parameters need to be introduced in order to compare the results presented here with the ones presented in [40,41]. These parameters will be discussed in the next subsection.

## 3.9 Comparison to power coupling models

All the results presented so far rely on the usage of the overall coupling loss $\alpha$, as defined in Eq. (3.51). This value is probably not easy to measure which is why the concept of steady state loss $\alpha_s$ is commonly used, for which different measurement techniques have been developed. A good review of the different techniques is presented in [62]. Since this is a theoretical framework, the theory of steady state loss is discussed in the next subsection.

### 3.9.1 Steady state loss

Steady-state losses are losses which can be measured if the mode distribution has reached an equilibrium mode distribution (EMD) [62]. Steady state loss is found when the loss value per unit length stays constant. To calculate this value, the method proposed by [40] is used. This method relies on solving the power flow differential equation. To understand the relation of the power flow differential equation with the model presented here, section IV of [40] will be discussed in more detail.

The partial differential equation describing power diffusion $P$ inside the MMF is given as:

$$K\left(\theta\frac{\partial^2 P}{\partial\theta^2}+\frac{\partial P}{\partial\theta}\right)-\alpha_m P=\frac{\partial P}{\partial z}+\frac{1}{v}\frac{\partial P}{\partial t}. \tag{3.57}$$

Here $\alpha_m$ represents the material loss MMF, $v$ the group velocity, which is assumed to be constant for all modes, and $\theta$ is the angle of propagation. The factor $K=\sqrt{2}n_1k_0\Delta^{2/3}F(\Omega)/r_0^3$ describes the power coupling strength as a function of the power coupling spectrum and will be discussed in more detail in annex A.2. Using the trial solution $P(z,\theta)=e^{-(\sigma+\alpha)z}G(\theta)$ and assuming steady state condition $\partial P/\partial t = 0$, Eq. (3.57) becomes [40]:

$$\theta\frac{\partial^2 G}{\partial\theta^2}+\frac{\partial G}{\partial\theta}+\frac{\sigma}{K}G=0 \tag{3.58}$$

using the normalized solution:

$$G_\nu(\theta)=\frac{1}{\sqrt{\theta_c}}\frac{J_0\left(u_\nu\sqrt{\theta/\theta_c}\right)}{J_1\left(u_\nu\right)}, \tag{3.59}$$

where $J_0$ and $J_1$ are the Bessel functions of zero and first order respectively and $\nu$ is an integer number. The parameter $u_\nu$ is determined by the roots of the Bessel function according to $J_0(\mu_\nu)=0$. The general solution to Eq. (3.59) is then given as a superposition of the trial solution as:

$$P(z,\theta)=e^{-\alpha_m z}\sum_{\nu=1}^{\infty}c_\nu G_\nu(\theta)e^{-\sigma_\nu z}. \tag{3.60}$$

The eigenvalues $\sigma_\nu = Ku_\nu^2/4\theta_c$ can be interpreted as mode dependent loss values. These values increase with increasing values of $u_\nu$ so that $\sigma_1<\sigma_2\ldots<\sigma_Y$ holds. The power distribution $P(z,\theta)$ inside the MMF has been basically expanded in terms of its eigenmodes given by Eq. (3.59). This spatial distribution $G_\nu(\theta)$ has no length dependence and the term $e^{-\sigma_\nu z}$ dictates its attenuation along the MMF[27]. As the length $z=L$ increases towards infinity, only one mode is left:

$$P(z,\theta)=c_1 e^{-(\alpha_m-\sigma_1)L}G_1(\theta). \tag{3.61}$$

This power distribution can be interpreted as the steady state power distribution since EMD has been reached and $\sigma_1$ is in that case the steady state loss value given in [1/m]. The actual steady state transmission loss is then $\sigma_1 L$. Now it is necessary to connect the coherent transmission model with the power flow equations presented in the previous paragraph. The output field vector is given in Eq. (3.41) in the frequency domain. Steady state loss requires $\partial P/\partial t=0,$ which is translated in the frequency domain to the evaluation of $\mathbf{T}_{LN}(z,\omega)$ at $\omega=\omega_0$. The output steady state power $\vec{\mathbf{b}}_{st}^{\dagger}\vec{\mathbf{b}}_{st}$ is then formulated as:

$$\vec{\mathbf{b}}_{st}^{\dagger}\vec{\mathbf{b}}_{st}=\vec{\mathbf{a}}^{\dagger}\mathbf{T}_{LN}^{\dagger}(\mathrm{z}=L,\omega=\omega_0)\mathbf{T}_{LN}(\mathrm{z}=\mathrm{L},\omega=\omega_0)\vec{\mathbf{a}}. \tag{3.62}$$

The power transmission matrix can be identified as:

$$\mathbf{P}(z=L,\omega=\omega_0)=\mathbf{T}_{LN}^{\dagger}(z=L,\omega=\omega_0)\mathbf{T}_{LN}(z=L,\omega=\omega_0) \tag{3.63}$$

[27] This attenuation value is not related to the MDL value, since the MDL values are computed using the singular value decomposition of the matrix $\mathbf{T}(z=L,\omega=\omega_0)$. The value here are computed by evaluating the eigenvalues of $\mathbf{P}(z=L,\omega=\omega_0)$.

and describes the power propagation inside the MMF in the basis of the eigenmodes given in Eq. (2.30). By expanding $\mathbf{P}(z=L,\omega=\omega_0)$ in terms of its eigenvectors, an expression comparable to the expression in Eq. (3.60) can be obtained. The eigenvector with the lowest eigenvalue can be identified as the EMD vector if steady state is reached and its eigenvalue can be related to steady state loss as:

$$\sigma_1 = \left\langle \log(\eta_1)/L \right\rangle. \tag{3.64}$$

Here $\eta_1$ is assumed to be the smallest eigenvalue[28] and needs to be applied here to several realizations due to the interference of the modes. To verify that the transmission link has reached steady state loss, the ratio between first and second eigenvalue is evaluated as proposed by [39,40]. If the ratio $\eta_1/\eta_2$ reaches a large enough value, for example 100, it is safe to assume that EMD has been reached and steady state loss can be evaluated. This procedure will be used in the next subsection to evaluate the root mean square (RMS) reduction of the impulse response as a function of steady state loss.

### 3.9.2 RMS impulse response

The effect of mode coupling can be analyzed by evaluating the RMS width of the impulse response of the MMF. This analysis has the advantage that it is not limited by the accurate inversion of the transfer matrix $\mathbf{T}_{LN}(z,\omega)$, as the GDO analysis presented in section 3.8. The RMS width of a pulse is defined as:

$$RMS = \sqrt{\left\langle t^2 \right\rangle - \left\langle t \right\rangle^2}, \tag{3.65}$$

where the n$^{\text{th}}$ moment $\left\langle t^n \right\rangle$ of the optical power envelope $p(t)$ is given as:

$$\left\langle t^n \right\rangle = \int_{-\infty}^{\infty} t^n p(t) dt \tag{3.66}$$

A pulse containing unit energy, $\left\langle t^0 \right\rangle = 1$, is launched at the input of the MMF while exciting all guided modes with $\vec{\mathbf{a}}_n$ as defined in section 3.7. The output response is then normalized to unit energy to capture only distortion effects.

[28] The smallest eigenvalue, corresponds to the smallest steady state loss value so that the assumption so $\sigma_1 < \sigma_2 < \ldots < \sigma_Y$ holds.

Three exemplary realizations are shown in Fig. 23 (b) – (d) for a ten mode FMF (These impulse responses are not normalized to unity at the output). Fig. 23 (b) shows the uncoupled impulse response. Each peak corresponds to the sum of power carried in a DMG. The power amplitude increases due to the increasing number of modes within a DMG with larger DMG number.

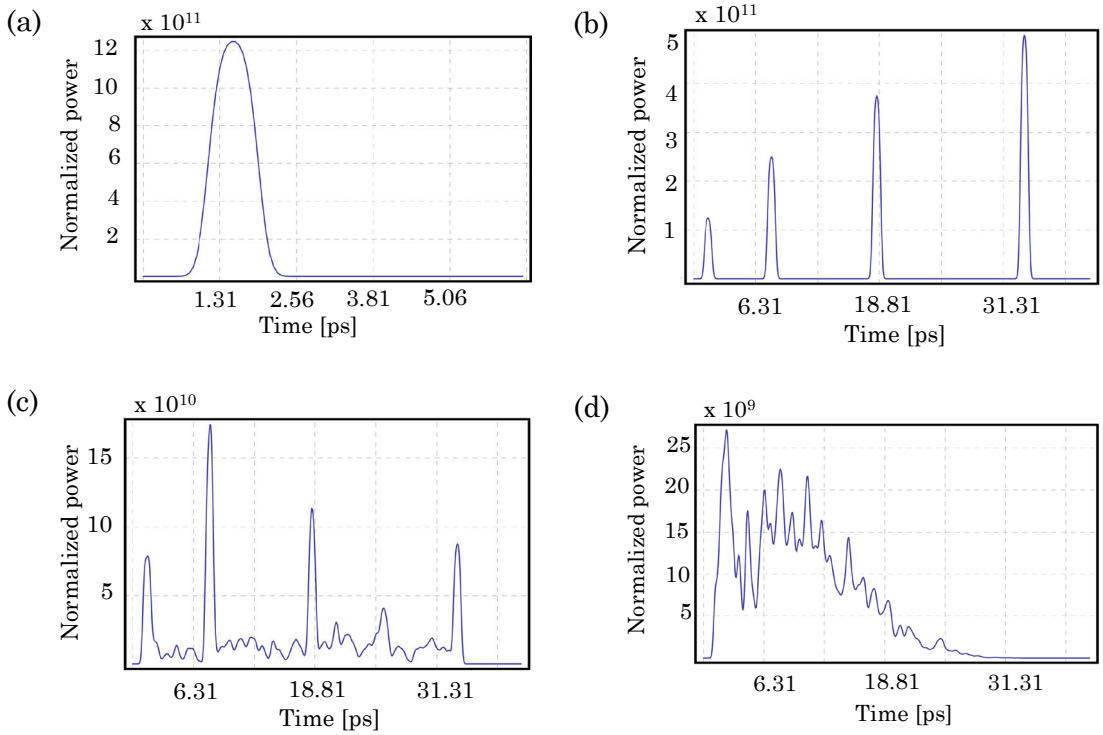


Fig. 23. (a) Input pulse with one ps width; (b) Uncoupled impulse response of ten mode FMF; (c) Impulse response of ten mode FMF with 1.6 dB coupling loss; (d) Impulse response of ten mode FMF with 8.2 dB coupling loss.

The DMG number increases for each peak from left to right of Fig. 23 (b). A sparse impulse response is shown in Fig. 23 (c), where the coupling loss corresponds to the value of 1.6 dB. Additionally, the impulse response is shown in Fig. 23 (d) where the coupling loss value is 8.2 dB. Here it is possible to see that the coupling process has effectively reduced the length of the impulse response at the price of 8.2 dB coupling loss.

The ratio $R$ between coupled to uncoupled RMS width, which is given as:

$$R = \frac{RMS}{RMS_{unc}} \tag{3.67}$$

and is calculated to capture the pulse width reduction. $R$ is therefore bounded by $0 < R \leq 1$ where the value 1 indicates no RMS width reduction.

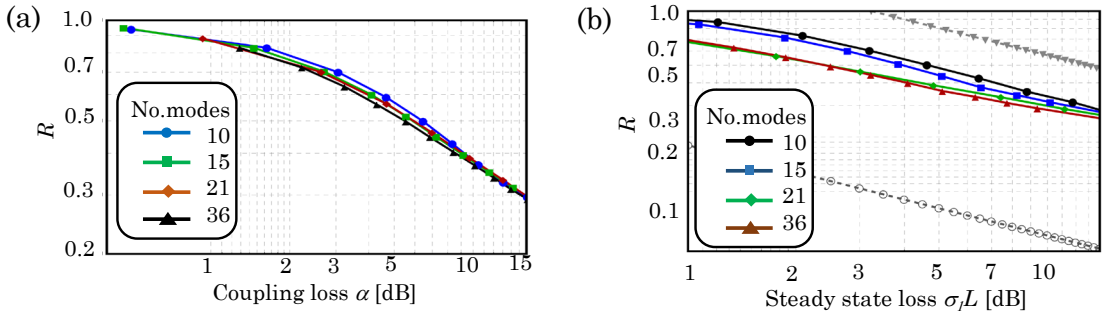


Fig. 24. (a) $R$ as function of overall loss. Results are in agreement with the results presented in Fig. 22; (b) $R$ as function of steady state loss. Dashes gray lines were computed using the values given in [40] and [41]. Solid lines were computed using the model presented here.

The solid lines in Fig. 24 (a) shows $R$ as a function of the overall coupling loss $\alpha$. These results are consistent with the results presented in Fig. 22 (a). Both the DGD spread, as well as $R$, increase very similarly for all simulated MMFs with different number of guided modes as long as $\alpha$ has the same value. Since $R$ captures amplitude and DGD spread, it can be related to a relative MMF bandwidth gain via $B_G \propto 1/R$ [29]. Fig. 24 (b) shows $R$ as a function of steady state loss $\sigma_1 L$. Solid lines are used to distinguish between the results presented in this manuscript against the results given in [41], which are plotted using gray dashed lines. The difference between the two gray dashed lines (circles and triangles) shown in Fig. 24 can be stated as follows: the lower line (gray-dashed with circle marker) represents the lower boundary, which is given using a value of $R^2\sigma_1 L = 0.18\text{dB}$ as estimated in [40] and verified in [41]. The upper boundary (grey dashed- with triangle markers) is a more realistic approximation given in [41], where a value of $R^2\sigma_1 L = 1.8\text{dB}$ was used. These approximations rely on the use of many modes to transform the coupled mode equations into a single differential equation as proposed by [39]. The solid lines shown in Fig. 24 (b) represent a more accurate solution to the problem since

[29] The relative bandwidth gain $B_G$ is computed accurately using the method presented here since it does not require the computation of the inverse matrix $\mathbf{T}_{LN}^{-1}(\omega, z)$ . It does not allow the individual DGD tracking as in section 3.8 though.

the equivalence of the coupled amplitude equations was solved. This is required, especially when analyzing FMFs, since the continuum approximation is not accurate in the limit of a few guided modes. As shown in Fig. 24(b), all curves converge to a square root behavior for high steady state loss values. This convergence is reached as the number of guided modes increases. This tendency agrees with the results presented in [40,41] in which a square root behavior is predicted for all values of $\sigma_1 L$ in the limit $D \to \infty$, where $D$ is the number of guided modes.

The previous results show that the coherent model, using discrete splices describes the MMF behavior correctly since it yields the same type of behavior estimated by [40,41]. The results presented here have been calculated using the parabolic index profile.

## 3.10 Summary

The main results of this chapter are summarized as follows:

- Mode coupling induced by micro-bends and splices can be modeled effectively by FMF lateral mismatches between ideal propagation sections.
- The number of lateral mismatches can be reduced down to $10^2$ segments per kilometer, while increasing the lateral mismatch to maintain the overall coupling loss constant. Reducing the number of segments per kilometer down to $10^2$ ensures a relative error below 1% for a coupling loss value of less than 7 dB. If the coupling loss is less than 2 dB/km, the number of segments can be reduced further down to 20 per kilometer.
- The relative bandwidth gain depends solely on the coupling strength induced by the mode coupling process. This applies for all FMF, no matter the number of guided modes.
- The spread of the impulse response of the FMF can be reduced by mode coupling and its reduction is linear in the low coupling regime, while it resembles a square root behavior in the high coupling regime.

Having analyzed the FMF model, the FMF is operated under mode division multiplexing condition. This is the topic of the next section.

# 4. FMF in MDM operation

Mode division multiplexing has attracted the attention of many researches in the last years due to the possibility of increasing the capacity relative to the SMF by the number of guided modes. This has been analyzed theoretically and shown in experiments by many authors, some of them named here [63,64,22]. The works rely on using the eigenmodes of the unperturbed FMF (the LP-modes), as described in section 2.3, as carriers. In the ideal case, where the FMF has no coupling and the multiplexing and de-multiplexing of the carrier modes is perfect, the signals modulated on each carrier mode propagate independently of each other (when considering the linear effects only). Therefore, the transmission throughput increases by the number of total guided or used modes. In the presence of modal coupling though, these channels are no longer independent of each other and require digital signal processing at the receiver to recover all transmitted data streams. It is therefore of interest to find eigenmodes of the complete MMF transmission system, which are more robust against modal coupling. Principal modes could prove to be such an eigenmode, since these modes a more robust towards distortion induced by modal dispersion and modal coupling as mentioned in the introduction of this work, together with Fig. 2. A special case of the principal modes is found in SMF, where the fundamental mode propagates in two different polarization directions. Due to optical birefringence, the modes propagate with different group velocities and due to random change in the birefringence along the propagation length, these modes couple, distorting the signal propagating along the SMF [65]. Principal states of polarization (PSP)

are eigenmodes of the GDO given in Eq. (3.45) and are therefore insensitive to polarization mode dispersion in the first order since each PSP travels with one well defined group velocity inside the SMF. This concept was first found by [66] for single mode fibers and then transferred to modes in a MMF by [20] and is illustrated in the case of a FMF supporting three guided modes as shown in Fig. 25.

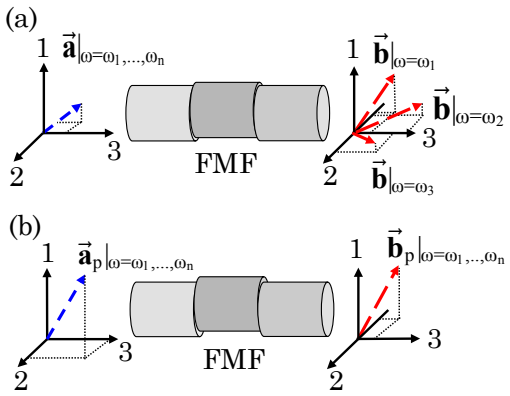


Fig. 25. Concept of principal modes in the case of a FMF supporting three spatial modes ($LP_{01}$, $LP_{11,o}$ and $LP_{11,e}$). Figure (b) shows an input vector corresponding to a PM at the input of the fiber. As the frequency changes the output vector $\vec{\mathbf{b}}_p$ stays unchanged. Figure (a) shows an example in the case where the input field pattern is not a PM. The output field distribution $\vec{\mathbf{b}}$ changes as the frequency changes.

A random mode, denoted here with $\vec{\mathbf{a}}(z=0)$ is excited as shown in Fig. 25 (a) at the input of the three mode FMF, where $z=0$ is assumed to be the FMF input. It is assumed, that this mode is a superposition of the three eigenmodes of the unperturbed FMF. Since each mode has a different group velocity $v_{gr}^{(l,q+1)}$, a pulse propagating on several eigenmodes arrives distorted at the output of the FMF. Even if only one eigenmode is selectively excited at the input of the FMF, the pulse shape is not guaranteed to be preserved because of modal coupling [52]. In the spatial-frequency domain, this can be translated to a varying output vector $\vec{\mathbf{b}}(z=L,\omega)$, which changes, as the frequency at the input changes and causes signal distortion. On the other hand, if a PM $\vec{\mathbf{a}}_p(z=0)$ is excited at the input of the FMF as shown in Fig. 25 (b), the output field pattern $\vec{\mathbf{b}}_p(z=L)$ stays constant over a small frequency range [67]. If the PMs are used as carrier modes in a MDM transmission system, they could prove to be

beneficial since they would not perceive neighboring PMs and transmit the signals undistorted. This is now analyzed in more depth by using them as carrier modes in MDM transmission systems and comparing their performance to the well-known LP- mode launch. The complete transmission system is shown in Fig. 26. The analysis here assumes that the transmitter knows the transmission channel, in this case the complete MMF link, in order to excite the PMs at the input side of the transmitter. The analysis in the next subsection is limited to a three mode FMF [30] to understand some of the limitations of this approach.

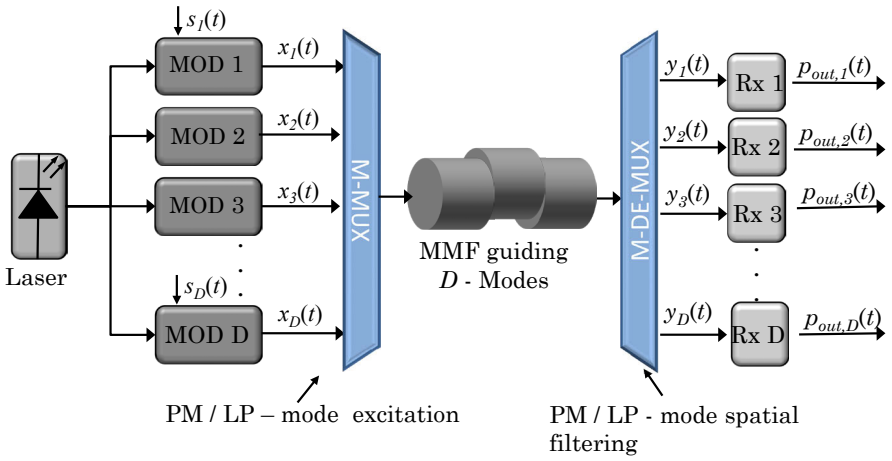


Fig. 26. Basic idea behind a FMF in mode division multiplexing operation. One laser is used as transmitter, which is split into $D$ number of modulators. Each modulator encodes different data streams $s_i(t)$ on the optical carrier, which results in a modulated optical signal $x_i(t)$. The spatial field distribution is then matched to an LP-mode or PM at the mode multiplexer (M-MUX) and transmitted though the FMF, supporting $D$ modes. At the receiver, each mode is mode-de-multiplexed (M-DE-MUX) and detected at one of the photodiodes Rx.

[30] A three mode FMF refers here to three spatial modes. Polarization is not considered in this analysis as mentioned earlier in section 3.

## 4.1 Performance evaluation in a three mode system

To understand some of the main limitations when using PMs for MDM purposes, a three-mode system is investigated numerically. Fig. 26 shows the transmission system under consideration, where the number of modes $D$ is limited to three. The transverse field distributions for the $LP_{01}$ mode is given according to Eq. (2.30) as:

$$e_{0,1}(\rho,\phi) = \frac{1}{\sqrt{\pi}\xi}\exp\left(\frac{-\rho^2}{2\xi^2}\right) \tag{4.1}$$

and both $LP_{11}$ modes as:

$$e_{1,1}(\rho,\phi) = \sqrt{\frac{2}{\pi}}\frac{\rho}{\xi}\exp\left(-\frac{\rho^2}{2\xi^2}\right)\begin{cases}\cos(\phi)\\ \sin(\phi)\end{cases}. \tag{4.2}$$

A single coherent light source, with angular carrier frequency $\omega_0$, is used as transceiver and its output power is divided equally into three different modulators, resulting in three individual signals at the same wavelength. The transverse field distribution $e_{l,q+1}(\rho,\phi)$ of each carrier is modified to match a specific principal mode or LP-mode respectively, in the optical domain by spatial filtering. The excitation of a specific modal distribution can be achieved as mentioned by [68,69] using adaptive optics, by using a holographic approach as realized in [70,71] or by using an integrated grating approach as presented in [21]. If the spatial field distribution is matched to a PM, adaptive techniques would be required due to temporal channel variations. Here the PMs are estimated once per channel realization. The modes are then multiplexed and transmitted to the output of the FMF as:

$$\vec{\mathbf{b}}(z=L,\omega) = \mathbf{T}_{LN}(z=L,\omega)\sum_{i=1}^{D} X_i(\omega)\begin{cases}\vec{\mathbf{a}}_i(z=0)\\ \vec{\mathbf{a}}_{p_i}(z=0)\end{cases}. \tag{4.3}$$

where $\vec{\mathbf{a}}_i(z=0)$ is a vector representing the i$^{th}$ LP mode and $\vec{\mathbf{a}}_{p_i}(z=0)$ is the i$^{th}$ PM at the input of the FMF. $X(\omega)$ is the Fourier transform of the optical signal:

$$x_i(t) = s_i(t)\exp(j\omega_o t), \tag{4.4}$$

where $s_i(t)$ represents the data signal modulated of the optical carrier. The output field vector is then de-multiplexed at the output of the FMF. Multiplexing and de-multiplexing can be considered as mirror images and it is therefore possible to apply the same concepts as mentioned for the multiplexing. The de-multiplexing of the i$^{th}$ LP - mode containing the i$^{th}$ output data stream $Y_i(\omega)$, now distorted by the transmission matrix $\mathbf{T}_{LN}(z,\omega)$, is achieved mathematically by applying the orthogonality condition defined in Eq.(3.8) as:

$$\vec{\mathbf{b}}^T(z=L,\omega)\vec{\mathbf{a}}_i^* = b_i(z=L,\omega) = Y_i(\omega). \tag{4.5}$$

Here the vector $\vec{\mathbf{a}}_i$ has just one non-zero component, depending on which LP-mode is to be de-multiplexed. In the case of de-multiplexing the fundamental $LP_{01}$ mode, the vector is given as: $\vec{\mathbf{a}}_1 = [1,0,0]^T$. De-multiplexing a PM is not as simple, since the PM is a weighted superposition of the three LP modes. In addition, the PMs do not satisfy the orthogonality condition given in Eq. (3.8) and Eq. (3.10). For this reason, a set of detection vectors $\vec{\mathbf{d}}_i$ will be defined in section 4.1.3, capable of detecting each PM without crosstalk at the angular carrier frequency $\omega_0$. Using these vectors, the output signal $Y_{p_i}(\omega)$ carried by the i$^{th}$ PM is given as:

$$\vec{\mathbf{b}}^T(z=L,\omega)\vec{\mathbf{d}}_i\Big|_{\omega=\omega_0} = \sum_{j=1}^{D} b_j(\omega)d_{j,i} = Y_{p_i}(\omega). \tag{4.6}$$

After de-multiplexing, the inverse Fourier transform is performed and direct detection is applied by the absolute square value to the output signal as:

$$p_i(t) = \left|\mathbb{F}^{-1}\{Y_i(\omega)\}\right|^2 = \left|y_i(t)\right|^2 \tag{4.7}$$

and

$$p_{p_i}(t) = \left|\mathbb{F}^{-1}\{Y_{p_i}(\omega)\}\right|^2 = \left|y_{p_i}(t)\right|^2. \tag{4.8}$$

The simulation parameters are given in Table IV and some values require explanation; $\alpha$ represents the average total transmission loss induced by splices and micro-bendings. This value is computed using Eq. (3.51) which requires an overfilled launch; $L$ is the FMF length and $\sigma_{spl}$ is the standard deviation of the FMF offset between adjacent FMF segments. The number of

ideal segments per km have been chosen to 20 since coupling losses are below 0.14 dB/km[31]. This would lead to a DGD spread error of less than 1% as described in section 3.7.1. The current analysis does not distinguish between splices and bends since both induced the same effect and can be viewed as generalization of the results presented in [52].

TABLE IV. SIMULATIONS PARAMETERS FOR MDM TRANSMISSION IN A THREE MODE FMF (ONE POLARIZATION)

| Parameter | Value | Quantity |
|---|---|---|
| $\xi$ | 5.5 μm | Radius at which the optical power of the fundamental mode has decreased to 1/e of its maximum value |
| $\Delta\tau_{max}$ | 6.3 ps/km | Maximal DGD |
| $2\rho_0$ | 26 μm | MMF diameter |
| $\alpha$ | 0 – 1.4 dB | Total average coupling loss of complete FMF length |
| $L$ | 10 km | Fiber length |
| $N$ | 20 / km | Number of ideal FMF segments per km |
| $B_F$ | 7.0 GHz | Bandwidth of three mode FMF for Length $L$ |
| $M_{max}$ | 2 | Maximal DMG number |
| $B_{mod}$ | 7 – 26 GHz | Modulation bandwidth |

Using these parameters the maximal transmission rate is analyzed as function of coupling loss using the PMs and LP-modes as carriers in subsection 4.1.2. Before this is analyzed, it is necessary to introduce the concept of the eye diagram which is often used to analyze the signal integrity of binary modulated signals as discussed in the next subsection.

### 4.1.1 Signal bandwidth and eye opening diagram

Digital signal transmission is advantageous in optical transmission links since it requires less signal to noise ratio [28]. Although the MDM transmission system analyzed in section 4.1.2 does not include Gaussian white noise, crosstalk to other channels can be perceived as noise and therefore the use of digital modulation schemes is justified here. Here the analysis is limited to on-off-keying (OOK) signals, which can be viewed as a special case of pulse

[31] This values has been calculated simply by diving the average overall coupling loss value $\alpha$ by the amount of segments used per km. Since the transmission length is 10 km and the maximal loss values is $\alpha = 1.4\,\mathrm{dB}$, the value of 0.14 dB/km is obtained.

amplitude modulation (PAM) described in annex A.3. The modulation bandwidth $B_{mod}$ of such a signal can be defined by the frequency $f_c = \omega_c / 2\pi$, at which the power spectral density crosses the first zero point [72]:

$$\left|S(\omega = \omega_c)\right|^2 / \left|S(\omega = 0)\right|^2 = 0. \tag{4.9}$$

Here $\left|S(\omega)\right|^2 = \left|\mathbb{F}\{s_i(t)\}\right|^2$ denotes the power spectral density. Fig. 27 shows the normalized power spectral density $\left|S(f)\right|^2 / \left|S(f = f_0)\right|^2$ as a function of frequency $f$ rather than angular frequency $\omega$. The signal bandwidth is denoted in Fig. 27 as $B_{\text{mod}} = f_c$.

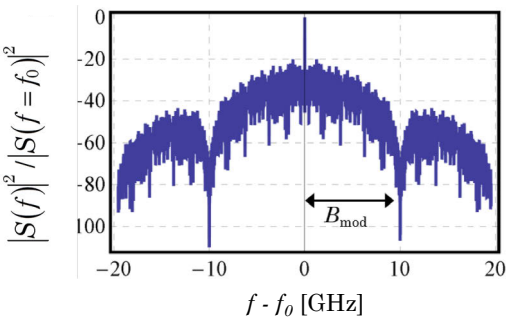


Fig. 27. Normalized power spectral density $\left|S(f)\right|^2 / \left|S(f = f_0)\right|^2$ for a 10 Gbit/s OOK signal. The pulse has been shaped using a 5th order Bessel filter with a 3dB filter bandwidth of 0.85 x Bitrate. The modulation bandwidth is given according to definition as $B_{mod}$ =10GHz.

A common tool used to analyze the signal integrity of OOK signals is the so called eye diagram. The eye diagram is constructed by partitioning a random bit sequence into many short sequences and superimposing these short sequences on each other. Fig. 28 shows the back to back (BTB) eye diagram of a random bit sequence $s(t)$ used for the MDM transmission. The bit sequence $s(t)$ has been shaped by using a 5th order Bessel filter as defined in annex A.3 with a bandwidth of $0.85 \times$ baud rate. Here two values are depicted: the eye opening (EO) and the eye width (EW). The EO is defined as the maximum opening within the bit interval:

$$\text{EO} = \min\{s(t) > d\} - \max\{s(t) < d\}, \tag{4.10}$$

where the value $d$ is the decision value and is used to define whether the signal is to be considered as zero or one. Here $s(t)$ has an amplitude of one and the

decision value is chosen at the value where the rising and falling edge intersect in the back to back eye diagram. The EW is defined as the maximal horizontal opening at a constant amplitude level and is illustrated in Fig. 28. Since the eye opening will vary as function of bitrate, the time axis will be normalized further on with respect to the back to back eye width as: $t_N = t / EW_{BTB}$. The normalization is done with respect to the input EW value and is indexed here with BTB.

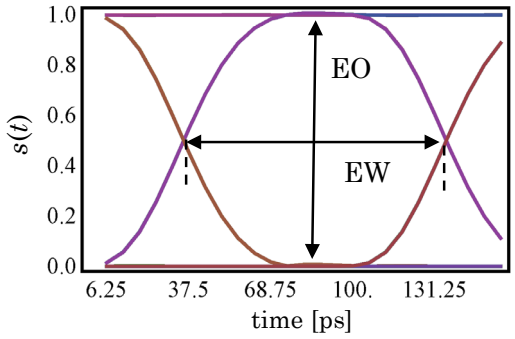


Fig. 28. Eye diagram of an arbitrary bit sequence $s(t)$ at 10 Gbit/s. The eye opening (vertical opening) and eye width (horizontal opening) are depicted to illustrate the values with EO and EW respectively. The time scale has not been normalized here.

These parameters will be used in the next subsections to analyze the transmission performance of PMs in MDM operation.

### 4.1.2 Maximal throughput using PMs in MDM operation

When the MMF is operated in the conventional incoherent way as discussed in section 1 and Fig. 1, where the source excites many of the guided modes, the transmission rate is limited by the MMF bandwidth $B_F$ [73,13]. If the modulation bandwidth $B_{\mathrm{mod}}$ of the signal $s_i(t)$, does not exceed the MMF bandwidth $B_F$, the signal does not suffer much from modal dispersion and a good transmission performance is obtained. The uncoupled bandwidth $B_F$ of a MMF is given as [5]:

$$B_F \approx \frac{0.443}{\Delta\tau_{\max} L}. \tag{4.11}$$

Since the PMs are frequency independent to the first order, it is expected that they overcome distortion effects due to modal dispersion and mode coupling up to a modulation bandwidth of $B_{\mathrm{mod}} \approx B_F$. In the case of a three mode FMF this means $B_{mod} \approx B_F = 7\mathrm{GHz}$ [32]. To formulate result independent of MMF length, transmission rate and fiber type, all the following transmission results are normalized with respect to the fiber bandwidth $B_F$ and a normalized throughput value is defined as:

$$b = \frac{B_{mod}}{B_F}. \tag{4.12}$$

To justify the use of PM transmission, the transmission quality of PMs under MDM operation is compared against the well-known LP-mode launch as presented for example in [22] but without the use of MIMO signal processing. As an example, a three mode transmission system is considered by multiplexing three random bit sequences $s_i(t)$ (one bit sequence per carrier mode) with OOK-NRZ modulation format, containing $2^{11}$ symbols. The input signal $s_i(t)$ is filtered using a fifth order Bessel filter, as described in annex A.3 with an electrical filter bandwidth of $B_{el} = 0.85 \times \mathrm{Bitrate}$. At the output of the MMF the modes are spatially filtered, detected and the optical power is computed. Additive Gaussian white noise is not included in this transmission and mode dependent losses are compensated at the output in order to study the signal distortion caused by inter-symbolic interference induced by mode coupling and mode dispersion. Mode dependent losses are compensated by multiplying the i$^{\mathrm{th}}$ de-multiplexed output signal with the value $G_i$ defined as:

$$\tilde{p}_i(t) = G_i p_i(t), \tag{4.13}$$

where $G_i$ is defined as the ratio of i$^{\mathrm{th}}$ input - to i$^{\mathrm{th}}$ output signal energy as:

$$G_i = \int_0^T p_{i,in}(t)\,dt \Big/ \int_0^T p_i(t)\,dt. \tag{4.14}$$

Here $T$ is the time length of the PRBS sequence and input and output power is given by $p_{i,\mathrm{in}}(t) = |x_i(t)|^2$ and $p_i(t) = |y_i(t)|^2$ respectively. This procedure is applied to the PMs as well and the value will be denoted as $G_{p_i}$. This ratio is

[32] The bandwidth of the FMF is $B_F \approx 7\mathrm{GHz}$ for a length of $L = 10\mathrm{km}$.

frequency independent and therefore compensates only an average mode dependent loss[33] value. Fig. 29 shows the eye diagram of two particular output signals de-multiplexed at the receiver. In (a) the de-multiplexed output signal of the $LP_{11}$ mode is shown while (b) shows the de-multiplexed output signal of the PM2. The normalized throughput value is $b = 1.14$, which corresponds to 8 Gbit/s.

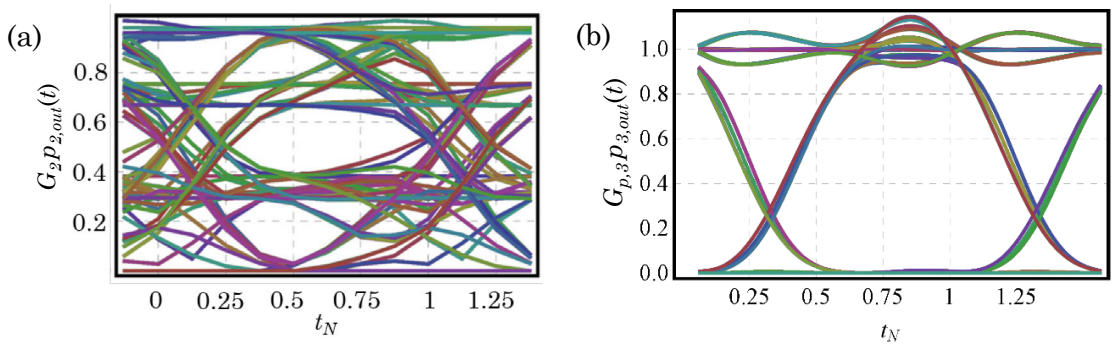


Fig. 29. Eye diagrams for the normalized output signal transmitted over a three mode FMF at 8 Gbits/s over 10 km in MDM operation. The eye diagram is evaluated as an example for the output signal de-multiplexed at the (a) $LP_{11}$ mode output and (b) PM3 output. Here 1.5 dB coupling losses are induced by mode coupling. These result resemble the ones presented in [74].

As expected, the signal modulated on the PM has significantly less distortion than the signal transmitted over the LP-mode. This is now analyzed further by evaluating the eye opening penalty (EOP) as a function of average coupling loss value. The EOP is defined as:

$$\mathrm{EOP[dB]} = 10\log\left(\frac{\mathrm{EO_{BTB}}}{\mathrm{EO}}\right), \tag{4.15}$$

$\mathrm{EO_{BTB}}$ stands for back-to-back eye opening, measured at the input of the FMF. Here it's important to emphasize again, the output signal has been normalized to contain the same energy as the input signal. Fig. 30 shows this analysis for the case where the (a) LP-modes are used as carrier modes and the (b) PMs are used as carrier modes. The normalized throughput value is fixed at $b = 1.14$ while the coupling loss value $\alpha$ is varied. Fig. 30 (a) shows the signal

[33] This mode dependent loss value is not the same values as used in section 3.8 where the ratio of maximal to minimal singular value is used. Mode dependent loss here referrers to the actual loss values for each particular mode.

multiplexed on the $LP_{01}$ mode that has a much lower eye opening penalty. This can be explained if one considers the modal distribution of the $LP_{01}$ mode, which is confined more at the core axis making it less susceptible to bents and splices. Both signals multiplexed on the $LP_{11}$ modes on the other hand exhibit a larger EOP value, which can be explained with the fact that they are more susceptible to bends and splices since their power distribution are located more at the core-axis boundary. Both exhibit a very similar trend as expected. Fig. 30 (b) shows that each signal multiplexed on a PM does practically not suffer signal distortion induced by modal dispersion and mode coupling.

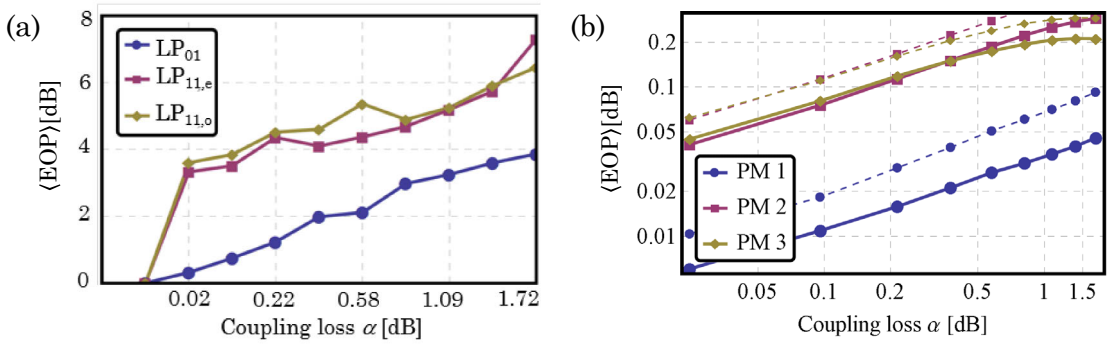


Fig. 30. EOP for a three mode FMF under MDM operation at 8 Gbit/s ($b=1.14$) as function of coupling induced loss $\alpha$ using (a) LP-modes as carriers and (b) PMs as carriers. Solid lines represent the mean EOP value, which has been obtained by averaging over ten FMF realizations. The dashed are the upper value of the mean confidence interval of 95%. The lower boundary is omitted for better overview and the confidence intervals of (a) are omitted since the mean EOP value is already very large and LP-modes will not be analyzed further.

The eye opening penalty does not exceed 0.4 decibel in Fig. 30 (b) for this particular bit rate and for the complete simulation range, which basically means that the received signal has not suffered distortion and no signal processing is required at the receiver. Nevertheless it is possible to observe an interesting behavior. Two of the three signals multiplexed on the PMs have almost identical behavior and exhibit the same performance, while the other signal exhibits a far better performance. If this is compared to the tendency shown in Fig. 30 (a) for the signals multiplexed on the LP – modes, one finds a very similar behavior; PM1 mode takes the role of the fundamental mode, while

the PM2 and PM3 take the role of the two higher order modes in the system[34]. This tendency will be studied further when increasing the number of modes in the transmission system in section 4.2.

The PM transmission analysis is now extended by analyzing the distortion behavior as function normalized throughput value $b$. The results are shown in Fig. 31 for two different scenarios: (a) $\alpha = 0.38$ dB and (b) $\alpha = 1.39$ dB. These results show that the EOP increases as the normalized throughput value increases, just as expected. It is also important to observe that the confidence interval for the EOP increases for larger normalized throughput values $b$. It can be seen that the actual EOP values depend very much on the coupling strength present in the transmission system, since larger EOP values are adopted for larger coupling loss values.

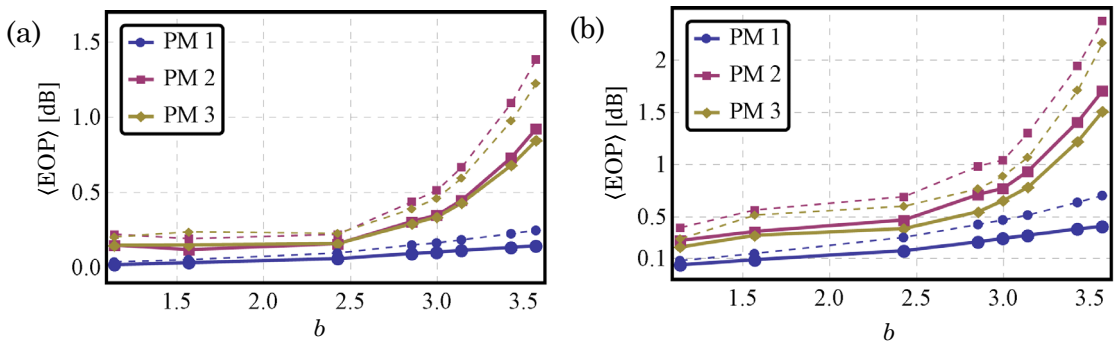


Fig. 31. EOP as function of normalized throughput $b = B_{mod} / B_F$ for two different overall coupling loss values $\alpha$: (a) $\alpha = 0.38$ dB and (b) 1.39 dB. Solid line represents mean value, evaluated over ten FMF realizations and the dashed lines represent the upper value of the mean confidence interval of 95%. The lower interval is omitted for better overview.

The performance of such a system will therefore depend largely on the combined value of $b$ and $\alpha$, which is shown in Fig. 32. Here, a contour plot is shown for the eye opening penalty as function of normalized throughput $b$ and coupling losses $\alpha$ for the signal de-multiplexed on (a) PM1 and (b) PM3[35].

[34] This does not necessary mean that the spatial distribution looks alike and that their temporal behavior is identical.
[35] PM2 is not shown since it behaves similarly to PM3 as shown in the previous results.

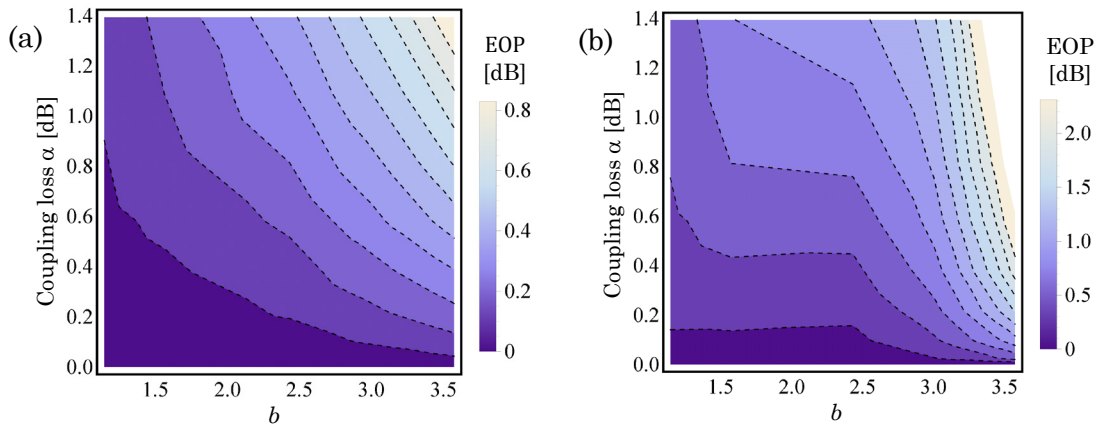


Fig. 32. EOP as function of coupling loss values $\alpha$ and normalized throughput $b = B_{mod} / B_{F3}$ for (a) PM1 and (b) PM3. These values represent the upper boundary given by the confidence interval for the mean EOP value.

Since the upper confidence interval of the mean EOP is much larger compared to its mean value, the upper boundary of the mean EOP confidence interval is used in Fig. 32. This ensures that 95% of all simulations lie underneath the EOP value specified. The results in Fig. 32 shows that PM1 has a much better performance than PM3. The eye opening is much larger over the entire simulated range which suggests that PM1 has a higher transmission bandwidth than PM2 and PM3.

To further quantify the signal quality at the output of the FMF, the normalized eye width ($EW_N$) of the signal is evaluated. The normalized eye width is shown in Fig. 28 and is defined as:

$$EW_N = \frac{EW}{EW_{BTB}}, \tag{4.16}$$

where $EW_{BTB}$ is the back to back eye width measured at the input of the MMF and the EW is the eye width at the output of the FMF, after de-multiplexing the signals. The $EW_N$ value is show as function of coupling loss values $\alpha$ for two different throughput values (a) $b = 2.4$ and (b) $b = 3.5$.

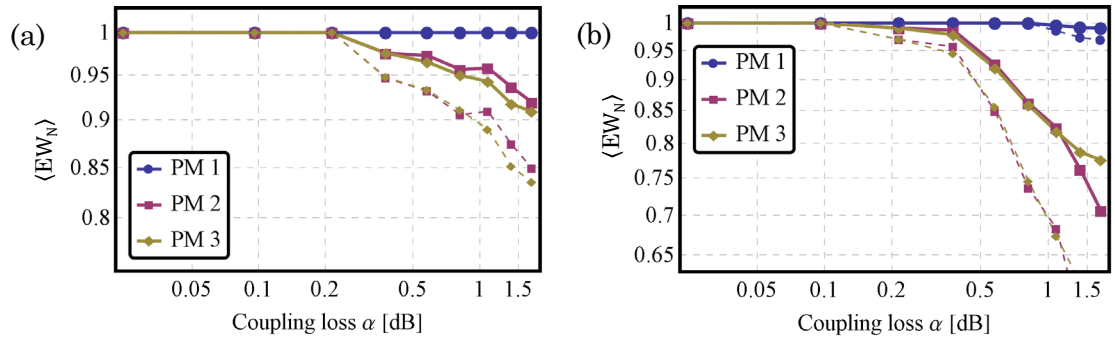


Fig. 33. Eye width as function of coupling loss values $\alpha$ for normalized throughput value of (a) $b=2.4$ and (b) $b=3.5$. The solid lines represent the mean eye width value and the dashed lines the lower value of the $5-95\%$ confidence interval. The upper value has been omitted for better overview.

Its values decrease with increasing values of $\alpha$ and $b$. In addition, it is also possible to observe that the signal multiplexed on PM2 and PM3 have similar eye width closure behavior. The $EW_N$ values decreases as function of $\alpha$ and as function of $b$. To gather the dependence over $\alpha$ and $b$, a contour plot is evaluated for the $EW_N$ value.

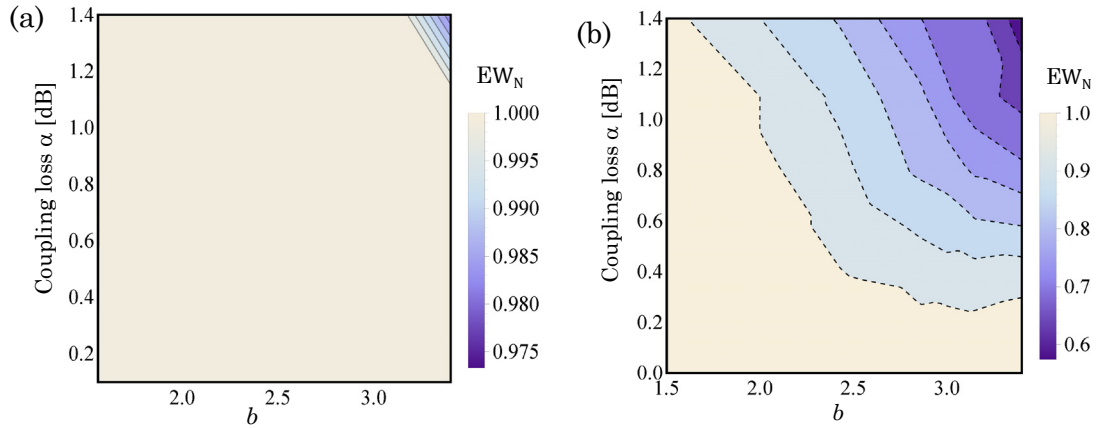


Fig. 34. Normalized eye width as function of coupling loss $\alpha$ and throughput value $b$. The results show the normalized eye width after the signal has been de-multiplexing and amplified; (a) shows the behavior for PM1 while (b) shows the behavior for PM3.

Fig. 34 (a) shows the normalized eye width $EW_N$ for PM1 while (b) shows the $EW_N$ value for PM3. It shows clearly that the signal carried by PM1 suffered less distortion than PM3 since the normalized eye width is almost unity, indicating almost no distortion. The signal transmitted through PM3 on the

other hand suffers from distortion at higher $\alpha$ and $b$ values. It is interesting to note that for signals transmitted through PM3 high normalized throughput $b$ values are possible without eye width closing only in conjunction with low coupling loss values $\alpha$ and vice versa. Since it is of interest here to operate a MDM transmission system, in which all transmission channel operate equally well, a performance criterion needs to be introduced to define weather a transmission mode is usable for transmission. Here a 1 dB eye opening penalty criterion is chosen exemplarily, combined with a minimum eye width opening of 0.78, which corresponds to an eye width penalty (EWP) of 1 dB. An example of an eye diagram of a signal that fulfils this criterion is shown in Fig. 35(a). Fig. 35 (b) shows the maximal allowable coupling loss values $\alpha$ and maximal throughput value $b$ for each PM so that the EOP and EWP criterion is fulfilled. The tendency is just as expected, PM1 has a higher performance and has therefore a higher allowable throughput value $b$. For PM2 and PM3 the maximal throughput value depends on the maximal amount of mode coupling induced loss tolerated in the transmission link. If a maximum value of $\alpha = 1.4\,\mathrm{dB}$ is acceptable, the maximal throughput value is $b = 2.7$. If only a value of $\alpha = 0.6\,\mathrm{dB}$ is tolerated, a value of $b = 3.3$ can be achieved. Since more than 1 dB coupling loss value is unlikely in a transmission system, it is possible to state that principal mode transmission in a three mode fiber seems to be very robust towards modal coupling as long as the modulation bandwidth per PM does not exceed roughly 2.5 times the FMF bandwidth[36]. This behavior is analyzed further in subsection 4.2, by scaling the number of guided modes within the FMF. For now, the analysis will continue in the frequency domain by analyzing crosstalk.

[36] This result is 2.5 times larger as the one presented in [52]. This is due to the definition of the FMF bandwidth used here in Eq.(4.11), which has an extra factor of 0.443 as proposed in [5].

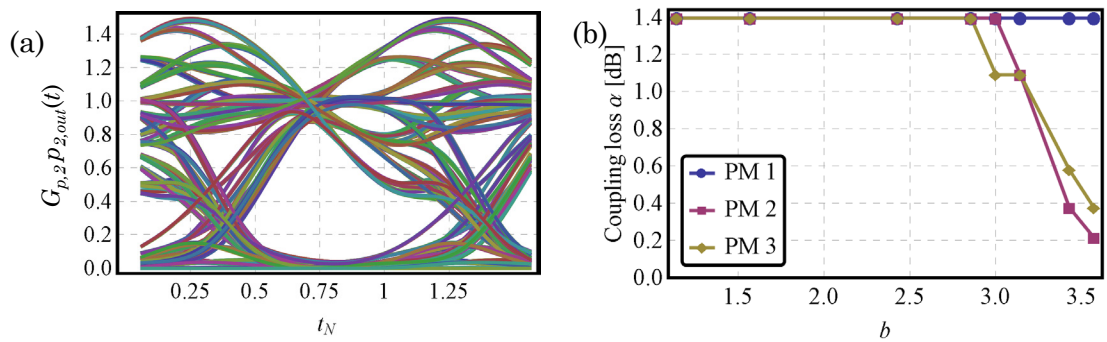


Fig. 35. (a) Example of an eye diagram that fulfills the EOP and EWP criterion; (b) maximal allowable coupling loss values $\alpha$ and maximal throughput value $b$ for each PM so that the combined criteria of EWP and EOP are fulfilled.

### 4.1.3 Crosstalk analysis and spatial filtering limitations

In order to operate the MMF in a MDM operation, it is necessary to de-multiplex each transmission mode at the receiver. For this purpose, the orthogonality condition given in Eq.(2.17) is used. As discussion in section 3.1, the orthogonality condition for the LP-modes is transformed in the vector space as:

$$\vec{\mathbf{a}}_i^T(z=0)\,\vec{\mathbf{a}}_j^*(z=0)=0. \tag{4.17}$$

where the vectors $\vec{\mathbf{a}}_i$ and $\vec{\mathbf{a}}_j$ are two vectors, representing the weighting coefficients of the LP-modes, with only one none-zero entry at the coefficient $i$ and $j$. As mentioned in section 3.6, the most important consequence of MDL is that the principal mode vectors are no longer orthogonal. This means that Eq. (3.8) and Eq.(3.10) in section 3.1 does not apply since their scalar product does not yield zero. In other words:

$$\vec{\mathbf{b}}_{p,i}^T(z=L,\omega)\Big|_{\omega=\omega_0}\vec{\mathbf{b}}_{p,j}^*(z=L,\omega)\Big|_{\omega=\omega_0}=k_1 \tag{4.18}$$

and

$$\vec{\mathbf{b}}_{p,i}^T(z=L,\omega)\Big|_{\omega=\omega_0}\vec{\mathbf{b}}_{p,j}(z=L,\omega)\Big|_{\omega=\omega_0}=k_2, \tag{4.19}$$

where $k_1$ and $k_2$ are constant values and the index $i$ and $j$ are the indices of two different principal modes. To avoid this, it is possible to construct a set of

vectors $\vec{\mathbf{d}}_j$ that obey the following conditions at the angular carrier frequency $\omega_0$:

$$\vec{\mathbf{b}}_{p,i}^{T}\left(z=L,\omega\right)\Big|_{\omega=\omega_0}\vec{\mathbf{d}}_j\Big|_{\omega=\omega_0}=0 \tag{4.20}$$

and

$$\vec{\mathbf{b}}_{p,i}^{T}\left(z=L,\omega\right)\Big|_{\omega=\omega_0}\vec{\mathbf{d}}_i\Big|_{\omega=\omega_0}=1. \tag{4.21}$$

This can be formulated in matrix notation as [52,74]:

$$\mathbf{P}\left(z=L,\omega\right)\Big|_{\omega=\omega_0}\cdot\mathbf{D}\Big|_{\omega=\omega_0}=\mathbf{I} \tag{4.22}$$

Here $\mathbf{P}$ is the matrix containing in its rows the principal modes at the output $\vec{\mathbf{b}}_p$, $\mathbf{I}$ is the identity matrix and $\mathbf{D}$ is the detection matrix in which each column represents one detection vector $\vec{\mathbf{d}}_i$ used to detect the i$^{\text{th}}$ PM. Computing the detection vectors translates in inverting the PM matrix $\mathbf{P}$ as:

$$\mathbf{D}\Big|_{\omega=\omega_0}=\mathbf{P}^{-1}\left(z=L,\omega\right)\Big|_{\omega=\omega_0}. \tag{4.23}$$

To study the impact on an MDM transmission system, a frequency domain analysis in which crosstalk is computed as a function of the frequency deviation $f-f_0$ is carried out. Crosstalk at the receiver is defined using the relation given in Eq. (4.18) as:

$$P_{j,1}^{C}\left(z=L,\omega\right)=\sum_{i=1,i\neq j}^{D=3}\left|\vec{\mathbf{b}}_{p,i}^{T}\left(z=L,\omega\right)\vec{\mathbf{b}}_{p,j}^{*}\left(z=L,\omega\right)\Big|_{\omega=\omega_0}\right|^2 \tag{4.24}$$

and using relation Eq. (4.20) as:

$$P_{j,2}^{C}\left(z=L,\omega\right)=\sum_{i=1,i\neq j}^{D=3}\left|\vec{\mathbf{b}}_{p,i}^{T}\left(z=L,\omega\right)\vec{\mathbf{d}}_{n,j}\Big|_{\omega=\omega_0}\right|^2. \tag{4.25}$$

Here the detection vector $\vec{\mathbf{d}}_{n,j}$ is normalized to unity in contrast to the definition given in Eq. (4.20). The frequency dependence in Eq. (4.24) and Eq. (4.25) has been computed by evaluating:

$$\vec{\mathbf{b}}_{p,i}^{T}\left(z=L,\omega\right)=\left[\mathbf{T}_{LN}\left(z=L,\omega\right)\vec{\mathbf{a}}_{p,i}\left(z=0\right)\right]^{T}. \tag{4.26}$$

Fig. 36 shows the results of the simulation for the frequency domain analysis.

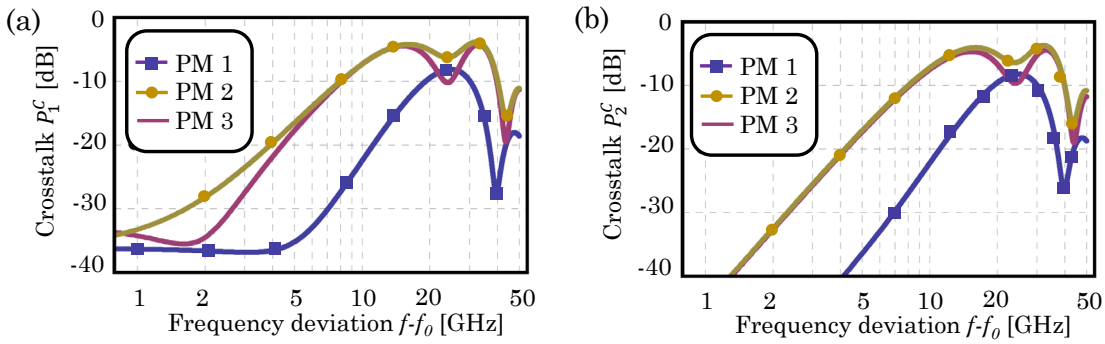


Fig. 36. Crosstalk of PMs in a three mode FMF using (a) the relation given in Eq. (4.25) and (b) using the equation given in Eq. (4.24) . The 10 km long FMF contains $\alpha = 0.6\text{dB}$ coupling loss and has bandwidth of $B_{F3} = 7\text{GHz}$

Comparing Fig. 36 (a) and (b) shows the effect of using the detection vectors. While (b) has some residual crosstalk around the carrier frequency, the use of detection vectors in (a) eliminates this completely. It is important to notice the curves in Fig. 36 (a) and (b) are very different for values below $f - f_0 < 5\,\text{GHz}$. Above this values the curves are very similar but not identical, which explains the difference in the curves shown in section 4.1.1, where EOP values behaved slightly different from each other for. As the frequency deviation increases, crosstalk increases by about 10 dB per 2 GHz and then fluctuates around 10 dB. The maximal crosstalk value depends on the mode coupling strength which grows as the total loss increases, as shown in Fig. 37. It is also important to notice that each PM has a different crosstalk value. Comparing for instance PM1 and PM3 in Fig. 36 (b) at $f - f_0 = 15\,\text{GHz}$ shows a crosstalk difference of 15 dB. This leads to the conclusion that each PM has a different crosstalk value, which correlates with the results presented in Fig. 30. This could have a great impact when using a MMF guiding a larger number of principal modes in MDM operation, since the number of modes at the output leads to increased crosstalk.

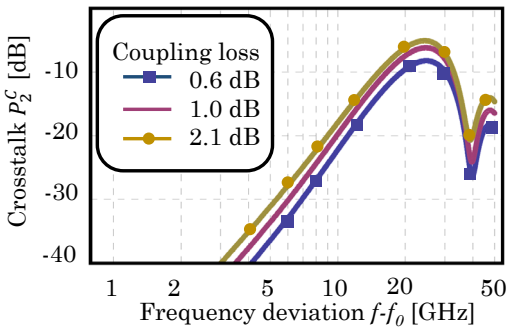


Fig. 37. Crosstalk for PM1 using detection vector for different coupling loss values $\alpha$.

Using Eq. (4.24) to de-multiplex the PMs at the receiver leads to additional crosstalk around the carrier frequency $f_0$ as shown in Fig. 36 (b) if not compensated by using the detection vectors $\vec{\mathbf{d}}_i$. Having said this, the analysis is continued by analyzing briefly the transmission degradation induced by not compensation the mode dependent loss value.

### 4.1.4 Effects of PM dependent loss

The signal analysis presented in section 4.1.2 assumes the compensation of principal mode dependent loss. This is compensated by multiplying the output signal $p_{i,out}(t)$ with the factor $G_i$, as given in Eq. (4.14). This factor compensates a time average loss value, so that only the amplitude of the signal is changed by this operation. It is therefore of interest to evaluate the effect on the EOP, defined in Eq. (4.15) without the compensation of principal mode dependent loss. The results for a fixed throughput value of $b = 1.14$ while varying the coupling loss value $\alpha$ are presented in Fig. 38.

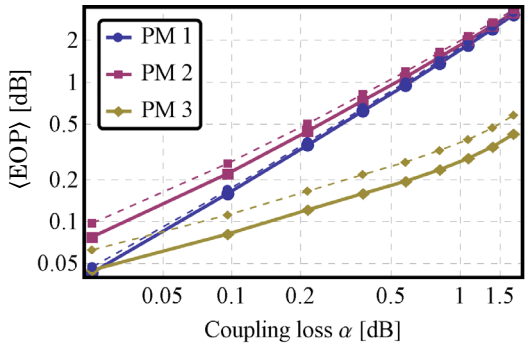


Fig. 38 EOP for a MDM transmission using PM as carriers without compensation of average principal mode dependent loss. Throughput value is fixed at $b$=1.14 while varying coupling loss value $\alpha$.

When comparing these results with the results presented in Fig. 30 (b), where principal mode dependent losses was compensated, it becomes obvious that compensation of loss is essential, to ensure good transmission performance. A difference of one order of magnitude can almost be observed among the curves presented in Fig. 38 and Fig. 30. Since the signal degradation without the compensation of PM dependent losses is so severe, further analysis using higher throughput values $b$ will not be continued since the performance degradation will increase even further.

## 4.2 Scaling properties for systems with higher number of modes

The number of modes is now varied in order to analyze the scalability of the principal modes transmission in MDM operation similarly to the results already presented in [52,75]. The simulation parameters are exactly the same ones as presented in Table III for a six-mode FMF and ten-mode FMF but are shown in Table V for better overview. Fig. 39(a) shows the maximal allowable coupling loss values $\alpha$ and maximal throughput value $b$ for each PM so that the EOP and EWP criterion of less than 1 dB is fulfilled. As expected, it is possible to observe that some PMs perform better than others.

TABLE V. SIMULATION PARAMETERS FOR SIX MODE AND TEN MODE FMF (ONE POLARIZATION)

| Parameter | Unit | Values | | |
|---|---|---|---|---|
| Number of modes | - | 3 | 6 | 10 |
| $NA$ | - | 0.11 | 0.12 | 0.13 |
| $\rho_0$ | μm | 13 | 15 | 16.25 |
| $\Delta\tau_{\max}$ | ps/km | 6.3 | 17 | 32 |
| $B_F$ | GHz | 7.0 | 2.6 | 1.38 |

The maximal throughput value $b$ that can be achieved when a maximal coupling loss value of $\alpha = 1.4\,\text{dB}$ is allowed is roughly $b = 2.3$, which is a value comparable to value given for a three mode fiber in section 4.1.2. These results can also be formulated in terms of number of usable PMs as shown in Fig. 39(b). The number of usable PMs can be understood as the total number of PMs, given the normalized throughput value $b$, that satisfy the EOP and EW penalty value of less than 1dB. Here the number of usable PMs are given as function of coupling loss $\alpha$ for a given throughput value $b$, similar to the results presented in [52]. These results are also extended to a ten mode FMF. Fig. 40 (a) shows the maximal allowable coupling loss values $\alpha$ and maximal throughput value $b$ for each PM in a ten mode FMF so that the EOP and EWP criterion is fulfilled and (b) show the number of usable PMs in a ten mode FMF.

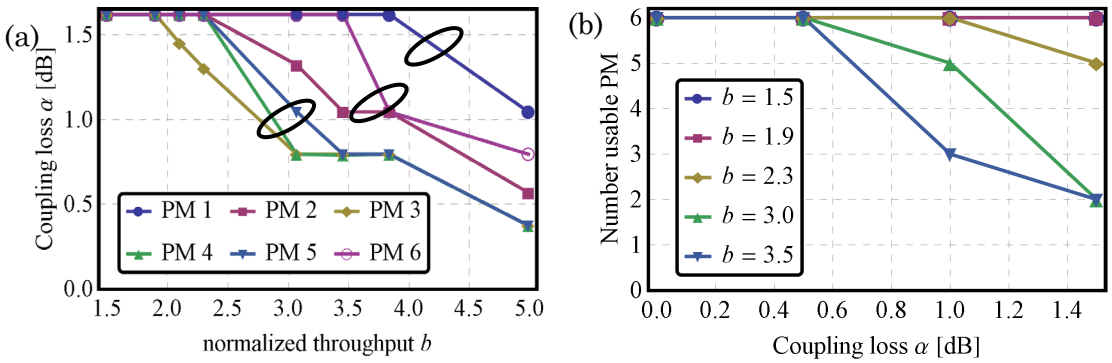


Fig. 39. (a) Maximal coupling loss value $\alpha$ and throughput value $b$ tolerated by each PM to fulfill the EOP and EW criterion in a six mode FMF; (b) number of usable PMs in a six mode FMF as function of coupling loss value $\alpha$ for different throughput values $b$.

Comparing the results for a three mode, six mode and ten mode FMF show that all PMs can be used for MDM transmission as long as the normalized throughput value does not exceed 2.3. This ensures that the signals multiplexed on each PM, do not suffer more than 1 dB eye opening penalty and 1 dB eye width penalty. In addition it is also interesting to note, that the performance of several PMs tends to be very similar, as marked in Fig. 39 (a) and Fig. 40 (a) with the black circle. This behavior could have great impact on the transmission performance of a MDM system using PMs as carriers, since exceeding the maximal throughput and coupling loss value would cause simultaneously the outage of several channels.

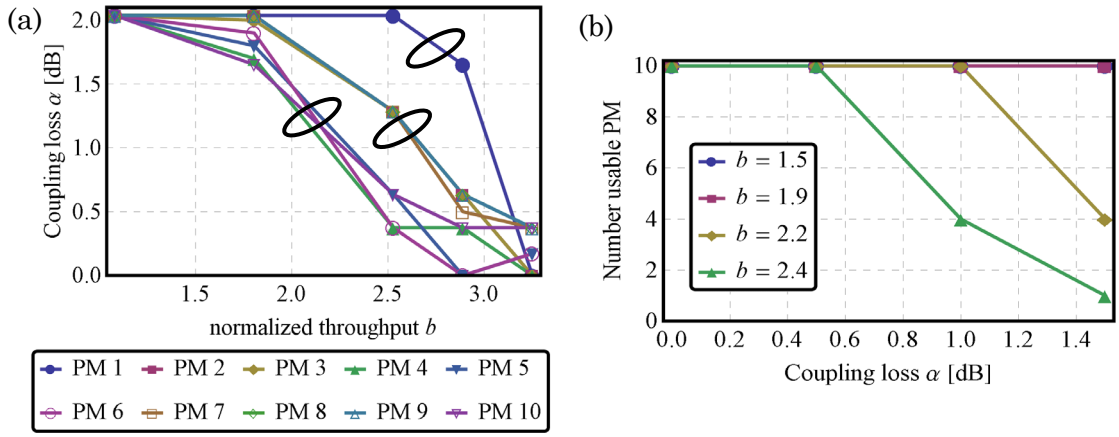


Fig. 40. (a) Maximal coupling loss value $\alpha$ and throughput value $b$ tolerated by each PM to fulfill the EOP and EW criterion in a ten mode FMF; (b) number of usable PMs in a ten mode FMF as function of coupling loss value $\alpha$ for different throughput values $b$.

These results show some of the potential limits of the MDM transmission system using PMs as carriers. Reducing the coupling strength and thereby the coupling loss value $\alpha$, seems like a possible solution to increase the maximal throughput in a mode division multiplex transmission using PMs as carriers. Nevertheless coupling loss values are extremely small so that this approach seems unpractical and an alternative approach needs to be used if the transmission rate is to be increased further. One possibility is the inclusion of MIMO digital signal processing at the receiver. Of course LP-mode launch is applicable there as well, but the question arises, if the complexity of such a receiver structure might be reduced by using the PMs as carriers. This will be the topic of the next section. For now, brief summary of the results of this chapter will be presented

## 4.3 Summary

The main results of this chapter are summarized as follows:

- The compensation of principal mode dependent loss is essential in an MDM transmission system. Should this not be taken into account, the performance is reduced significantly.
- Mode division multiplexing transmission using principal modes as carriers is beneficial without the use of MIMO digital signal processing

at the receiver, if the modulation bandwidth of each signal modulated upon each PM does not exceed roughly twice the MMF bandwidth. In this case an eye opening penalty and eye width penalty of a maximum of 1 dB can be expected for each de-multiplexed signal stream.

- The multiplexing gain obtained by a MDM transmission using PMs as carriers against the conventional MMF use is given by $G_M \approx 2 \times D$, where $D$ represents the number of guided modes. Here it is assumed that all PMs are used for transmission.

These results have a direct impact on the design of a MDM transmission system using PMs as carriers. If principal mode dependent losses are present, either induced by mode coupling or by any other device in the transmission system, it needs to be compensated by some sort of principal mode selective amplifier. This means that each PM would obtain a different amplification value. If principal mode dependent losses are not present or have been compensated, the maximal transmission rate is limited by twice the MMF bandwidth. The transmission rate of each channel needs to be fixed so that the modulation bandwidth of each channel does not exceed twice the MMF bandwidth in order to guarantee good system performance. Alternately, it is possible to consider algorithms that would adapt the transmission rate to the PM in use. In this case the transmission rate could be increased further. The MDM transmission system would also require feedback to adapt the PMs at the input of the FMF to channel variations. In this case it is important to know the time rate at which the channel varies, which could be in the order of magnitude of milliseconds, which is the time at which polarization fluctuations occur in SMF [76].

# 5. Comparison of receiver complexity

The mode division multiplexing transmission system presented in section 4 was analyzed without MIMO digital signal processing after detection. The maximal throughput achieved was mainly limited by the MMF bandwidth. As mentioned earlier, this limit could be overcome by using MIMO digital signal processing at the receiver. In that case, MDM transmission using LP-modes as carriers is feasible as presented by many authors [22,49,63,77]. Nevertheless it is still of interest to compare the performance of the LP-mode launch towards PM launch in MDM transmission in terms of receiver complexity. Here the complexity of the receiver structure will be defined by the amount of temporal filter taps necessary to equalize a signal to a certain error vector magnitude (EVM) level, defined in section 5.2. The complete transmission system resembles therefore the transmission system shown in Fig. 26, but it includes now a coherent receiver to obtain phase and amplitude information of the transmitter signal, as well as MIMO digital signal processing to equalize the output signals as shown in Fig. 41, similar to [78].

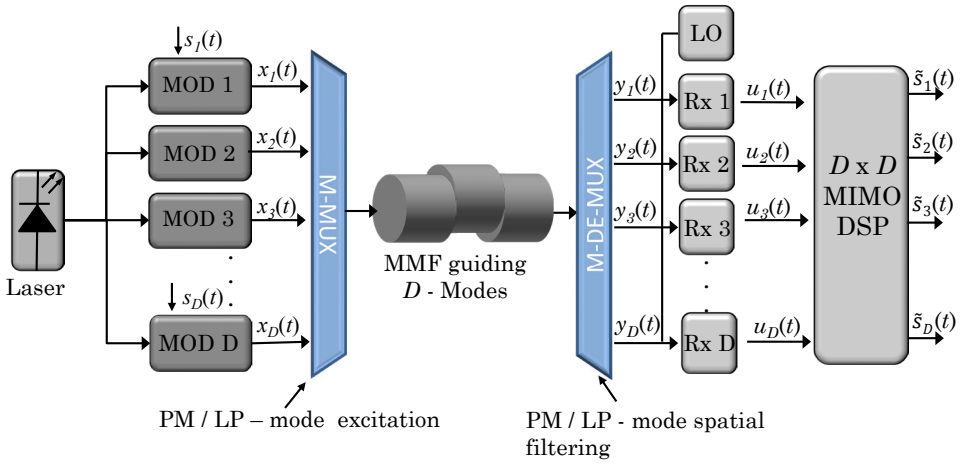


Fig. 41. MDM transmission system using MIMO digital signal processing. Optical fields at the output of each modulator (MOD) are encoded and then matched to a desired spatial mode which is either a LP-mode or a principal mode. These are then multiplexed and transmitted through the multimode fiber. At the output, the sum of all modes is mode-de-multiplexed (M-DE-MUX) and detected using a coherent receiver (RX). Each signal then passes through the MIMO Wiener filter where an estimate of the transmitted input signal $s_i(t)$ is computed.

Since the transmission scenario does not change much with respect to the FMF, the same fiber parameters are used as in section 3.8 in Table III for the six mode FMF. The use of coherent receivers enables the use of higher order modulation formats, which are discussed in annex A.3. Here the analysis is limited to quadrature phase shift keying (QPSK) signals. The coherent receiver is assumed to be ideal which means that the frequency of the local oscillator is $\omega_0$ so that no frequency compensation technique is necessary. After propagating through the MMF, the optical signal is filtered spatially and the following expression is obtained for the signals DE-multiplexed from the LP-modes:

$$y_i(t) = \mathbb{F}^{-1}\{Y_i(\omega)\} \tag{5.1}$$

and for the PMs:

$$y_{p,i}(t) = \mathbb{F}^{-1}\{Y_{p,i}(\omega)\}. \tag{5.2}$$

The following description will be limited to signals DE-multiplexed from LP-modes as given in Eq. (5.1) to simplify notation but is also applicable for PMS. The signal $y_i(t)$ can also be formulated as:

$$y_i(t) = u_i(t)\exp(j\omega_0 t). \tag{5.3}$$

The optical carrier frequency is given here with $\omega_0$ and $u_i(t)$ describes the i$^{th}$ complex envelope. To obtain the complex envelope of the optical signal $u_i(t)$, a coherent receiver is necessary which basically down mixes the optical signals $y_i(t)$ with a local oscillator laser to transform the pass band signal into a baseband signal and thus obtaining $u_i(t)$. Since the MIMO Wiener filter works with complex filter coefficients, the complex signal is processed without decomposing the signal into in-phase and quadrature component. The analog optical signal[37] $y_i(t)$ is down sampled to two samples per symbol. Since the goal here is to analyze the signal distortion due to transmission, no noise is added. In this case, the MIMO Wiener filter can practically equalize the signal $s_{i,out}(t)$ so that the square error is basically zero, i.e. $\mathbb{E}\left\{\left|e(t)\right|^2\right\} = \mathbb{E}\left\{\left|s_i(t) - \tilde{s}_i(t)\right|^2\right\} \approx 0$. Since it is of interest to compare if the receiver complexity is reduced in terms of required filter taps using the PMs as carrier modes against the LP – modes, a criterion needs to be defined, up to which point a mode is successfully equalized. A common metric used to define the quality of a complex signal is the so called error vector magnitude (EVM) which is discussed in more detail in subsection 5.2. For now the details of the MIMO Wiener filter are discussed.

[37] The analog optical signal is modeled here and transmitted here by using 16 samples per bit.

## 5.1 MIMO Wiener Filter

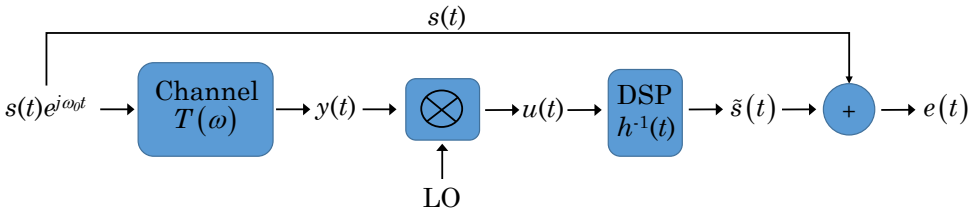


Fig. 42. Typical configuration for optimum inverse system modeling [79].

In this subsection the fundamentals of the MIMO Wiener filter will be discussed. The filter will be discussed by starting out with a simple single input single output (SISO) case and then extending it to the more complex multiple input multiple output case. The basic idea of the SISO problem is shown in Fig. 42. An arbitrary input signal $x(t) = s(t)\exp(j\omega_0 t)$ propagates for instance through a single mode fiber. The channel is described in the frequency domain by the transfer function $T(\omega)$ and the output signal $y(t)$ is given as[38]:

$$y(t) = \mathbb{F}^{-1}\{X(\omega)T(z,\omega)a\}. \tag{5.4}$$

The complex envelope $u(t)$ is recovered using a coherent detector and then sampled and it enters the equalizer, where it is convoluted with the estimated inverse channel impulse response $h(t)^{-1}$ as:

$$\tilde{s}(t) = h^{-1}(t) * u(t). \tag{5.5}$$

The signal $\tilde{s}(t)$ is an estimate of the input data signal $s(t)$. The error $e(t)$ is then computed and the optimal estimation of the input signal $\tilde{s}_{opt}(t)$ is obtained when the error is minimal. The transmission channel is assumed to be causal, containing only linear effects and it is time invariant[39]. For this reason the signal will be described using a finite impulse response (FIR) filter which will be discussed later. The analysis here will deal with the time domain representation of the Wiener filter. A Wiener filter minimizes the expectation value of the square error $|e(t)|^2$ of the signal as:

[38] Here the notation used in section 4 is used to describe a single mode fiber. The transfer matrix $\mathbf{T}_{LN}(z,\omega)$ simply becomes a transfer function $T(z,\omega)$ and the input vector $\vec{\mathbf{a}}$ is simply a scalar value a.

[39] At least for a certain time window.

$$\mathbb{E}\left\{\left|e(t)\right|^2\right\} = \mathbb{E}\left\{\left|s(t) - \tilde{s}(t - T_d)\right|^2\right\} \doteq \text{Min.} \tag{5.6}$$

Here $T_d$ is the time delay induced run time through the channel and the inverse equalizer, which will be omitted for simplicity now.

As mentioned earlier the signal needs to be resampled which is done by choosing a sampling period $T$ of at least $T < T_B / 2$ according to the Nyquist criterion, where $T_B$ is the symbol duration, in order to avoid aliasing. The sampled version of Eq. (5.6) is then given as:

$$\mathbb{E}\left\{\left|e(nT)\right|^2\right\} = \mathbb{E}\left\{\left|s(nT) - \sum_{l=0}^{L_F-1} c_l^* u(nT - lT)\right|^2\right\}. \tag{5.7}$$

Here $L_F$ is the length of FIR filter and $c_l^*$ are the complex filter coefficients. The error signal $e(nT)$ is defined as:

$$e(n) = s(n) - \sum_{l=0}^{L_F-1} c_l^* u(n - l), \tag{5.8}$$

where $c_l^* = a_l + jb_l$ and both $a_l$ and $b_l$ are real numbers. Here the simplified notation $s(n) \triangleq s(nT)$ was used and will be used further on. Since the square error $\left|e(n)\right|^2 = e(n)e^*(n)$ needs to be minimized, it is necessary to perform the derivative of Eq. (5.7) with respect to the filter coefficients $c_k$, which are the only free parameters and set the equation to zero to minimize the square error as:

$$\mathbb{E}\left\{\frac{\partial\left|e(n)\right|^2}{\partial c_k}\right\} = \mathbb{E}\left\{\frac{\partial e(n)}{\partial c_k}e^*(n) + e(n)\frac{\partial e^*(n)}{\partial c_k}\right\} = 0. \tag{5.9}$$

The differentiation with respect to a complex variable is defined as [79]:

$$\frac{\partial}{\partial c_k} = \frac{\partial}{\partial a_k} + j\frac{\partial}{\partial b_k}. \tag{5.10}$$

By applying Eq. (5.10) to Eq.(5.8), the following result is obtained for the derivative of $e(n)$ and $e^*(n)$ with respect to $c_k$:

$$\begin{aligned}\frac{\partial e(n)}{\partial c_k} &= \frac{\partial\left[s(n)-\sum_{l=0}^{L_F-1}(a_l-jb_l)u(n-l)\right]}{\partial c_k}\\ &= -2u(n-k),\\ \frac{\partial e^*(n)}{\partial c_k} &= 0.\end{aligned} \tag{5.11}$$

Inserting Eq. (5.11) into Eq. (5.9) yields[40]:

$$\mathbb{E}\{u(n-k)s^*(n)\}-\sum_{l=0}^{L_F-1}c_l\mathbb{E}\{u(n-k)u^*(n-l)\}=0. \tag{5.12}$$

The left hand side of Eq. (5.12) is the cross-correlation value between the output signal and the input signal. The right hand side describes the autocorrelation of the output signal $u(t)$ at different time differences $k-l$. Doing the same procedure for all coefficients $c_k$, where $k\in[0,L_F-1]$ yields $k$ different equations as (as an example $L_f=3$ is considered):

$$\begin{aligned}r_0 &= c_0R_{0,0}+c_1R_{0,1}+c_2R_{0,2}\\ r_1 &= c_0R_{1,0}+c_1R_{1,1}+c_2R_{1,2}\\ r_2 &= c_0R_{2,0}+c_1R_{2,1}+c_2R_{2,2}.\end{aligned} \tag{5.13}$$

Here the following notation was used:

$$\begin{aligned}r_k &= \mathbb{E}\{u(n-k)s^*(n)\},\\ R_{k,l} &= \mathbb{E}\{u(n-k)s^*(n-l)\}.\end{aligned} \tag{5.14}$$

This can be written in matrix notation as:

$$\vec{\mathbf{r}}_{us}=\mathbf{R}_{uu}\vec{\mathbf{c}}. \tag{5.15}$$

The matrix $\mathbf{R}_{uu}$ contains all components $R_{k,l}$ given by:

$$\mathbf{R}_{uu}=\begin{pmatrix}R_{0,0} & R_{0,1} & \cdots & R_{0,L_f-1}\\ R_{10} & R_{1,1} & \cdots & R_{1,L_f-1}\\ \vdots & \vdots & \ddots & \vdots\\ R_{L_f-1,0} & R_{L_f-1,1} & \cdots & R_{L_f-1,L_f-1}\end{pmatrix}. \tag{5.16}$$

The vector $\vec{\mathbf{c}}=\left[c_0,c_1,\ldots,c_{L_f-1}\right]^T$ contains all the unknown filter coefficients and the vector $\vec{\mathbf{r}}_{us}=\left[r_0,r_1,\ldots,r_{L_f-1}\right]^T$ contains the cross-correlation coefficients

[40] Here the index $l$ has been changed to the index $k$ to differentiate it to the index used in the summation. Both belong to the same space though, reaching from $\{k,l\}\in[0,L_F-1]$

between input and output signals at different time instances. This equation is known as the Wiener – Hopf equation [80]. Applying the inverse[41] of $\mathbf{R}_{uu}$ to Eq. (5.15) yields the filter coefficient vector $\vec{\mathbf{c}}$ as:

$$\mathbf{R}_{uu}^{-1}\vec{\mathbf{r}}_{us} = \vec{\mathbf{c}}. \tag{5.17}$$

The size of the matrix $\mathbf{R}_{uu}^{-1}$ which needs to be inverted is $L_F \times L_F$ and the number of filter coefficients is given by $L_F$. The resulting filter structure is depicted in Fig. 43 for a FIR filter length of $L_F = 4$. Here the signal $u(n)$ passes through the filter bank. The signal is delayed each time by $\Delta t$, and then multiplied by the filter coefficient $c_i^*$. The sum of all these parts results then in the estimated signal $\tilde{s}(n)$ which is an estimation of the input signal $s(n)$ as shown in Fig. 42. The estimation of the cross-correlation vector $\vec{\mathbf{r}}_{us}$ requires the knowledge of the input signal $s(n)$ which can be obtained for instance by training in real transmission systems.

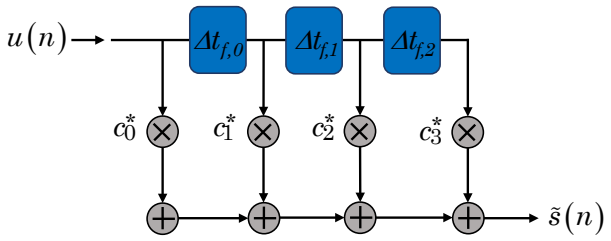


Fig. 43. FIR filter structure for signal de-convolution. Here the filter has exemplary just four filter coefficients $c_i^*$.

When implementing this, care needs to be taken, since the output signal $u(n - T_d)$ has some delay $T_d$ due to propagation compared to the input signal $s(n)$. In the single input single output (SISO) system, the delay is well defined since it is given by the time the signal requires to propagate throughout the channel. This issue is treated in the following simple example. An input signal $s(n)$ passes through a lossy, non-dispersive medium of some length $L$ and arrives at the output after some time $T_d = L/v$. The output signal $u(n)$ passes through the filter bank. At the output of the filter the square error $|e(n)|^2$ between the input signal $s(n)$ and the filtered signal $\tilde{s}(n)$ is estimated. From

[41] When inverting $\mathbf{R}_{yy}$, the QR – decomposition should be used since the matrix might be ill conditioned.

intuition, it is expected that only one filter tap is required to recover the input signal $s(n)$, since the signal $u(n)$ is just a shifted, damped version of $s(n)$.

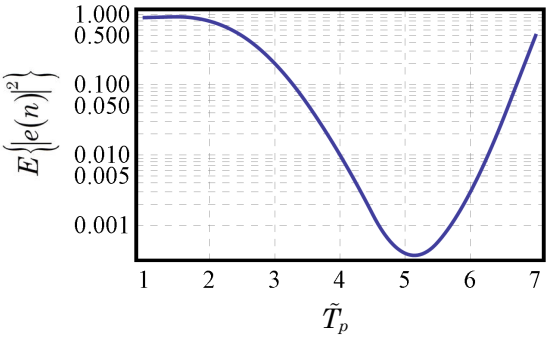


Fig. 44. The square error as function of the delay $\tilde{T}_p$ for an FIR filter with fixed filter length $L_f = 1$. The error becomes minimal when the input signal $s(n)$ is delayed at least by the time shift $\tilde{T}_p = 5$, which is the shift the output signal $u(n)$ has experienced due to propagation.

Here the delay required to estimate $r_{us} = \mathrm{E}\{u(n-k)s^*(n-\tilde{T}_d)\}$ correctly plays an important role: 1. if $\tilde{T}_d$ is too small, no correlation is found and the filter coefficients are estimated incorrect, which in return yields a much higher error, 2. $\tilde{T}_d$ is estimated to large and more than one filter tap $L_f$ is needed to minimize the square error, overestimating the required filters taps. This behavior is shown in Fig. 44. Here a FIR filter one tap $L_f = 1$ is used to show the behavior.

Having said this, the Wiener filter is now formulated for the multiple input and single output case. Equation (5.7) is extended now by modeling the signal $s_j(n)$ by a weighted superposition of all output signals $u_d(n)$ as [80]:

$$\mathrm{E}\left\{|e_j(n)|^2\right\} = \mathrm{E}\left\{\left|s_j(n) - \sum_{d=1}^{D}\sum_{l=0}^{L_F-1} c_{l,d}^* u_d(n-l)\right|^2\right\}. \tag{5.18}$$

Here the index $j$ refers to the j[th] input signal and $D$ is the total amount of output signals. Applying the same procedure as before, while taking into account that the number of taps are now extended to $D \times L_F$, yielding $D \times L_F$ equations[42], the following equation is obtained [80]:

$$\vec{\mathbf{r}}_{\mathbf{u}s_i} = \mathbf{R}_{\mathbf{uu}}\vec{\mathbf{c}}_i. \tag{5.19}$$

[42] The SISO problem before contained only $L_F$ equations.

This equations looks very similar to Eq. (5.15) but a closer looks shows that the correlation matrix is now performed between multiple output signals $u_d(n)$, described by the vector $\vec{\mathbf{u}} = [u_1, u_2, \ldots, u_D]^T$. The matrix $\mathbf{R_{uu}}$ in Eq. (5.19) can thus be viewed as a nested matrix:

$$\mathbf{R_{uu}} = \begin{pmatrix} \mathbf{R}_{u_1u_1} & \cdots & \mathbf{R}_{u_1u_D} \\ \vdots & \ddots & \vdots \\ \mathbf{R}^*_{u_Du_1} & \cdots & \mathbf{R}_{u_Du_D} \end{pmatrix}. \tag{5.20}$$

The matrices $\mathbf{R}_{u_iu_i}$ describe the autocorrelation of the output signal $u_i(n)$ with itself and their shape is identical to the matrix given in Eq. (5.16). The matrices $\mathbf{R}_{u_iu_j}$ describe the correlation between the output signals $u_i(n)$ and $u_j(n)$. The cross-correlation vector $\vec{\mathbf{r}}_{\mathbf{u},s_i} = [r_{u_1s_i}, r_{u_2s_i}, \ldots, r_{u_Ds_i}]^T$ contains the correlation values between the input signal $s_i(n)$ and all the output signals $u_i(n)$, where $j \in [1, D]$. Up to this point, the filter coefficients for one signal estimation $\tilde{s}_i(n)$ have been made. Equation (5.19) basically describes a multiple input single output (MISO) receiver structure as shown in Fig. 45 for the example of three output signals. Eq. (5.19) can be expanded to describe a multiple input multiple output receiver, by noting that it can be expanded to describe the filter coefficients for all signals by writing:

$$[\vec{\mathbf{r}}_{\mathbf{u}s_1}, \vec{\mathbf{r}}_{\mathbf{u}s_2}, \ldots, \vec{\mathbf{r}}_{\mathbf{u}s_D}] = \mathbf{R_{uu}}[\vec{\mathbf{c}}_1, \vec{\mathbf{c}}_2, \ldots \vec{\mathbf{c}}_D]. \tag{5.21}$$

Since all of these equations have the matrix $\mathbf{R_{uu}}$ in common and a vector containing vectors as elements is basically a matrix, it is possible to formulate the complete MIMO filter coefficients as [80]:

$$\mathbf{C} = \mathbf{R}^{-1}_{\mathbf{uu}}\mathbf{R_{us}}. \tag{5.22}$$

Here the filter coefficient matrix $\mathbf{C}$ is given as: $\mathbf{C} = [\vec{\mathbf{c}}_1, \vec{\mathbf{c}}_2, \ldots, \vec{\mathbf{c}}_D]$ and the matrix $\mathbf{R_{us}}$ is given as: $\mathbf{R_{us}} = [\vec{\mathbf{r}}_{\mathbf{u}s_1}, \vec{\mathbf{r}}_{\mathbf{u}s_2}, \ldots, \vec{\mathbf{r}}_{\mathbf{u}s_D}]$. Equation (5.22) fully describes the equalizer filter coefficients required to recover all input signals after propagation through a MIMO system such as for example a MMF in MDM operation.

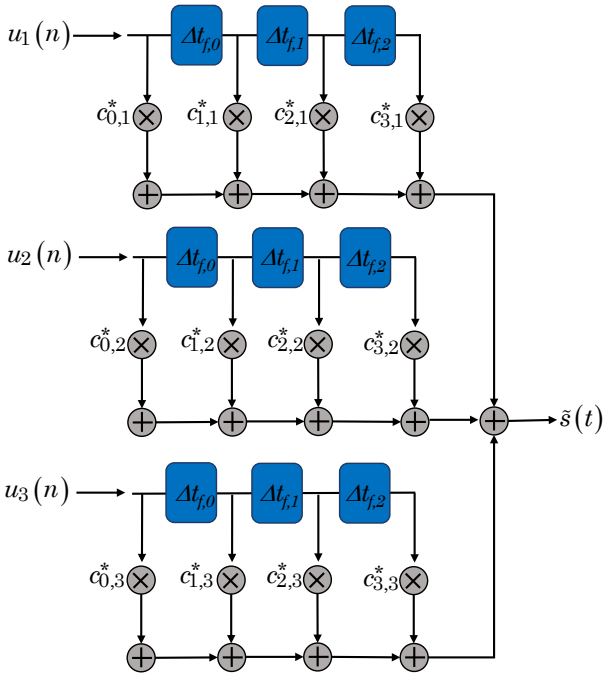


Fig. 45. MISO FIR filter structure. All output signals $y_i \; i \in [1,2,3]$ are combined and weighted to obtain the input signal estimation $\tilde{x}_1$.

It is important to mention here that the formalism proposed in [80] does not take the complex valued nature of the FIR filter coefficients into account, which will lead to a suboptimal recovery of the input signals, if these are also complex valued. Eq. (5.22) is applied in subsection 5.4 to a FMF operated in MDM operation while comparing the maximal filter length required to de-multiplex successfully the received signals $u(n)$ using the LP-mode and PMs as carrier modes. Before doing that, a new metric is introduced to quantify the quality of higher order modulation formats.

## 5.2 Error vector magnitude

The error vector magnitude measures basically the standard deviation of each constellation point, using the ideal constellation point as reference. This metric will be used to define the quality of the equalized signal $\tilde{s}_i(t)$. For completeness, the definition of the EVM values is given as [81]:

$$EVM_m = \sigma_{err}; \qquad \sigma_{err}^2 = \frac{1}{N}\sum_{n=1}^{N}\left|s_i(nT_s) - \tilde{s}_i(nT_s)\right|^2. \tag{5.23}$$

Here $T_s$ is the symbol duration and $T$ is set to $T = T_s$ [43]. The signal $s_i(nT)$ has unit amplitude and each symbol lies therefore on the unit circle as depicted in Fig. 46 (a).

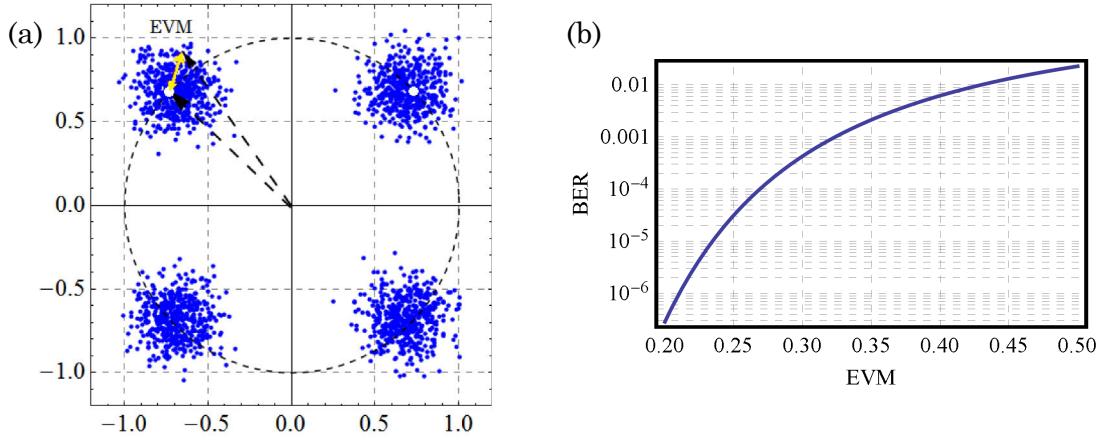


Fig. 46. (a) Example of a 4 QAM signal in which the sampled symbols are distributed around the ideal constellation points marked in white. The error vector is shown with the yellow arrow; (b) BER as function of EVM value (similar to [81]).

The EVM is plotted exemplarily in Fig. 46 (a), where the white arrow shows the error vector. Since the in-phase component and quadrature component of the signal can be viewed as independent random variables, the probability density function (PDF) is a product of the individual PDFs as:

[43] A clock recovery algorithm needs to be applied to the signal $\tilde{s}_i(nT_s)$ before it can be sampled exactly in the middle of the symbol interval to evaluate the EVM value. This can only be done after the signal has been equalized by the MIMO Wiener filter since no correlation can be found otherwise to the reference signal $s_i(nT)$.

$$f_{\tilde{s}_I\tilde{s}_Q}\left(\tilde{s}_I,\tilde{s}_Q\right)=f_{\tilde{s}_I}\left(\tilde{s}_I\right)f_{\tilde{s}_Q}\left(\tilde{s}_Q\right) \tag{5.24}$$

Here $f_{\tilde{s}_I\tilde{s}_Q}\left(\tilde{s}_I,\tilde{s}_Q\right)$ represents the joint PDF and $f_{\tilde{s}_I}\left(\tilde{s}_I\right)$ and $f_{\tilde{s}_Q}\left(\tilde{s}_Q\right)$ the PDF for the in phase and quadrature component respectively.

The relation between EVM and the symbol error ratio (SER) can be formulated by assuming that the in-phase component and quadrature components has a PDF with follows a Gaussian distribution:

$$\begin{aligned}\mathrm{SER}&=1-\frac{1}{2\pi\left(\sigma_x\sigma_y\right)}\int_0^\infty\int_0^\infty\exp\left(-\frac{\left(x-\mu_x\right)^2}{2{\sigma_x}^2}-\frac{\left(y-\mu_y\right)^2}{2\sigma_y^2}\right)dxdy,\\&=1-\frac{1}{4}\left(1+\mathrm{erfc}\left(\frac{\mu}{\sqrt{2}\sigma}\right)\right)^2.\end{aligned} \tag{5.25}$$

Here it was assumed that $\mu_x=\mu_y=\mu$ and $\sigma_x=\sigma_y=\sigma$. Since the EVM value is related to the standard deviation by $\sigma_x^2+\sigma_y^2=\mathrm{EVM}^2\Rightarrow\sqrt{2}\sigma=\mathrm{EVM}$, the bit error ratio (BER) is given as:

$$\mathrm{BER}=\frac{1}{2}\left[1-\frac{1}{4}\left(1+\mathrm{erf}\left(\frac{\mu}{\mathrm{EVM}}\right)\right)^2\right] \tag{5.26}$$

Which is consistent with the results presented in [82] and plotted in [81]. The BER as a function of EVM is plotted in Fig. 46 (b). The analysis presented here is realized without any noise so as to analyze the minimal number of filter taps required to equalize the signal $u_i\left(t\right)$ distorted by the transmission channel given some EVM value. The BER value at which it is assumed that forward error correction (FEC) is capable of recovering the distorted signal errorless, is commonly given at a value of $\mathrm{BER}\approx10^{-3}$ and corresponds to an EVM value of $\mathrm{EVM}\approx0.32$. This limit takes into account the presence of noise, which is not present in the MDM system here. For this reason, a lower value is chosen so that in the presence of noise the FEC limit is achieved. The value chosen here is $\mathrm{EVM}=0.23$, which corresponds to a BER value of $\mathrm{BER}\approx10^{-5}$.

Before presenting the simulation results, it is important to understand the parameters that influence the complexity of the MIMO digital signal processing unit in a MMF transmission system. This will be discussed in the next subsection.

## 5.3 Parameters of influence

For illustrative purposes a simple two mode transmission system as shown in Fig. 47 is considered. Here a signal is transmitted through the $LP_{01}$ mode and is ideally spatially filtered and detected by Rx 1.

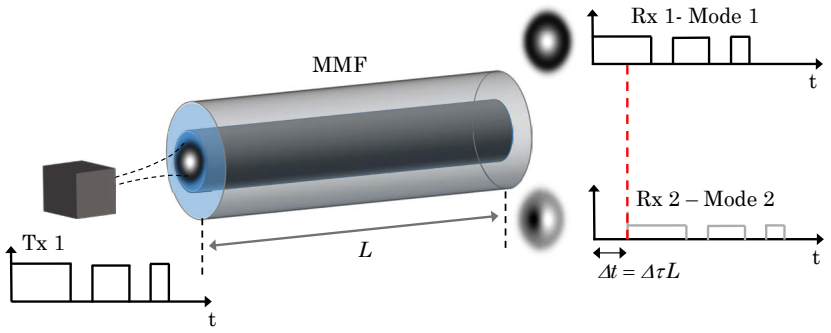


Fig. 47. Illustration of required temporal receiver length. A NRZ-PRBS signal is launched on the fundamental $LP_{01}$ mode and is spatial filtered and detected by Rx 1. Due to crosstalk at transmitter, some power couples into the transmission channel 2, which is guided by the $LP_{11}$ mode. At Rx 2, a delay copy of the original signal is obtained, with a delay $\Delta t = \Delta\tau L$

It is assumed, that there is a frequency independent crosstalk at the transmitter, so that some portion of the signal couples to the other spatial channel without distorting it, mainly the $LP_{11}$ mode. In that case a portion of the signal will arrive, just as shown in Fig. 47 at Rx 2 in grey. This version is a delayed copy of the original signal, which was supposed to be sent only through the $LP_{01}$ mode. If this crosstalk signal at Rx 2 is to be used for equalization purposes at Rx 1, the receiver needs to keep the signal at Rx 1 for a time $\Delta t$, until it can process it together with the portion of Rx 2. This would introduce one single filter tap with time delay $\Delta t$. In this simple illustration, the cause for crosstalk is at one discrete point. In the transmission system of interest though, crosstalk is induced by micro-bendings and splices. Therefore it is necessary to resolve the signal more precisely. Usually the optical signal is sampled and then processed. Therefore the smallest possible time resolution is the sampling rate, which is here twice the symbol rate $R_s$. Each filter tap has therefore a temporal length of $\Delta t_f = 1/(2R_s)$, where $R_s$ is the transmission rate. The maximal number of temporal filter taps $N_s$ in the absence of noise are therefore given as:

$$N_s = \frac{\Delta t}{\Delta t_f} = \Delta t 2 R_s \approx \frac{B_{mod}}{B_F} = b. \tag{5.27}$$

Here Eq. (4.11) was used and the definition of the modulation bandwidth given in section 4.1.1 was used. As depicted in Fig. 45, the number of filter taps increase additionally with the number of channels used. In this case, the number of channels is given by the total number of guided modes which is limited here to six. From Eq. (5.27) it becomes evident that the number of required filter taps $N_T = D \times N_s$ increases with the normalized throughput $b$. For this reason, all the following results are plotted as function of $b$. Having reviewed this, the results will be presented in the next subsection.

## 5.4 Simulation results

The simulation parameters are shown in Table VI and they are basically the same as the ones used in section 4.2 for the six mode FMF. The modulation format used in this is QPSK and the length of the PRBS sequence is $2^{11}$. Here it's worthwhile to note that the few mode fiber bandwidth given is for the length of $L = 10\text{km}$.

TABLE VI. SIMULATION PARAMETERS FOR MDM TRANSMISSION USING MIMO DIGITAL SIGNAL PROCESSING

| Parameter | Value | Unit |
|---|---|---|
| Number of modes | 6 | - |
| $NA$ | 0.12 | - |
| $\rho_0$ | 15 | μm |
| $\Delta\tau_{\max}$ | 17 | ps/km |
| $B_F$ | 2.6 | GHz |
| $L$ | 10 | km |
| $\alpha$ | 0 - 2 | dB |
| $B_{mod}$ | 5 - 31 | GHz |
| $\sigma_{spl}$ | 0 – 0.34 | μm |

The results are shown in Fig. 48 (a) though (d). These result were computed by averaging over 16 simulation realizations for a given $\sigma_{spl}$ and random phase. From the results presented in section 4.1.3 it is known that PMs have different crosstalk behavior. For this reason it is expected that some of these require more filter taps to equalize them successfully to a value of EVM = 0.23. For this reason Fig. 48 (a) – (d) contain two curves. The mode that performs best requires the minimum amount of taps (dashed curve), while the modes that perform the worst require the maximal amount of taps (solid curve) to achieve the EVM value. The rest are somewhere in between as shown by the shaded area. The results presented in (a) and (b) were carried out using an overall coupling loss of $\alpha_1 = 0.4\text{dB}$ while the results in (c) and (d) contained an overall coupling loss of $\alpha_2 = 1.3\text{dB}$. The result filled in red in Fig. 48 (b) and (d) show that PM transmission has some advantage towards the LP-mode transmission (shaded in blue), but it depends highly on the value of $b$ and the overall coupling loss value $\alpha$.

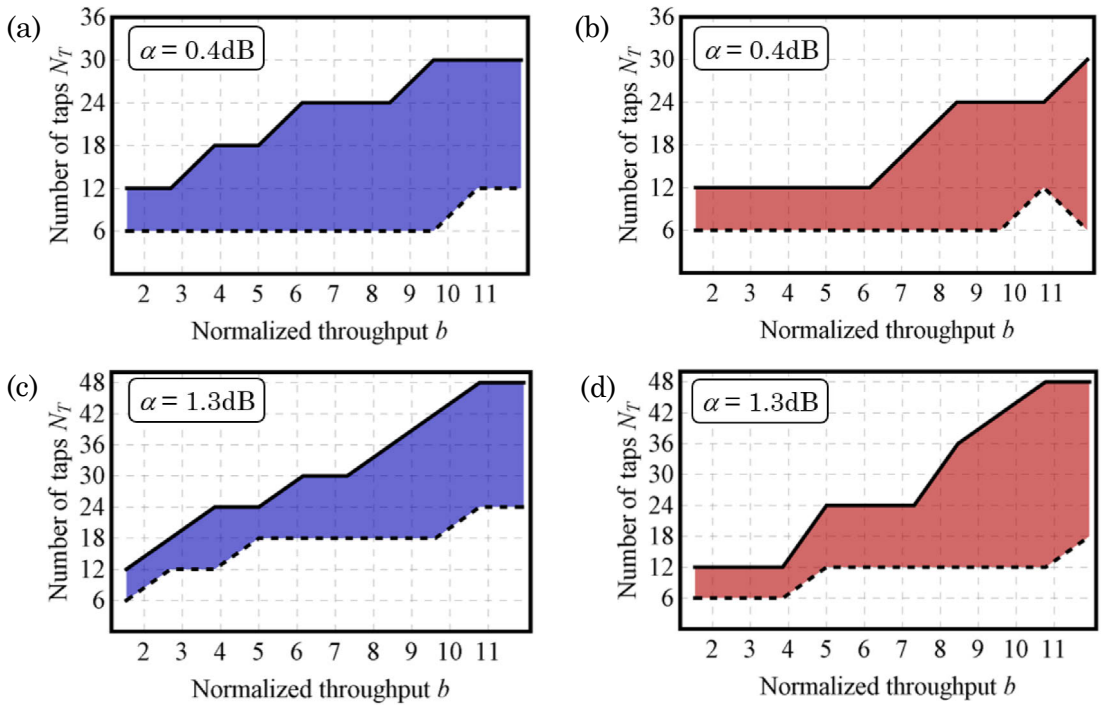


Fig. 48. Required filter taps per mode as function of normalized bandwidth $b$ ; (a) and (b) show simulation results for 0.4 dB overall coupling loss for LP – modes and PMs respectively; (c) and (d) show simulation results for 1.3 dB overall coupling loss for LP – modes and PMs respectively. Each simulation curve is calculated by averaging over 16 transmission realizations using a truncated normal distribution for $\sigma_{spl}$ .

In the case of the PMs, it is also interesting to notice the lower boundary (dashed curve) does not increase significantly as $b$ increases, leading to the conclusion that there is one (or several) PM at least that require a small number of filter coefficient to be successfully equalized, which is consistent with the results already presented in section 4.2. This points out that this particular PM does not couple much, making this one very robust toward modal coupling even for higher $b$ values.

In the case of short range transmission, most of the implementations cases such as data center transmission need to have a low complexity value since this makes them low cost. In this case it is of interest to analyze the maximal throughput one can achieve using a fixed equalizer length of two temporal taps, i.e. $N_s = 2$ and $N_T = 6N_s = 12$ . The system will be defined then as adequate if all transmission channels are successfully equalized to an EVM value below 0.23. The normalized throughput as a function of coupling loss $\alpha$ is shown in Fig. 49. Two curves are shown, the red curve with round markers

represents the results for PM transmission, while the blue curve with square markers represent the results for LP-mode transmission. These lines represent the boundary up to which the maximal throughput value $b$ can be increased as a function of coupling loss value $\alpha$, so that the receiver is still capable of equalizing all the signals down to the EVM value of 0.23. In other words, all signals that are transmitted and have values below that boundary, are successfully equalized. Comparing both curves it is possible to observe that for coupling loss values of less than 0.3 dB, there is basically no performance difference. This is to be expected since crosstalk for those values tends to zero and the signal can be equalized with good performance without requiring many taps. As the coupling increases, the performance difference between the two carriers increases. Here it is possible to observe that PM transmission has a 2.5 times higher throughput b value than LP-mode transmission using the same receiver.

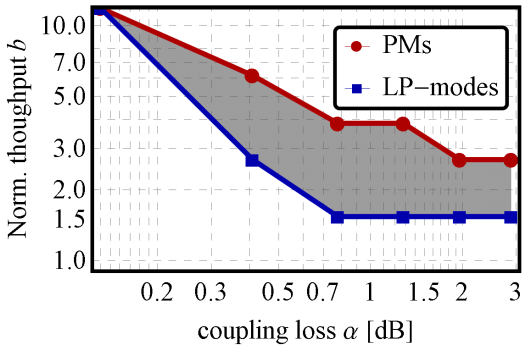


Fig. 49. Maximal allowable throughput values using PMs and LP-modes. A demultiplexed signal $u(t)$ is considered to be equalized, if its EVM value is below 0.23. Here a fixed filter length of $N_s = 2$ and $N_T = 12$ was used and the EVM value of each signal evaluated. Shaded area represents the improvement if the PMs are used as carriers.

This enhancement stays constant up to a coupling loss value of 1.5 dB (due to increasing simulation time, there are only two values between $\alpha = 1.3\text{dB}$ and $\alpha = 2.0\text{dB}$, so that the limit to which the improvement of 2.5 is given is not very accurate). After this, the performance difference is reduced down to a factor of 1.6. This shows that PM mode transmission offers some benefit towards LP-mode transmission if MIMO signal processing is used. In the case of having a receiver length of $N_s = 12$, a benefit exits if the coupling loss value does not

increase above 1.5 dB. The limit of this benefit is now analyzed by incrementing the temporal filter length of the digital processing unit.

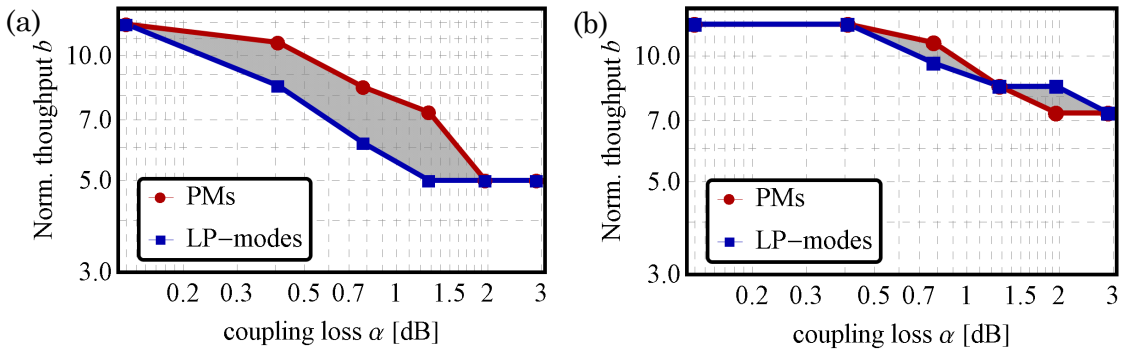


Fig. 50. Maximal throughput using PMs and LP-modes; Equalizer length is (a) $N_T = 24$ and (b) $N_T = 36$. Shaded area represents the difference between two carrier approaches.

The results are shown in Fig. 50 (a) and (b) using a maximal equalizer length of $N_T = 24$ per mode and $N_T = 36$ per mode respectively. The performance difference is reduced in comparison to the results presented in Fig. 49, which is not surprising when one considers the mathematical definition of PMs, which is frequency independent up to the first order. Fig. 50 (a) shows a maximum improvement of 1.3 in the area of roughly 0.9dB and 1.4dB coupling loss. For a filter length of $N_T = 36$, the throughput difference is basically zero, i.e. both carrier modes perform equally well. Having said this, the results will be summarized in the next subsection.

## 5.5 Summary

The results can therefore be summarized as follows:

- PM mode transmission in MDM scheme using coherent detection and MIMO digital signal processing makes only sense if the maximal normalized throughput value does not exceed 6 times the fiber bandwidth and losses induced by mode coupling does not exceed 1.5 dB. In this case, a 2.3 fold throughput improvement can be achieved compared to the conventional LP - mode transmission system.
- Increasing the temporal length of the MIMO processing unit can improve the general performance of the transmission system, but does not lead to improved performance when compared to a MDM transmission system that uses the LP-modes as carriers.

These results point out the fact that mode division multiplexing using PMs as carriers modes can be advantageous if the normalized throughput and coupling loss values do not exceed a value of $b = 6$ and $\alpha = 1.3\,\mathrm{dB}$ respectively. In this case the maximal number of taps per mode required to equalize the signal is $N_T = 12$. This can only be advantageous if the transmission length is short or if a mode dispersion compensating system is installed in the transmission link. The latter option is only feasible if the channel stays constant over the entire transmission time. To make MDM using PMs as carriers feasible, the complexity of exciting, tracking and de-multiplexing the PMs has to be less than the effort of using real time digital signal processing to equalize the signals at the output of the MMF. If the transmission link is bidirectional, the issue of feeding the channel information back to the transmitter to launch into the right PMs becomes manageable.

# 6. Summary, future work and conclusions

Throughout this work a matrix based, coherent field transmission model was developed for a MMF with arbitrary number of modes, having an infinitely extended parabolic profile. It was shown that the eigenmodes of the unperturbed MMF are well described using the Laguerre-Gaussian mode model, which can be applied to:

- MMF with truncated parabolic index profiles
- MMF with power law index profiles
- MMF with truncated parabolic index profiles and trenches

The differential group delay and propagation constants were compared, while neglecting the effect of chromatic dispersion and profile dispersion. The inclusion of these effects should be realized if for instance the laser source has a large line width or if the modulation bandwidth is very high. Profile dispersion can be included as shown for example in [35]. Including this effect would then require to optimize the exponent in power law profiles for each carrier wavelength $\lambda_0$ to obtain the highest possible MMF bandwidth. By neglecting this effect we has intrinsically assumed the optimal bandwidth for the wavelength of interest, which is here $\lambda_0 = 1.55\mu m$.

The transmission model is proven to model accurately mode coupling induced by random fiber imperfections such as micro-bends and splices in MMF with infinitely extended parabolic profile, which was proven by analytical and numerical results. Other random perturbations can be covered by this model, as long as the difference between the propagation constants of adjacent mode

groups $\Delta\beta$ is equally spaced, as it is in the case of a MMF with infinitely extended parabolic profile. Other types of MMF with near parabolic profiles can be modeled by this approach accurately as well, as long as the value $\Delta\beta$ does not deviate too much from the equally spaced case. The deviation of the mode coupling behavior when $\Delta\beta$ are not exactly equally spaced, will have to be evaluated in the future, to generalize the applicability of this model.

It was shown that losses induced by coupling is the main parameter which dictates the behavior of the DGD spread and MMF fiber bandwidth. In this sense, through measurement of the average bandwidth gain, the coupling loss $\alpha$ can be estimated and vice versa. The model is to be taken with care at this point, since it does not necessary deliver information about the micro-bends in the system. It delivers only the coupling effect of a MMF with random perturbations accurately, as long as the model and the system to which it is compared to have the same coupling losses. In addition it can be stated that this modelling approach is fast in comparison to other lumped models (for example [43]), since it does not require as many sections (100 vs. $10^4$). The minimal number of segments required to model a one km long MMF system accurately, was calculated to be 100. This analysis was limited to a 10 mode fiber but it is expected that MMFs guiding a larger number of modes do not require more segments. This still has to be verified rigorously though.

The concept of the principal modes was introduced for a non – unitary system, which was necessary due to the nature of the transmission channel, the MMF, which contains coupling losses. The group delay operator was used to evaluate the evolution of the group delay of the principal modes and the DGD spread reduction induced by the mode coupling process. This approach is limited though, since it does not allow the evaluation of the group delay up to a certain coupling loss value $\alpha$, since the matrix to be evaluated (group delay operator) becomes non-invertible due to the rank reduction of the matrix[44]. This effect is unfortunately mode dependent and a limit up to which this procedure works cannot be stated. A solution to this problem is the evaluation of the pseudo-inverse of the matrix. This procedure is not constrained to square matrices and

[44] Physically speaking it means that a principal mode is lost due to losses.

thus delivers a possible solution to the problem, but was not investigated rigorously enough to be presented here.

Further on this model was used to simulate a MMF in mode division multiplexing operation. Here the PMs were used as carrier modes and their performance compared towards the well-known LP-mode launch, using a combined eye opening and eye width penalty criterion. Here is as assumed that the channel is stationary and the channel is known at the receiver in order to estimate the individual PMs. It was shown the PM have the advantage of being relatively robust towards modal dispersion, modal mode coupling and crosstalk, as long as the modulation bandwidth of the signal modulated on each PM does not exceed roughly twice the fiber bandwidth[45]. This appears to be a general rule for PM transmission in MDM scheme without MIMO signal processing at the receiver and was verified for various MMF guiding different numbers of modes.

In addition the performance using MIMO digital signal processing was compared as well. Here the maximal throughput as function of coupling loss $\alpha$ was compared and evaluated for a six mode fiber, using QPSK as modulation format. Roughly twice the throughput was achieved using PM transmission compared to LP-mode transmission. Here the temporal filter length $N_s = 2$ of the MIMO DSP was kept constant and the maximal achievable throughput was compared. EVM was used as a metric to measure the quality of the signal, where a transmission channel was considered adequate for transmission if it could be equalized by the fixed equalizer down to an EVM value below 0.23. Increasing the amount of temporal filter taps $N_s$ of the MIMO DSP unit further than $N_s = 2$ does not yield significant performance increase in terms of a higher throughput difference. Further work in this area would include the measurement of the MMF temporal behavior, since this would dictate how fast the channel would need to be estimated, which would lead then to a re-estimation of the PMs as well. The application of PM is only thinkable if they can be excited without using costly adaptive systems and only for short to mid-range transmission systems, due to latency.

[45] This applies only under the assumption that coupling induced loss does not exceed 1.2 dB.

# Annex A

## A.1 Transformation to Laguerre differential equation

Here the transformation of Eq. (2.22) to Eq. (2.25) is shown using the trial solution $\psi_l(w) = g_l(w)(w/V)^l \exp(-w/2)$, where $w = VR^2$. First, the differential equation:

$$\left\{\frac{\partial^2}{\partial R^2} + \frac{1}{R}\frac{\partial}{\partial R} - \frac{l^2}{R^2} + u_r^2 - V^2R^2\right\}\psi_l(R) = 0 \tag{A.1}$$

is changed as to be a function of $w$ as:

$$\left\{w\frac{\partial^2}{\partial w^2} + \frac{\partial}{\partial w} - \frac{l^2}{4w} + \frac{\mu_r^2}{4V} - \frac{w}{4}\right\}\psi_l(w) = 0, \tag{A.2}$$

Here the following relations for the derivatives were used:

$$\begin{aligned}\frac{\partial}{\partial R} &= 2VR\frac{\partial}{\partial w},\\ \frac{\partial^2}{\partial R^2} &= 2V\frac{\partial}{\partial w} + (2VR)^2\frac{\partial^2}{\partial w^2}.\end{aligned} \tag{A.3}$$

Applying now the trial solution to Eq. (A.2) yields:

$$\left[w\frac{\partial^2 g(w)}{\partial w^2} + (l+1-w)\frac{\partial g(w)}{\partial w} + \left(\frac{\mu_r^2}{4V} - \frac{l+1}{2}\right)g(w)\right]\left(\frac{w}{v}\right)^{\frac{l}{2}}\exp\left(\frac{-w}{2}\right) = 0$$

(A.4)

Since the term after the square bracket is zero only at infinity, the term inside the square bracket needs to be solved. The solution that ensures that $g(w)$ decreases monotonically as $\rho$ increases is the generalized Laguerre polynomial $L_q^l(w)$ [30]. This requires the parameter:

$$\frac{\mu_r^2}{4V} - \frac{l+1}{2} = q, \tag{A.5}$$

to be a positive integer, here called $q$. This constrains the parameter $\mu_r^2$ to values of:

$$\mu_{l,q} = \sqrt{2V(2q+l+1)}. \tag{A.6}$$

If the definition of $\mu_{l,q} = \rho_0\sqrt{k_0^2 n_1^2(\lambda) - \beta_{l,q}^2}$ is now used, the propagation constant $\beta_{l,q}$ can be calculated as:

$$\beta_{l,q}(\omega) = n_1(\lambda)k_0\sqrt{1 - \frac{4\Delta(\lambda)(2q+l+1)}{V}}, \tag{A.7}$$

which is the result presented in Eq. (2.27).

## A.2 Power coupling spectrum

Here a more rigorous relation is formulated to show the coupling equivalence between splices and micro-bendings in a MMF with parabolic index profile. Equation (3.20) is formulated in terms of a slowly varying amplitude $c_\mu = a_\mu \exp(-j\beta_\mu z)$, where $c_\mu$ describes the amplitude of the $\mu^{\text{th}}$ eigenmode of the matrix differential equation now formulated as:

$$\frac{\partial c_\mu}{\partial z} = \sum_m c_m \kappa_{\mu,m} \exp\left[-j(\beta_m - \beta_\mu)z\right]. \tag{A.8}$$

From mode coupling theory it is known that coupling induced by small distortions occurs only within neighboring mode groups [39] [46], i.e. if $|\Delta M| = 1$. [47] After integrating Eq. (A.8) the following equations is obtained:

$$c_\mu(L) = \sum_m c_m \tilde{\kappa}_{\mu,m} \int_0^L f(z) \exp\left[-j(\beta_m - \beta_\mu)z\right] dz, \tag{A.9}$$

where the summation index $m$ extends only over the modes with DMG number $M$ and the index $\mu$ belongs to the mode with DMG number $M \pm 1$. Here it is assumed as in [40], that $\kappa_{\mu,m}(z) = \tilde{\kappa}_{\mu,m} f(z)$ where $\tilde{\kappa}_{\mu,m}$ is constant and $f(z)$ is the deformation function of the MMF as depicted in Fig. 51. The integral on the right side of Eq. (A.9) can be interpreted as the Fourier transform of $f(z)$ and is called the coupling spectrum, which is denoted here by $F(\Omega)$. If the Fourier transform of $f(z)$ vanishes at the spatial frequency $\Omega = \beta_m - \beta_\mu$, the $\mu^{\text{th}}$ mode will not be excited. The coupling spectrum:

$$F(\Omega) = \frac{1}{\sqrt{L}} \int_0^L f(z) \exp\left[-j\Omega z\right] dz \tag{A.10}$$

can also be formulated differently by applying twice a partial integration to Eq. (A.10) as:

[46] This has been shown also in [43] for a MMF with parabolic index profile using the Hermite-Gauss modes.

[47] $|\Delta M|$ describes the PMG number difference of modes belonging to adjacent mode groups.

$$F(\Omega) = -\frac{jf(z)}{\Omega\sqrt{L}}\exp(-j\Omega z)\Big|_0^L + \frac{1}{\Omega^2\sqrt{L}}\frac{\partial f(z)}{\partial z}\exp(-j\Omega z)\Big|_0^L - \frac{1}{\Omega^2\sqrt{L}}\int_0^L \frac{\partial^2 f(z)}{\partial z^2}\exp(-j\Omega z)\,dz. \tag{A.11}$$

It is now assumed that the first two terms in Eq. (A.11) can be neglected since their values do not contribute significantly to $F(\Omega)$. This results in:

$$F(\Omega) = -\frac{1}{\Omega^2\sqrt{L}}\int_0^L \frac{\partial^2 f(z)}{\partial z^2}\exp(-j\Omega z)\,dz. \tag{A.12}$$

Equation (A.10) and Eq. (A.12) allow the estimation of the power coupling spectrum using either the deformation function $f(z)$ or its second derivative $\partial^2 f(z)/\partial z^2$. Since the second derivative of $f(z)$ can be interpreted as the curvature function $1/R(z)$, it is more convenient to use the formulation in Eq. (A.12) for the description of micro-bendings, while the formulation in Eq. (A.10) is used here to describe the power coupling spectrum related to random splice mismatches. Since a statistical model is considered here consisting of MMF sections with constant curvature and random amplitude and sign, it is necessary to evaluate the ensemble average of the power coupling spectrum $\left\langle \left|F(\Omega)\right|^2 \right\rangle$, where $\langle\ \rangle$ denotes the ensemble average. The power coupling spectrum for the curvature function can be obtained from the Fourier transform of the autocorrelation function as derived in [6] by:

$$\left\langle \left|F_{1/R}(\Omega)\right|^2 \right\rangle = \frac{1}{\Omega^4 L}\int_{-\infty}^{\infty} c_{1/R}(u)\exp(-j\Omega u)\,du, \tag{A.13}$$

where $c_{1/R}(u)$ is the autocorrelation function[48] related to the curvature function $1/R(z)$. The autocorrelation function of a MMF with piecewise constant curvature sections and fixed length $L_{seg}$ is given by:

[48] The integral boundary $L$ can be extended to infinity since the autocorrelation function is zero there.

$$c_{1/R}(u) = \left\langle \frac{1}{R(z)} \frac{1}{R(z+u)} \right\rangle = \begin{cases} \dfrac{L_{seg} - |u|}{L_{seg}} \sigma_{1/R}^2 & |u| \le L_{seg}, \\ 0 & |u| \ge L_{seg}. \end{cases} \tag{A.14}$$

Here $\sigma_{1/R}$ denotes the standard deviation of the inverse bending radius which follows a truncated Gaussian distribution. Applying Eq. (A.13) with the definition given of $c_{1/R}(u)$ in Eq. (A.14) yields [40]:

$$\left\langle \left| F_{1/R}(\Omega) \right|^2 \right\rangle = \frac{2\sigma_{1/R}^2}{L_{seg}\Omega^6} \left(1 - \cos\left(\Omega L_{seg}\right)\right). \tag{A.15}$$

By assuming that $\Omega L_{seg} \gg 2\pi$ and averaging over the length, following expression is obtained [40]:

$$\left\langle \left| F_{1/R}(\Omega) \right|^2 \right\rangle = \frac{2\sigma_{1/R}^2}{L_{seg}\Omega^6}. \tag{A.16}$$

As discussed earlier, the definition given in Eq. (A.10) is used to estimate the power coupling spectrum $F_{spl}^2(\Omega)$ of a MMF with piece-wise constant splices. The power coupling spectrum can be obtained by taking into account Eq. (A.10)

$$\left\langle \left| F_{spl}(\Omega) \right|^2 \right\rangle = \frac{1}{L} \int_{-\infty}^{\infty} c_{spl}(u) \exp(-j\Omega u)\, du. \tag{A.17}$$

Its autocorrelation function $c_{spl}(u)$ is given by:

$$c_{spl}(u) = \left\langle f_{spl}(z) f_{spl}(z+u) \right\rangle, = \begin{cases} \dfrac{L_{seg} - |u|}{L_{seg}} \sigma_{spl}^2 & |u| \le L_{seg}, \\ 0 & |u| \ge L_{seg}. \end{cases} \tag{A.18}$$

Here $f_{spl}(z)$ is the deformation function describing the splice offsets and $\sigma_{spl}^2$ describes the standard deviation of splice offset distribution which also follows a truncated Gaussian distribution. The average power coupling spectrum is then given as:

$$\left\langle \left| F_{spl}(\Omega) \right|^2 \right\rangle = \frac{2\sigma_{spl}^2}{L_{seg}\Omega^2}. \tag{A.19}$$

Equation (A.16) and Eq. (A.19) describe the power coupling spectra for a MMF link with random micro-bendings and splices respectively. Both spectra have a different dependency of $\Omega$, as shown in Fig. 52, which might lead to the conclusion that both coupling mechanisms behave differently.

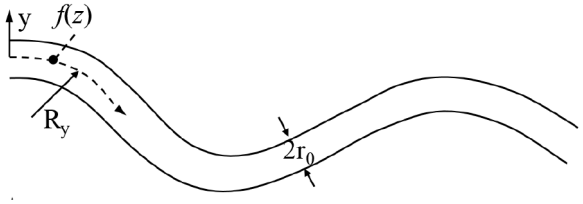


Fig. 51. Random micro-bends in y – direction with radius $R_y$ in a MMF and the respective deformation function $f(z)$

If the spatial frequency is now sought, at which both power coupling spectra yield the same results, following results is obtained:

$$\Omega = \sqrt{\frac{\sigma_{1/R}}{\sigma_{spl}}}. \tag{A.20}$$

If Eq. (3.19) is taken into account which states that $\Delta x = r_0^2 / 2\Delta R$ and the definition of the standard deviation is used, the following result is obtained:

$$\Omega = \frac{\sqrt{2\Delta}}{r_0}. \tag{A.21}$$

This spatial frequency $\Omega$ has the exact value of $\Delta\beta$ between neighboring mode groups in a MMF with infinite parabolic profile. Since this difference applies for all adjacent mode groups, all guided modes require a deformation with a spatial frequency of $\Omega = \Delta\beta$ in order to couple to one another. In this particular case it simply means that both coupling spectra behave identically. Having proved this, it is worthwhile analyzing the complete set of coupling spectra that have the following dependency:

$$\left\langle \left| F(\Omega) \right|^2 \right\rangle \propto \frac{1}{\Omega^n}, \tag{A.22}$$

where $n$ is an arbitrary number. As shown in Fig. 52 (b), all this curves intersect at one point, namely $\Omega = 1$. Since it was proven before, that the

coupling spectra of splices and micro-bends intersect in one location, it can be deduced that all curves intersect at the exact same location as well. This has the following consequence. All coupling phenomena, which have a coupling spectra proportional to Eq. (A.22) can be described accurately with this model.

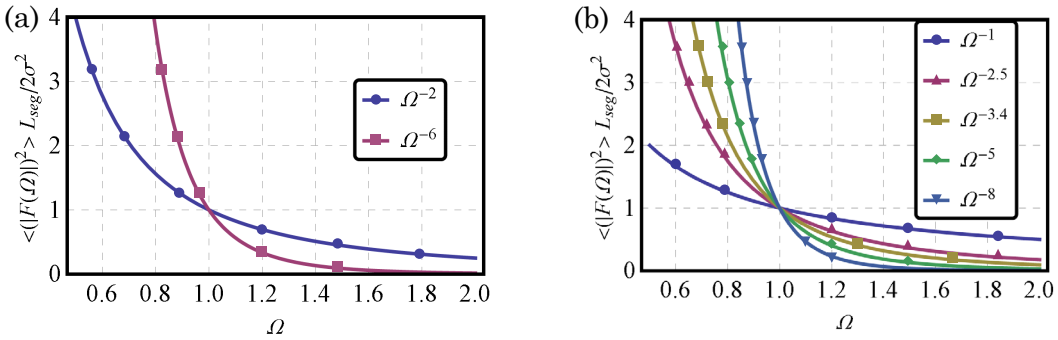


Fig. 52. (a) Power coupling spectrum of the deformation function of micro-bending and splices; (b) general family of power coupling spectra that intersect at $\Omega=1$

## A.3 Digital modulation

Digital modulation and detection consist of transferring information in the form of bits over some communication channel. This information is encoded into certain amplitude and/or phase levels of some analog signal $s(t)$ and then imprinted on a carrier wave, with angular carrier frequency $\omega_0$. This causes a spectral shift of the signal, which is then called a pass band signal. This can be formulated mathematically as [83]:

$$s(t)\cos(\omega_0 t) = a(t)\cos\left[2\pi\left(f_0 t - f(t)\right)t + \phi(t)\right]. \tag{A.23}$$

Where $a(t)$ describes the pure amplitude modulation, $f(t)$ the frequency modulation and $\phi(t)$ the phase modulation. Frequency modulation will not be dealt here, i.e. $f(t) = 0$. Eq. (A.23) can also be written in complex notation as:

$$s(t)\cos\left(2\pi f_0 t + \phi(t)\right) = \mathrm{RE}\left\{\underline{s}(t)\exp\left(j2\pi f_0 t\right)\right\}. \tag{A.24}$$

Here $\mathrm{RE}\{x\}$ refers to the real part of $x$ and $\underline{s}(t) = s_I(t) + js_Q(t)$ is the complex envelope, now divided into real and imaginary part, $s_I(t)$ and $s_Q(t)$ respectively.

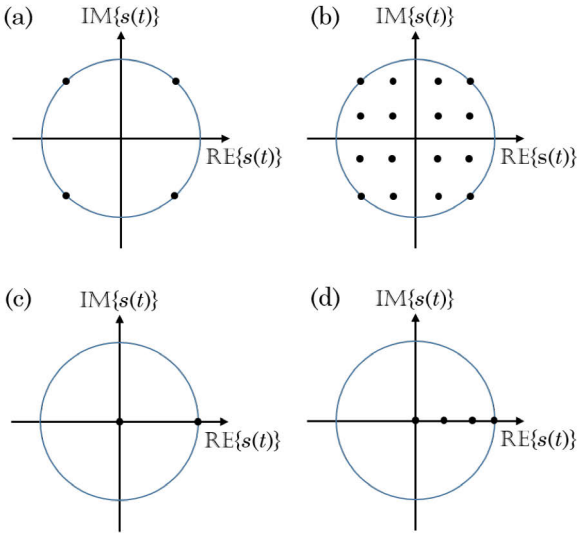


Fig. 53. Constellation diagram for various (no pulse shaping) signal types; (a) 4 QAM (b) 16 QAM (c) 2 PAM (OOK) and (d) 4 PAM.

If no phase modulation exists, the envelope $s(t)$ is real, i.e. $s_Q(t) = 0$, and the modulation is called multilevel pulse amplitude modulation (MPAM). If both amplitude and phase modulation exist, the signal is called multilevel

quadrature amplitude modulation (MQAM). Some examples are given in Fig. 53 in the so called constellation diagram. The complex envelope $\underline{s}(t) = s_I(t) + js_Q(t)$ consist basically out of two signals with envelope $s_I(t)$ and $s_Q(t)$ , phase shifted by 90 degrees. These signals are in general described by their amplitude level and a pulse shape as: $s_I(t) = A_{I,i}g(t)$ and $s_Q(t) = A_{Q,i}g(t)$. The pulse shape of the signal $g(t)$ is imprinted on the binary signal here in the frequency domain using a fifth order Bessel filter with the following transfer function [84]:

$$H(\omega) = \prod_i^5 \left(1 + a_i f_n + b_i f_n^2\right)^{-1}, \tag{A.25}$$

where $a_i$ and $b_i$ are real coefficients. These filter coefficients for several orders of Bessel filters are given in Table VII.

TABLE VII. FILTER COEFFICIENTS FOR BESSEL FILTER

| Parameter | Filter order | | | | |
|---|---|---|---|---|---|
| | 1 | 2 | 3 | 4 | 5 |
| $a_i$ | 1 | 1.3617 | 0.7560 | 1.3397 | 0.6656 |
| | | | 0.9996 | 0.7443 | 1.1402 |
| | | | | | 0.6216 |
| $b_i$ | 0 | 0.6180 | 0 | 0.4889 | 0 |
| | | | 0.4772 | 0.3890 | 0.4128 |
| | | | | | 0.3245 |

Here, only two types of signals will be treated: 2 PAM or on off keying (OOK) and 4 QAM signals or quadrature phase shift keying. The generation of an OOK signal is in principle the simplest way of modulating since it basically requires only to turn the carrier off, for a logical zero and to turn in on, for a logical one. Direct modulation of the transmitter is possible, but it adds an unwanted frequency modulation (known as chirp) which widens the required bandwidth and therefore reduces the spectral efficiency. For this reason a mach-zehnder type modulator (MZM) is often used [5], which is capable of suppressing this effect if it's driven in a push-pull configuration. The OOK signal can therefore be described as [83]:

$$s_i(t) = \mathrm{RE}\left\{A_i g(t) \exp(j\omega_0 t)\right\} \qquad 0 \le t \le T_s \gg 1/f_c \tag{A.26}$$

Here $A_i$ describes the amplitude level which takes only two values: zero and one for OOK keying signals and $T_s$ is the symbol time. The QPSK signal, is a special case of the quadrature amplitude modulation since the magnitude of each constellation point is unity (if properly normalized) and the information is basically coded on the phase. It can be described over one symbol time $T_s$ as [83]:

$$s_i(t) = \mathrm{RE}\left\{Ag(t)\exp\left(j2\pi(i-1)/M + j\pi/4\right)\exp\left(j\omega_0 t\right)\right\}, \qquad \text{(A.27)}$$

for $0 \le t \le T_s$.

# 7. Acknowledgment

First of all I want to thank God for giving me the strength, endurance and patience throughout this work. Without him nothing would have been possible.

Second of all, I would like to thank my supervising Professor Klaus Petermann, who mentored this work throughout all its stages with many fruitful comments and discussions. I am grateful for his support and mentorship, which thought me many important aspects of scientific working. I would also like to thank Professor Christian -Alexander Bunge for his help, especially at the beginning of this work. His comments were very valuable and his good mood was always very welcome. Prof. Krummrich and Dr. Bülow also have my thanks for agreeing to supervise this dissertation.

In addition, I would also like to thank my former colleagues at the TU – Berlin. Coffee brakes were always a good basis for discussion and Dimis wisdom will always be remembered with laughter. I will remember that time with good thoughts.

In addition, I would also like to thank my wife and daughter, who supported me at home during all this time. I wish to thank my wife for being such a loving and caring person on whom I could always take comfort with. They both are the happiness of life.

I will conclude thanking my parents for supporting me during all my studies, financially and emotionally. All their efforts are well remembered and they are very much appreciated.

# 8. Acronyms

| ACRONYM | DEFINITION |
|---|---|
| BER | **B**it **E**rror **R**atio |
| BTB | **B**ack **T**o **B**ack |
| CWDM | **C**oarse **W**avelength **D**ivision **M**ultiplexing |
| DEMUX | **DE** – **M**ultiplexing |
| DGD | **D**ifferential **G**roup **D**elay |
| DMG | **D**egenerate **M**ode **G**roup |
| DSP | **D**igital **S**ignal **P**rocessing |
| DWDM | **D**ense **W**avelength **D**ivision **M**ultiplexing |
| EMD | **E**quilibrium **M**ode **D**istribution |
| EO | **E**ye **O**pening |
| EOP | **E**ye **O**pening **P**enalty |
| EVM | **E**rror **V**ector **M**agnitude |
| EW | **E**ye **W**idth |
| EWP | **E**ye **W**idth **P**enalty |
| FEC | **F**orward **E**rror **C**orrection |
| FIR | **F**inite **I**mpulse Response |
| FMF | **F**ew **M**ode **F**iber |
| GDO | **G**roup **D**elay **O**perator |
| LED | **L**ight **E**mitting **D**iode |
| LG | **L**aguerre-**G**auss |
| LN | **L**ocal **N**ormal |
| LP | **L**inear **P**olarized |
| MD | **M**ode **D**ispersion |
| MDL | **M**ode **D**ependent **L**oss |
| MDM | **M**ode **D**ivision **M**ultiplexing |
| MGDM | **M**ode **G**roup **D**ivision **M**ultiplexing |
| MIMO | **M**ultiple **I**nput **M**ultiple **O**utput |
| MISO | **M**ultiple **I**nput **S**ingle **O**utput |
| MMF | **M**ultiple **M**ode **F**iber |
| MPAM | **M**ultilevel **P**ulse **A**mplitude **M**odulation |

| **ACRONYM** | **DEFINITION** |
|---|---|
| MQAM | **M**ultilevel **Q**uadrature **A**mplitude **M**odulation |
| MUX | **M**ultiplexing |
| MZM | **M**ach **Z**ehnder **M**odulator |
| NRZ | **N**on **R**eturn to **Z**ero |
| OOK | **O**n **O**ff Keying |
| PAM | **P**ulse **A**mplitude **M**odulation |
| PD | **P**hoto **D**iode |
| PDF | **P**robability **D**ensity **F**unction |
| PM | **P**rincipal **M**ode |
| PMD | **P**olarization **M**ode **D**ispersion |
| PMF | **P**robability **M**ass **F**unction |
| PRBS | **P**seudo **R**andom **B**it **S**equence |
| PSP | **P**rincipal **S**tates of **P**olarization |
| QAM | **Q**uadrature **A**mplitude **M**odulation |
| QPSK | **Q**uadrature **P**hase **S**hift **K**eying |
| RMS | **R**oot **M**ean **S**quare |
| RX | **R**eceiver |
| SDM | **S**pace **D**ivision **M**ultiplexing |
| SER | **S**ymbol **E**rror **R**atio |
| SISO | **S**ingle **I**nput **S**ingle **O**utput |
| SMF | **S**ingle **M**ode **F**iber |
| SNR | **S**ignal to **N**oise **R**atio |
| VCSEL | **V**ertical **C**avity **S**urface **E**mitting **L**aser |
| WDM | **W**avelength **D**ivision **M**ultiplexing |
| WKB | **W**entzel **K**ramers **B**rillouin |

# 9. List of figures

# 10. List of publications

1 A. A. Juarez, S. Warm, C.-A. Bunge, P. Krummrich, K. Petermann, Perspectives of Principal Mode Transmission in a Multi-Mode Fiber, Proc. ECOC 2010, paper P4.10, Turin, Italy, Sept. 2010.

2 A. A. Juarez, S. Warm, C. -A. Bunge, K. Petermann, Number of usable Principal Modes in a Mode Division Multiplexing Transmission for different Multi-mode fibers, Proc. Optical Fiber Communications Conference (OFC) 2011, paper JThA34, Los Angeles, 2011.

3 S. Warm, A. A. Juarez, B. Wohlfeil, K. Petermann, Cross-Talk in Mode-Division-Multiplex Optical Fiber Transmission Systems, Proc. Transparent Optical Networks (ICTON), 2011 13th International Conference, Stockholm, 2011.

4 A. A. Juarez, S. Warm, C. -A. Bunge, K. Petermann, Mode Division Multiplexing using Principal Modes as Carriers in MMFs with Different Number of Guided Modes. Proceedings of Photonic Networks, 12. ITG Symposium, pp. 136 – 140. May 2013.

5 H. Louchet, A. A. Juarez, C.-A. Bunge, P. M. Krummrich, A. Richter, K. Petermann, Capacity Upgrade of Legacy Fiber Plant using SDM and Multimode/Multicore EDFAs, Proc. ECOC 2011, paper P 1.74, Geneva, Swiss, 2011.

6 A. A. Juarez, C.-A. Bunge, S. Warm, and K. Petermann, Perspectives of principal mode transmission in mode-division-multiplex operation, Optics Express, vol. 20, no. 13, p. 13810, 2012.

7 A. A. Juarez, D. Kroushkov, C. -A. Bunge, K. Petermann, Comparison of MIMO receiver complexity in a MDM transmission system using Principal modes and LP Modes; Proceedings of Photonic Networks, 14. ITG Symposium, pp. 57-60, May 2013.

8 A. A. Juarez, E. Krune, K. Petermann, Equivalent Modeling of Micro-bending in Multimode-fibers with Parabolic Index Profile using Discrete

Coupling; Proc. Conference on Lasers and Electro-Optics (CLEO Europe 2013), paper CI P. 13 Tue, München, May 2013.

9 A. A. Juarez, E. Krune, C. Bunge, S. Warm and K. Petermann, Modeling of Micro-bending in Multimode Fibers with Parabolic Index Profile using Discrete Coupling Points, in Proc. 39th ECOC, 2013, paper P.1.13, London.

10 A. A. Juarez, E. Krune, C. Bunge, S. Warm and K. Petermann, Modeling of Mode Coupling in Multimode Fibers with respect to Bandwidth and Loss, Journal of Lightwave Technology, vol. 32, no. 8, p. 1549, 2014.

# References

[1] E. B. Desurvire, "Capacity Demand and Technology Challenges for Lightwave Systems in the Next Two Decades," *Journal of Lightwave Technology*, vol. 24, no. 12, pp. 4697-4710, December 2006.

[2] R. E. Freund, C. -A Bunge, N. N. Ledentsov, and Ch. Caspar, "High-Speed Transmission in Multimode Fiber," *Journal of Lightwave Technology*, vol. 28, no. 4, pp. 569 - 586, February 2010.

[3] C. F Lam et al., "Fiber optic Communicatios Technologies: What`s Needed for Datacenter Network Operations," *IEEE Communications Magazine*, vol. 48, no. 7, pp. 32-39, July 2010.

[4] H. Liu, C. F. Lam, and C. Johnson, "Scaling Optical Interconnects in Datacenter Networks," in *18th IEEE Symposium on High Performance Interconnects*, Mountain View, CA, 2010, pp. 113-116.

[5] E. Voges and K. Petermann, *Optische Kommunikationstechnik*, 1st ed. Heidelberg, New York: Springer Verlag, 2002.

[6] D. Marcuse, *Light transmission optics*. New York: Bell Telephone Laboratories, 1972.

[7] J. D. Ingham, R. V. Penty, and I. H. White, "10 Gb/s & 20 Gb/s extended-reach multimode-fiber datacommunication links using multilevel modulation and transmitter-based equalization," in *Proc. of Optical Fiber Conference (OFC)*, San Diego, CA., 2008, p. OTuO7.

[8] A. V. Rylyakov et al., "Transmitter Predistortion for Simultaneous Improvements in Bit Rate, Sensitivity, Jitter, and Power Efficiency in 20 Gb/s CMOS-Driven VCSEL Links," *Journal of Lightwave Technology*, vol. 30, no. 4, pp. 399-405, February 2012.

[9] A. Vahdat, H. Liu, X. Zhao, and C. Johnson, "The Emerging Optical Data Center," in *Proc. of Optical Fiber Conference (OFC)*, Los Angeles, CA, 2011, p. OTuH2.

[10] T. Koonen, H. van den Boom, I. T. Monroy, and G. Khoe, "High Capacity Multi-Service In-House Networks using Mode Group Diversity Multiplexing," in *Proc. of Optical Fiber Conference (OFC)*, Los Angeles, CA, 2004, p. FG4.

[11] C. P. Tsekrekos, A. Martinez, F. M. Huijskens, and A. M. Koonen, "Mode group Diversity Multiplexing Transceiver Design for Graded-Index Multimode Fibres," in *Proc. of European Conference Of Optical Communications (ECOC)*, Galsgow, 2005, p. We4.P.113.

[12] C. P. Tsekrekos, A. Martinez, F. M. Huijskens, and A. J. M. Koonen, "Design considerations for a transparent mode group diversity multiplexing link," *IEEE Photonic Technology Letters*, vol. 18, no. 22, pp. 2359 - 2361, November 2006.

[13] L. Raddatz, I. H. White, D. G. Cunningham, and M. C. Nowell, "An Experimental and Theoretical Study of the Offset Launch Technique for the Enhancement of the Bandwidth of Multimode Fiber Links," *Journal of Lightwave Technology*, vol. 16, no. 3, pp. 324-331, March 1998.

[14] H. S. Chen, H. P. A. van den Boom, and A. M. J. Koonen, "30Gbit/s 3 × 3 Optical Mode Group Division Multiplexing System with Mode-Selective Spatial Filtering," in *Proc. of Optical Fiber Conference (OFC)*, Los Angeles, CA, 2011, p. OWB1.

[15] C. P. Tsekrekos and A. M. J. Koonen, "Mode-selective spatial filtering for increased robustness in a mode group diversity multiplexing link," *Optics Letters*, vol. 32, no. 9, pp. 1041-1043, May 2007.

[16] K. M. Patel, A. Polley, K. Balemarthy, and S. E. Ralph, "Spatially Resolved Detection and Equalization of Modal Dispersion Limited Multimode Fiber Links," *Journal of Lightwave Technology*, vol. 24, no. 7, pp. 2629-2636, July 2006.

[17] M. Awad, I. Dayoub, A. Okassa M'Foubat, and J. M. Rouvaen, "The inter-modes mixing effects in Mode Group Diversity Multiplexing," *Optics Communications*, no. 282, pp. 3908–3917, February 2009.

[18] A. Agmon and M. Nazarathy, "Broadcast MIMO over multimode optical interconnects by modal beamforming," *Optics Express*, vol. 15, no. 20, pp. 13123–13128, October 2007.

[19] M. Nazarathy and A. Agmon, "Coherent Transmission Direct Detection MIMO Over Short-Range Optical Interconnects and Passive Optical Networks," *Journal of Lightwave Technology*, vol. 26, no. 14, pp. 2037-2045, July 2013.

[20] S. Fan and J. M. Kahn, "Principal modes in multimode waveguides," *Optics Letters*, vol. 30, no. 2, pp. 135-137, Januar 2005.

[21] B. Wohlfeil, C. Stamatiadis, L. Zimmermann, and K. Petermann, "Compact Fiber Grating Coupler on SOI for Coupling of Higher Order Fiber Modes," in *Proc. of Optical fiber conference (OFC)*, Los Angeles, 2013, p. OTh1B.

[22] R. Ryf et al., "Mode-Division Multiplexing Over 96 km of Few-Mode Fiber Using Coherent 6 x 6 MIMO Processing," *Journal of Lightwave Technology*, vol. 30, no. 4, pp. 521-531, February 2012.

[23] X. Shen, J. M. Kahn, and M. A. Horowitz, "Compensation for multimode fiber dispersion by adaptive optics," *Optics letters*, vol. 30, no. 22, pp. 2985-2987, November 2005.

[24] R. A. Panicker, J. M. Kahn, and S. P. Boyd, "Compensation of Multimode Fiber Dispersion Using Adaptive Optics via Convex Optimization," *Journal of Lightwave technology*, vol. 26, no. 10, pp. 1295-1303, May 2008.

[25] R. A. Panicker, J. P. Wilde, and J. M. Kahn, "10 x 10 Gb/s DWDM Transmission through 2.2km MMF using adaptive optics," *IEEE Photonic Technology Letters*, vol. 19, no. 15, pp. 1154-1156, August 2007.

[26] X. Chen et al., "25 Gb/s transmission over 820 m of MMF using a multimode launch from an integrated silicon photonics transceiver," *Optics Express*, vol. 22, no. 2, pp. 2070-2077, January 2014.

[27] A. W. Snyder and J. D. Love, *Optical waveguide Theory*. London: Chapman and Hall, 1983.

[28] K. Petermann. (2012) Einführung in die Optische Nachrichtentechnik. [Online]. http://www.hft.tu-berlin.de/menue/lehre/veranstaltungen/optische_nachrichtentechnik/

[29] D. Gloge, "Weakly guiding fibers," *Applied Optics*, vol. 10, no. 10, pp. 2252 - 2258, October 1971.

[30] M. Abramowitz and I. A. Stegun, *Handbook of mathematical functions*, 2nd ed. New York: Dover Publications, 1965.

[31] H. -G. Unger, *Planar optical waveguides and fibers*.: Oxford University Press, 1977.

[32] K. Petermann, "Nonlinear Distortion and Noise in Optical Communication Systems due to Fiber Connectors," *IEEE Journal of Quantum Electronics*, vol. QE-16, no. 7, pp. 761-770, July 1980.

[33] L. Papula, *Mathematik für Ingenieure und Naturwissenschaftler*, 13th ed. Heidelberg: Vieweg, 2011, vol. 1.

[34] C. -A. Bunge, "Gigabit-Übertragung mit Vielmodenfasern," Technische Universität, Berlin, Gemany, Dissertation 2003.

[35] W. L. Mammel and L. G. Cohen, "Numerical prediction of fiber transmission characteristics from arbitrary refractive-index profiles," *Applied Optics*, vol. 21, no. 4, pp. 669-703, Feb. 1982.

[36] J. A. Arnaud, *Beam and fiber optics*. New York: Academic Press, 1976.

[37] Robert Olshansky, "Effect of the cladding on pulse broaderning in graded-index optical waveguides," *Applied Optics*, vol. 16, no. 8, pp. 2171 - 2174, August 1977.

[38] Katsunari Okamoto and Takanori Okoshi, "Analysis of Wave Propagation in Optical Fibers Having Core with a-power Refractive-Index Distribution and Uniform Cladding," *IEEE Transactions on microvave theory and techniques*, vol. MTT-24, no. 7, pp. 416-421, July 1976.

[39] D. Marcuse, *Theory of Dielectric Optical Waveguides*. New York and London: Academic Press, 1974.

[40] D. Marcuse, "Losses and Impulse Response of a Parabolic Index Fiber With Random Bends," *The Bell System Technical Journal*, vol. 52, no. 8, pp. 1423-1437, October 1973.

[41] R. Olshansky, "Mode Coupling Effects in Graded-index Optical Fibers," *Applied Optics*, vol. 14, no. 4, pp. 935-945, April 1975.

[42] K. Kitayama, S. Seikai, and N. Uchida, "Impulse response prediction based on Experimental Mode Coupling Coefficient in a 10 km Long Graded Index Fiber," *IEEE Journal of Quantum Electronics*, vol. QE-16, no. 3, pp. 356-362, March 1980.

[43] M. B. Shemirani, W. Mao, R.l A. Panicker, and J. M. Kahn, "Principal Modes in Graded-Index Multimode Fiber in Presence of Spatial- and Polarization-Mode Coupling," *Journal of Lightwave Technologie*, vol. 27, no. 10, pp. 1248-1261, May 2009.

[44] H. E. Rowe, *Electromagnetic PropagationIin Multi-Mode Random Media*. New York: Wiley, 1990.

[45] K. Petermann, "Theory of Microbending Loss in Monomode Fibres with Arbitrary Refractive Index Profile," *Archiv für Elektronik und Übertragungstechnik AEÜ*, vol. 30, no. 30, pp. 337-342, 1976.

[46] I. A. White and S. C. Mettler, "Modal Analysis of Loss and Mode Mixing in Multimode Parabolic index Splices," *The Bell System Technical Journal*, vol. 62, no. 5, pp. 1189-1207, Nov. 1982.

[47] G. B. Hocker, "Fiber-optic sensing of pressure and temperature," *Applied Optics*, vol. 18, no. 9, pp. 1445-1448, May 1979.

[48] T Toyoda and M. Yabe, "The temperature dependence of the refractive indices of fused silica and crystal quartz," *Journal of Physics D: Applied Physics*, vol. 16, no. 5, pp. L97-L100, May 1983.

[49] Massimiliano Salsi et al., "Mode-Division Multiplexing of 2x100 Gb/s Channels Using an LCOS-Based Spatial Modulator," *Journal of Lightwave Technology*, vol. 30, no. 4, pp. 618-623, February 2012.

[50] F. Mezzadri, "How to Generate Random Matrices from the Classical Compact Groups," *Notices of the AMS*, vol. 54, no. 5, pp. 592-604, May 2007.

[51] Kean-Po Ho and Joseph M. Kahn, "Statistics of Group Delays in Multimode Fiber With Strong Mode Coupling," *Journal of Lightwave Technology*, vol. 29, no. 21, pp. 3119-3128, November 2011.

[52] A. A. Juarez, C. A. Bunge, S. Warm, and K. Petermann, "Perspectives of principal mode transmission in mode-division-multiplex operation," *Optics Express*, vol. 20, no. 13, pp. 13810-13824, June 2012.

[53] N. Gisin and B. Huttner, "Combined effects of polarization mode dispersion and polarization dependent losses in optical fibers," *Optics communications*, no. 142, pp. 119-125, October 1997.

[54] A. A. Juarez, E. Krune, S. Warm, C. -A. Bunge, and K. Petermann, "Modeling of Mode Coupling in Multimode Fibers with Respect to Bandwidth and Loss," *Journal of Lightwave Technology*, vol. 32, no. 8, pp. 1549-1558, April 2014.

[55] A. A. Juarez, E. Krune, and K. Petermann, "Equivalent Modeling of Micro-bending in Multimode-fibers with Parabolic Index Profile using Discrete Coupling," in *Proc. Conference on Lasers and Electro-Optics (CLEO Europe 2013)*, Munich, Germany, 2013, p. P.13.

[56] A. A. Juarez, E. Krune, C.-A. Bunge, S. Warm, and K. Petermann, "Modeling of Micro-bending in Multimode Fibers with ParabolicIndex Profile using Discrete Coupling Points," in *Proc. of European Conference of Optical Communications (ECOC)*, London, 2013, p. p.1.13.

[57] S. Warm and K. Petermann, "Splice loss requirements in multi-mode fiber mode-division-multiplex transmission links," *Optics Express*, vol. 21, no. 1, pp. 519-532, 2013.

[58] K. P. Ho and J. M. Kahn, "Mode-dependent loss and gain: statistics and effect on mode-division multiplexing," *Optics Express*, vol. 19, no. 17, pp. 16612-16635, August 2011.

[59] G. H. Galub and C. F. Van Loan, *Matrix computations*, 3rd ed.: Johns Hopkins University Press, 1996.

[60] P. J. Winzer and G. Foschini, "MIMO capacities and outage probabilities in spatially multiplexed optical transport systems," *Optics Express*, vol. 19, no. 17, pp. 16680-16696, August 2011.

[61] S. Ö Arik, D. Askarov, and J. M. Kahn, "Effect of Mode Coupling on Signal Processing Complexity in Mode-Division Multiplexing," *Journal of Lightwave Technology*, vol. 31, no. 3, pp. 423-431, February 2013.

[62] L. G. Cohen, P. Kaiser, and Chinlon Lin, "Experimental techniques for evaluation of fiber transmission Loss and Dispersion," *Proceedings of the IEEE*, vol. 68, no. 10, pp. 1203-1209, June 1980.

[63] Neng Bai et al., "Mode-division multiplexed transmission with inline few-mode fiber amplifier," *Optics Express*, vol. 20, no. 3, pp. 2668-2680, January 2012.

[64] R. Ryf et al., "Mode-multiplexed 6×20-GBd QPSK transmission over 1200-km DGD-compensated few-mode fiber," in *Proc. of Optical Fiber Conference (OFC)*, Los Angeles, California, March 2012.

[65] J. P. Gordon and H. Kogelnik, "PMD fundamentals: Polarization mode dispersion in optical fibers," *Proceedings of the National Academy of Sciences*, vol. 97, no. 9, pp. 4541-4550, April 2000.

[66] C. D. Poole and R. E. Wagner, "Phenomenological approach to polarization dispersion in long single mode fibers," *Electronic letters*, vol. 22, no. 19, pp. 1029-1030, Sep. 1986.

[67] K. P. Ho and J. M. Kahn, "Linear Propagation Effects in Mode-Division Multiplexing Systems," *Journal of Lightwave Technology*, vol. 32, no. 4, pp. 614-628, February 2014.

[68] G. Stepniak, L. Maksymiuk, and J. Siudak, "Increase Multimode Fiber Tranmission Capacity by Mode Selective Spatial light modulation," *Journal of Lightwave technology*, vol. 29, no. 13, pp. 1980-1987, July 2011.

[69] R. A. Panicker, J. M. Kahn, and S. P. Boyd, "Compensation of Multimode Fiber Dispersion Using Adaptive Optics via Convex Optimization," *Journal of Lightwave technology*, vol. 26, no. 10, pp. 1295-1303, May 2008.

[70] J. Carpenter and T. D. Wilkinson, "All Optical Mode-Multiplexing Using Holography and Multimode Fiber Couplers," *Journal of Lightwave Technology*, vol. 30, no. 12, pp. 1978-1984, June 2012.

[71] D. Flamm et al., "All-Digital Holographic Tool for Mode Excitation and Analysis in Optical Fibers," *Journal of Lightwave Technology*, vol. 7, pp. 1023-1032, April 2013.

[72] R. Küng. (2011) Nachrichtentechnik und Mobilkommunikation NTM1. [Online]. https://home.zhaw.ch/~kunr/ntm.html

[73] L. Raddatz, I. H. White, D. H. Cunningham, and M. C. Nowell, "Increasing the bandwidth-distance product of multimode fibre using offset launch," *Eletronics Letters*, vol. 33, no. 3, pp. 232-233, January 1997.

[74] A. A. Juarez, S. Warm, C. A. Bunge, P. Krummrich, and K. Petermann, "Perspectives of principal mode transmission in multimode fibers," in *Proc. of European Conference of Optical Communications (ECOC)*, Torino, Italy, 2010, p. P.4.10.

[75] A. A. Juarez, S. Warm, C. A. Bunge, and K. Petermann, "Number of usable principal modes in a mode division multiplexing transmission for different multi-mode fibers," in *Proc. of Optical Fiber Conference (OFC)*, Los Angeles, CA, 2011, p. JTHA34.

[76] H. Bülow et al., "Measurement of the Maximum Speed of PMD Fluctuation in Installed Field Fiber," in *Proc. of Optical Fiber Conference (OFC)*, San Diego, CA., 1999, pp. WE4-1.

[77] S. Randel et al., "6×56-Gb/s mode-division multiplexed transmission over 33-km few-mode fiber enabled by 6×6 MIMO equalization," *Optics Express*, vol. 19, no. 17, pp. 16697-16707, August 2011.

[78] A. A. Juarez, D. Kroushkov, C. A. Bunge, and K. Petermann, "Comparison of MIMO receiver complexity in a MDM transmission system using Principal modes and L-P Modes," *ITG-Fachbericht 241, Photonische Netze*, pp. 57-60, 2013.

[79] Dimitris G. Manolakis, Vinay K. Ingle, and Stephen M. Kogan, *Statistical and adaptive signal processing*. Boston, London: Artech house, 2005.

[80] Yiteng Huang, Jacob Benesty, and Jingdong Chen, *Acoustic MIMO Signal Processing*. New York, USA: Springer, 2006.

[81] R. Schmogrow et al., "Error Vector Magnitude as a Performance Measure for Advanced Modulation Formats," *Photonic Technology letters*, vol. 24, no. 1, pp. 61-63, January 2012.

[82] R. Shafik, S. Rahman, and R. Islam, "On the Extended Relationships Among EVM, BER and SNR as Performance Metrics," in *4th International Conference on Electrical and Computer Engineering ICECE*, Bangladesh, 2006.

[83] A. Goldsmith, *Wireless communication*. New York: Cambridge University Press, 2005.

[84] U. Tietze and Ch. Schenk, *Halbleiterschaltungstechnik*. Heidelberg: Springer, 2002.

[85] C. D. Poole and R. E. Wagner, "Phenomenological approach to polarization dispersion in long single - mode fibers," *Electronic Letters*, vol. 22, no. 19, pp. 1029-1030, September 1986.